ADVANCEMENTS IN IRREVERSIBLE ELECTROPORATION FOR THE TREATMENT OF CANCER

Christopher Brian Arena

Dissertation submitted to the faculties of the
Virginia Polytechnic Institute and State University
and
Wake Forest University
in partial fulfillment of the requirements for the degree of

Doctor of Philosophy
in
Biomedical Engineering

Rafael V. Davalos
Marissa Nichole Rylander
John H. Rossmeisl, Jr.
John L. Robertson
Paulo A. Garcia

March 20th, 2013
Blacksburg, VA

Keywords: Pulsed Electric Field, Bipolar Pulses, High-Frequency, Phase Change Material, Latent Heat Storage, Tissue Engineering, Hydrogel, Electrochemotherapy, Electrogenetherapy

Advancements in Irreversible Electroporation for the Treatment of Cancer

Christopher Brian Arena

ABSTRACT

Irreversible electroporation has recently emerged as an effective focal ablation technique. When performed clinically, the procedure involves placing electrodes into, or around, a target tissue and applying a series of short, but intense, pulsed electric fields. Oftentimes, patient specific treatment plans are employed to guide procedures by merging medical imaging with algorithms for determining the electric field distribution in the tissue. The electric field dictates treatment outcomes by increasing a cell's transmembrane potential to levels where it becomes energetically favorable for the membrane to shift to a state of enhanced permeability. If the membrane remains permeabilized long enough to disrupt homeostasis, cells eventually die. By utilizing this phenomenon, irreversible electroporation has had success in killing cancer cells and treating localized tumors. Additionally, if the pulse parameters are chosen to limit Joule heating, irreversible electroporation can be performed safely on surgically inoperable tumors located next to major blood vessels and nerves.

As with all technologies, there is room for improvement. One drawback associated with therapeutic irreversible electroporation is that patients must be temporarily paralyzed and maintained under general anesthesia to prevent intense muscle contractions occurring in response to pulsing. The muscle contractions may be painful and can dislodge the electrodes. To overcome this limitation, we have developed a system capable of achieving non-thermal

irreversible electroporation without causing muscle contractions. This progress is the main focus of this dissertation. We describe the theoretical basis for how this new system utilizes alterations in pulse polarity and duration to induce electroporation with little associated excitation of muscle and nerves. Additionally, the system is shown to have the theoretical potential to improve lesion predictability, especially in regions containing multiple tissue types. We perform experiments on three-dimensional *in vitro* tumor constructs and *in vivo* on healthy rat brain tissue and implanted tumors in mice. The tumor constructs offer a new way to rapidly characterize the cellular response and optimize pulse parameters, and the tests conducted on live tissue confirm the ability of this new ablation system to be used without general anesthesia and a neuromuscular blockade.

Situations can arise in which it is challenging to design an electroporation protocol that simultaneously covers the targeted tissue with a sufficient electric field and avoids unwanted thermal effects. For instance, thermal damage can occur unintentionally if the applied voltage or number of pulses are raised to ablate a large volume in a single treatment. Additionally, the new system for inducing ablation without muscle contractions actually requires an elevated electric field. To ensure that these procedures can continue to be performed safely next to major blood vessels and nerves, we have developed new electrode devices that absorb heat out of the tissue during treatment. These devices incorporate phase change materials that, in the past, have been reserved for industrial applications. We describe an experimentally validated numerical model of tissue electroporation with phase change electrodes that illustrates their ability to reduce the probability for thermal damage. Additionally, a parametric study is conducted on various electrode properties to narrow in on the ideal design.

Acknowledgements

I would like to thank my advisor, Dr. Davalos, for his guidance throughout graduate school. Your patience and good humor along the way has made this experience truly enjoyable. Additionally, your willingness to expose your students to all aspects of translational research has provided me with the necessary skills to stand on my own. I am grateful to have had the opportunity to work on many exciting projects under your direction, and I could not have accomplished all that I have without your support and leadership. Thank you for always encouraging me to finish what I set out to do. You are a great mentor and friend.

I would also like to thank each of my committee members for helping me achieve this milestone in life. Dr. Rylander, your kindness and enthusiasm for research were part of the reason I chose to attend Virginia Tech. I appreciate that you helped me get established in the lab early on by securing funding and allowing me to learn techniques that you passed down to your students. I am also grateful that you have maintained an interest in my research until the end, and that you are always willing to help push my career forward. Dr. Rossmeisl, your efforts on helping us develop and test our new electroporation system were extraordinary. I would not be graduating with my doctorate had you not gone out on a limb with us that Saturday morning, and thereafter. It has been an honor to work with, and learn from you. Dr. Robertson, I am so appreciative of the fact that you gave us the opportunity to take our system to the next level by treating animal patients. It has been a unique and rewarding experience to see a technology develop this far and to be at your side during the procedures. This is what every biomedical engineer hopes for, and I look forward to continuing this work with you. Dr. Garcia, it has been great getting to know you personally and professionally. Thank you for making me feel welcome in the lab from the start, playing soccer, and hanging out downtown on countless nights. I have

enjoyed watching you succeed as a graduate student and postdoc. You set an extremely high bar in the lab, but are always willing to make the time to help others reach similar goals. Thanks for always being the voice of reason and for listening every day to new ideas and concerns. You already are, and will continue to be, an excellent advisor.

To my fellow lab mates, it has been a pleasure working with all of you. Thank you for helping with everything from conducting experiments to ordering supplies for the lab, and for always doing so with a positive attitude. A special thanks to Dr. Michael B. Sano, for sharing his knowledge of electronics, and for spending hours at a time building systems in support of this dissertation. You have helped me become a better engineer and been instrumental in bringing these systems to life.

To my siblings, Brian, Kimberly, Aimee, and Charles, thank you for always being there for me and for making me the person I am today. You are all an inspiration. To my fiancée Sara, thank you for agreeing to marry me. I am so lucky to have had you in my life over the past four years to face the challenges of graduate school together. You have always kept things in perspective and given me a reason to smile. You are the most caring person I have ever met, and I look forward to sharing the rest of our lives together

Finally, I would like to dedicate this dissertation to my parents, George and Debbie Arena. I am so blessed to have you as parents. You have always been there for me, and your belief in me has served as a never ending source of motivation. Thank you for everything you do, and I love you both.

Table of Contents

List of Figures

List of Tables

List of Abbreviations

IRE – Irreversible electroporation

H-FIRE – High-frequency irreversible electroporation

PEF – Pulsed electric field

TMP – Transmembrane potential

nsPEF – Nanosecond pulsed electric field

EGT – Electrogenetherapy

ECT – Electrochemotherapy

FEM – Finite element model

3D – Three-dimensional

PDE – Partial differential equation

ODE – Ordinary differential equation

H&E – hematoxylin and eosin

1 – Overview

1.1 – A Brief History of Cancer

Reports of what has come to be known as cancer (Latin word for crab) date back far beyond Hippocrates' coining of the term in 460 BC, where he noted that the blood vessels supplying a tumor resemble the far reaching legs of a crab. The first known documented case of cancer was found on the Edwin Smith Egyptian papyrus around 3000 BC, *wherein* eight cases of tumors in the breast were described ("The history of cancer," 2012). While physicians of the day noted that there is no treatment for this disease, palliative care was attempted using cauterization with a tool called the fire drill. By rapidly turning this ancient medical device, heat was generated along its shaft capable of focally burning the cancerous tissue (Wicker, 1990).

Over 5000 years later, there is still no all-encompassing cure for cancer. However, treatments have advanced to the point where complete remissions can be obtained for a variety of cancer types on a case-by-case basis. Some of these treatments, like the fire drill, rely on the generation of extreme temperatures to destroy tissue within a targeted region. Common examples of modern surgical tools include devices for performing radiofrequency ablation, cryoablation, laser ablation, and high-intensity focused ultrasound. Success of these modalities is, in large part, due to associated advancements in energy-based treatment planning systems as well as the concurrent development of medical imaging platforms that allow for improved tumor and treatment outcome visualization within the body.

Over the past decade, a non-thermal technique for tissue ablation, termed irreversible electroporation (IRE), has been developed by Davalos *et al*. (R. V. Davalos et al., 2005). The mechanism of action of IRE relies on the delivery of pulsed electric fields (PEFs) to create structural defects in a cell's plasma membrane, ultimately leading to its death. While there is a

certain degree of temperature increase due to Joule heating, pulsing protocols are designed to limit this increase to levels below those associated with thermal damage. The inherent non-thermal nature of IRE offers unique benefits (discussed in the following chapter) that have translated to the successful treatment of a variety of cancerous pathologies (Bagla et al., 2012; Ellis et al., 2011; Neal et al., 2011; Thomson et al., 2011).

1.2 – Project Goals

Despite the recent success of IRE for cancer treatment, several challenges remain that must be overcome in order to facilitate widespread clinical use of the technology. This is the focus of the research presented *herein*. Specifically, we aim to propose solutions for the following limitations:

1) The presence of multiple tissue types can distort the electric field distribution in the tissue and complicate treatment planning algorithms.
2) The PEFs used to perform IRE cause intense muscle contractions, which requires the administration of general anesthesia and neuroparalytic agents prior to treatment.
3) Cell death is highly dependent upon an electric field threshold, which can vary greatly between cell types.
4) There is an elevated probability for thermal damage in regions surrounding electrodes during high-dose cases of IRE.

1.3 – Document Organization

The document is organized into twelve chapters. Chapter 2 presents a literature review on the state of the art in electroporation-based therapies. Following Chapter 2, a theoretical groundwork is laid to help understand the complex interaction of PEFs with biological materials.

A model is presented that allows for the investigation of a cell's transmembrane potential (TMP) and pore density in response to high-frequency, bipolar PEFs. These types of waveforms are the primary focus of this work, as they represent a potential solution to both points 1) and 2) above. Up until this point, IRE has been performed with individual, unipolar PEFs that have durations on the order of 100 μs. By alternating pulse polarity on a timescale that is two orders of magnitude shorter, these waveforms have the ability to make heterogeneous tissues "look" electrically homogenous while at the same time reducing or eliminating muscle contractions depending on the location of treatment. In Chapter 4, the techniques presented in Chapter 3 are utilized at the tissue level to allow for a theoretical investigation of high-frequency, bipolar PEFs in heterogeneous tissues (Arena, Sano, Rylander, et al., 2011). The ability of these waveforms to non-thermally ablate tissue without causing muscle contractions is studied experimentally in Chapter 5. We termed this technique high-frequency IRE (H-FIRE) (Arena & Davalos, 2012; Arena, Sano, Rossmeisl, et al., 2011). Promising results led to the testing of H-FIRE on tumors implanted subcutaneously in mice (Chapter 6). Chapter 7 deals with the development of a computational model used to better understand the relationship between H-FIRE pulse parameters and muscle and nerve stimulation versus ablation area. Chapter 8 addresses point 3) above through the development of a three-dimensional (3D) tissue engineered tumor that allows for a rapid and economical evaluation of a cells electric field threshold for death without requiring the use of animal models (Arena, Szot, et al., 2012). Point 4) above is addressed by theoretically (Chapter 9) and experimentally (Chapter 10) exploring the use of latent heat storage materials in electrode designs to reduce the probability for thermal damage (Arena, Mahajan, et al., 2012). Finally, Chapter 11 highlights the major findings and future directions of this research, and Chapter 12 lists the references used throughout the document.

2 – Background of Electroporation

2.1 – Introduction

Electroporation, or electropermeabilization, is a phenomenon in which the application of PEFs across cells leads to the development of structural defects within lipid bilayer membranes. The PEFs have durations on the order of nanoseconds to microseconds and amplitudes on the order of hundreds to thousands of volts per centimeter. Defect creation results in increased membrane permeability to ions and macromolecules and is directly linked to the induced buildup of charge across membranes, or TMP, that is caused by the PEFs. It is hypothesized that defects take the form of nanoscale pores. A majority of the literature supports this claim on the basis of well-developed theory (Abidor et al., 1979; Weaver, 1994). However, the biophysical mechanisms behind membrane permeabilization are still highly debated, and real-time, direct visualization of pores remains to be seen. This lack of understanding has driven many chemists, biologist, physicists, and engineers to study electroporation. Today abundant literature exists on topics ranging from numerical techniques for modeling pore formation, such as molecular dynamics simulations of lipid bilayers (Leontiadou et al., 2004; Tieleman et al., 2003; Vernier et al., 2009), to clinical trials on therapies utilizing the electroporative phenomenon for the treatment of different diseases, such as cancer (Ball et al., 2010; Daud et al., 2008; Garon et al., 2007; Mir, Belehradek, et al., 1991; Thomson et al., 2011).

Although the interaction of electromagnetic fields with biological materials has been studied for over two centuries, it is unclear from literature when scientists first recognized the phenomenon of electroporation. One of the most intriguing reports is on tissue injury due to lightning strikes, where gross lesions in the brain have been found in some cases (Jex-Blake, 1913). While not reported at the time, it is now understood that injury mechanisms in electrical

shock trauma include not only thermal damage produced by Joule heating, but also in superposition tissue electroporation and macromolecule degeneration (R. C. Lee et al., 2000). Further, by tuning the electrical pulse parameters, electroporation can induce cell death without any significant levels of accompanying thermal damage (R. V. Davalos et al., 2005; R. V. Davalos et al., 2008; R. V. Davalos et al., 2003), giving rise to many of the benefits seen clinically, which are discussed later in this chapter. In this sense, membrane permeabilization is permanent and has given rise to the term IRE. Reversible electroporation results when membrane permeabilization is temporary and cells remain viable following pulsing. It is evident that observations of membrane breakdown occurred well before those of reversible electroporation (Stampfli et al., 1957).

In biotechnology and medicine, reversible electroporation has been used to introduce substances into cells that would normally not overcome the ionic transport barrier posed by the plasma membrane. These substances include foreign DNA and drugs, among other hydrophilic and large macromolecules (Prausnitz et al., 1993; Titomirov et al., 1991). In the case of gene uptake into cells, 3 pulses separated by 3 s generating an electric field with an amplitude of 8000 V/cm and a duration of 5 μs were initially found to result in efficient transfection (Neumann et al., 1982). Another important discovery at the time was that dielectrophoresis can be combined with reversible electroporation to promote cell fusion (electrofusion), which is an important application in synthetic biology and tissue engineering (Pilwat et al., 1981). In the late 1980's, researchers proposed that the cytotoxicity of chemotherapeutic drugs could be enhanced through the application of high voltage electrical impulses (Okino et al., 1987; Orlowski et al., 1988). Bleomycin, which acts by cleaving DNA, has become the primary drug of choice. It is not membrane permeable through passive diffusion unless combined with electroporation, affording

the treatment a high level of selectivity. It is important to note that the pulse parameters first proposed for electrofusion are distinct from those used in what is now called electrochemotherapy (ECT) (Mir, Orlowski, et al., 1991) and electrogenetherapy (EGT), and the role of various pulsing protocols for different electroporation applications will be discussed throughout this chapter.

Electroporation-based therapies involve delivering pulses through electrodes inserted directly into, or adjacent to, the targeted tissue. During ECT and EGT, there is an accompanying occurrence of IRE for cells located near electrodes due to the high electric field gradient and narrow range of pulse parameters that are effective at inducing reversible electroporation (Onik et al., 2007). As a result, IRE was first viewed as an upper limit in reversible electroporation applications. It was not until the last decade that IRE was explored as a therapeutic means to destroy substantial volumes of targeted tissue without the use of adjuvant drugs (R. V. Davalos et al., 2005). The first *in vivo* experiments demonstrated that a necrotic lesion occurs with cell scale resolution (J. F. Edd et al., 2006), which can be imaged using ultrasound (Onik et al., 2007) or MRI (Ellis et al., 2011). Further, by designing protocols that minimize any associated Joule heating, IRE promotes preservation of sensitive structures, such as major nerves (Onik et al., 2007), blood vessel architecture, and extracellular matrix components (Maor et al., 2007). Another independent, non-thermal technique for tissue ablation utilizes electric fields with strengths that are an order of magnitude greater (~100 kV/cm) and durations an order of magnitude shorter (~100 ns) than those typically used for ECT, EGT, and IRE. These nanosecond pulsed electric fields (nsPEF) are known to cause electroporation within the membranes of intracellular organelles (Vernier et al., 2006) as well as the plasma membrane

(Pakhomov et al., 2007). *In vivo* results indicate that the mechanism of cell death for nsPEFs is distinct from IRE, and involves predominantly apoptotic pathways (Long et al., 2011).

2.2 – Published Results on IRE

After being shown theoretically to be a feasible non-thermal focal ablation technique in 2005 by Davalos, *et al*. (R. V. Davalos et al., 2005), the first *in vivo* study with this objective in mind was carried out by Edd, *et al*. (J. F. Edd et al., 2006). This study placed two plate electrodes on opposite sides of a rat liver and delivered a 20 ms long square wave pulse with a voltage-to-distance ratio of 1000 V/cm. Animals were sacrificed 3 hours after pulsing, and the tissue was perfusion fixed. Numerical simulations calibrated the lesion IRE thresholds to range between 300 and 500 V/cm, and histological examination showed cellular-scale resolution between treated and unaffected cells, with nearly indistinguishable cell borders in the treated areas. The large vessel architecture remained intact. It also showed endothelial necrosis and congestion in the treated region, such that any surviving cells in the treatment region were subject to ischemia.

The vascular effects of the pulses were further explored by Maor, *et al*. (Maor et al., 2007, 2008; Maor et al., 2009). These studies investigated the ability to use IRE for tumor ablation in close proximity to vasculature, a limitation of thermal focal ablation techniques. They used plate electrodes to apply 10, 100 μs long pulses of 3800 V/cm in one second to exposed rat carotid arteries. Rats were sacrificed and the tissue fixed at several time points up to 28 days after the procedure. Overall the treated vessels showed preserved endothelial cells of the internal lamina, with a progressive decrease in vascular smooth muscle cells in the tunica media.

Investigation of the immune system's interaction with IRE was carried out for healthy tissue and tumors (Bassim Al-Sakere et al., 2007; E. W. Lee et al., 2007; Onik et al., 2007; Rubinsky et al., 2007). In these studies, cutaneous implanted murine tumors and healthy tissue

were exposed and pulsed using plate electrodes. For the tumor study, tissue samples were collected for immunohistochemistry and it was found that T-lymphocyte levels were highest prior to treatment, and rapidly declined within the first 6 hours after pulsing. The authors conclude that the mechanism of necrosis occurs independent of the immune system and may therefore be a suitable treatment option for immunocompromised patients. In addition, immune responses over longer time points were investigated in large animal models. In (Rubinsky et al., 2007), porcine livers were subjected to IRE pulses. By 24 hours, there was an increase in inflammatory cells and signs of drainage by the regional lymph nodes. These findings were consistent with observations from lesions produced in canine prostates (Onik et al., 2007). In (E. W. Lee et al., 2007), porcine liver tissue 24 hours after treatment showed that the ablated regions contained calcium deposition, were positive for the BCL-2 apoptosis marker, and showed sinusoids congested with neutrophils and eosinophils.

Studies experimentally investigating the ability for IRE to effectively treat tumors have been carried using implanted tumors in a murine (B. Al-Sakere et al., 2007; Guo et al., 2010; Neal et al., 2010). In the first study by Al-Sakere *et al.* (B. Al-Sakere et al., 2007), a murine sarcoma cell line was used to grow cutaneous tumors in mice. TUNEL staining showed increased DNA double strand breaks suggesting apoptosis. Additionally, observed vascular occlusion may indicate additional hypoxia-induced tumor cell death. Tumors subjected to a protocol of 80 pulses of 2500 V/cm, each 100 μs long and separated by 3.3 seconds, showed complete regression in 12 of 13 trials. In a second study performed by Neal *et al.* (Neal et al., 2010), MDA-MB-231 human mammary carcinoma cells were grown into tumors orthotopically within the mammary fat pad of mice. A total of 100 pulses ranging between 1100 and 1300 V were delivered through a single, bipolar electrode, each lasting 100 μs and separated by 3

seconds. The bipolar probe design included a 2.30 mm long insulative sheath to separate the active portions of the electrode. Complete regression was achieved in 5 of 7 experimental tumors. In a third study by Guo *et al*. (Guo et al., 2010), the N1-S1 rat hepatoma cell line was used to induce tumors in the left medial lobe of the liver in Sprague-Dawley rats. They were treated using eight 2500 V/cm square wave pulses, each 100 µs long at a rate of 1 pulse every 100 ms. They found significant tumor volume reductions within 7-15 days post-therapy using MRI and histology.

There have been several pre-clinical trials on animal patients, two of which may be found in (Garcia, Pancotto, et al., 2011; Neal et al., 2011). One patient had a non-resectable forebrain malignant glioma (Garcia, Pancotto, et al., 2011). This 12-year old canine presented with rapidly progressive neurological deterioration due to the growth of his tumor. IRE was performed at the time of biopsy for the patient based on treatment parameters derived from numerical models and preliminary data on IRE in normal brain (Ellis et al., 2011; Garcia et al., 2010). The IRE ablation procedure resulted in nearly complete resolution of focal neurological dysfunction within one week of the procedure. An MRI scan of the brain performed 48 hours after the IRE demonstrated a 75% reduction in tumor mass. The canine patient subsequently received adjunctive fractionated whole-brain radiotherapy for 4 weeks following IRE (50 Gy, delivered in 20 fractions of 2.5 Gy each). The patient was in complete remission 4 months after IRE therapy, based on serial MRI and neurologic examinations.

An additional canine patient (6-year old, spayed female Labrador Retriever) has been reported on in (Neal et al., 2011). The patient presented with a large soft tissue sarcoma (high grade histiocytic sarcoma) on the inner aspect of the thigh and groin. The tumor was causing sciatic neuropathy, and compartmental syndrome-associated pain. Its proximity to vital nerves

and vasculature made it unresectable, and thermal therapies would have also damaged these vital structures. IRE was performed with 3 electrode insertions, and a 54% reduction in tumor volume was observed within 8 days, as well as improved mobility and no further need for pain medicine. The great response resulted in the use of systemic chemotherapy (four cycles of CCNU, 65 mg/m^2 every 21 days), until the tumor developed resistance to the chemotherapy. A second application of IRE to an originally untargeted region of the tumor was performed to eliminate the remainder of the tumor. Findings from this study include the ability for IRE to remain effective to cancer cells that have developed resistance to chemotherapy as well as muscle cell sparing at the tumor boundary as observed by serial biopsies taken at the margin. Electrophysiological evaluation revealed small decreases in the amplitudes of the distal compound muscle action potentials, which returned to pre-IRE values 2 weeks after treatment. By four months post-diagnosis, the cancer was considered in remission, and remains in complete remission based on follow-up examinations currently 24 months after the original diagnosis.

In addition to the promising pre-clinical case studies using IRE to treat more delicate and complex varieties of tumors, there are several early stage human trials that have been conducted. These include a phase 1 safety trial on various localized tumors with incurable malignancies (Ball et al., 2010; Thomson et al., 2011). The primary aim of the study was to determine the safety of IRE therapy at various organs in the body (liver, kidney, and lung) for patients' refractory to alternative therapies. Complete tumor ablation verified by CT was achieved in 46 of the 69 tumors, a success rate of 66%, with most failures occurring in renal and lung tumors (Thomson et al., 2011). For the lung, it was proven safe, but pneumothorax was almost inevitable. One interesting result was the nearly complete absence of post-ablation pain. Biopsies one month after surgery showed preservation of tissue structure with coagulative necrosis of the

cells. A separate report from this study discusses patient anesthesia considerations, including the need for general anesthesia, a neuromuscular blockade, careful patient positioning for CT-guided therapies, and the use of an ECG synchronizing system to prevent arrhythmias (Ball et al., 2010). Overall, this safety study showed the ability to use IRE safely in treating a variety of tumors located throughout the body. Recently, these results have been extended to include pancreatic cancer, following 100% ablation success in 27 patients 90 days post-IRE (Martin et al., 2012).

2.3 – Conclusion

Electroporation-based therapies rely on the ability of pulsed electric fields to create permeabilizing defects in cellular membranes. It is understood that the electric field promotes an increase in TMP up to a critical permeabilizing threshold. The stress created by the induced TMP leads to a time dependent transition in the membrane structure (Teissie et al., 2005). However, there is still debate over the nature of the stress itself, the mechanism by which the stress causes a reorganization of the membrane, and the molecular description of the reorganization. One widely accepted theory presented in Chapter 3 is based on the transition of hydrophobic pores inherent to lipid bilayers into hydrophilic pores capable of conducting ions. However, this theory fails to answer certain experimental observations, such as effects on the membrane-solution interfacial regions (Lopez et al., 1988) and membrane conductance fluctuations (Antonov et al., 1980). Additionally, in molecular dynamics simulations of lipid bilayers, recent results indicate that pore formation is controlled by the increased likelihood of water defects in the membrane, as opposed to lipid headgroup interactions (Tieleman, 2004). Continued advances in molecular dynamics, along with spectroscopic methods and imaging techniques will help to elucidate the biophysical mechanism behind the electroporative phenomenon (Teissie, 2002).

Despite lacking a complete understanding of electroporation at the cellular and molecular scale, therapies utilizing the electroporative phenomenon are having great success in clinical applications. This can be attributed to the proven therapeutic efficacy and safety of IRE, ECT, EGT, and nsPEFs. In the future, all electroporation-based therapies will find their place in medicine. In particular, it is likely that cancer, a disease for which no universal cure is in sight, will require combinatorial therapies to treat patients. Already, great clinical outcomes have been achieved by performing IRE, ECT, EGT, and nsPEFs alone, together, or in combination with other conventional therapies, such as radiation therapy. This multimodal approach will continue to be an avenue of future research as the field of electroporation develops and gains recognition.

3 – Modeling the Effects of High-Frequency Pulsed Electric Fields on Single Cells

3.1 – Introduction

Reversible electroporation is a precursor for the development of irreversible membrane defects. As a result, the theoretical background commonly used to describe ECT and EGT overlaps with that of IRE, and to some extent, nsPEFs. This chapter begins with a discussion of how governing equations for predicting the microscopic electric field distribution within single cells and macroscopic electric field distribution within tissues can be derived from Maxwell's equations. Analytical techniques are then presented for predicting TMP development and pore formation at the single cell level based on the local electric field distribution. This analysis includes a formulation allowing for the accurate prediction of these two outcomes when bipolar PEF are applied during H-FIRE.

3.2 – Theoretical Considerations of Electroporation

3.2.1 – Electromagnetics and the Electro-quasistatic Assumption

The interaction of electromagnetic waves with objects, such as cells, is governed by Maxwell's equations, which are given in differential form as:

$$\nabla \times H = J + \frac{\partial \boldsymbol{D}}{\partial t} \text{ (Maxwell-Ampere's law)} \quad (1)$$

$$\nabla \times E = -\frac{\partial \boldsymbol{B}}{\partial t} \text{ (Faraday's law of induction)} \quad (2)$$

$$\nabla \cdot D = \rho_e \text{ (Gauss's law)} \quad (3)$$

$$\nabla \cdot B = 0 \text{ (Gauss's law for magnetism)} \quad (4)$$

where H is the magnetic field, J is the current density, D is the electric displacement, E is the electric field, B is the magnetic flux density, and ρ_e is the electric charge. Solutions to the full-

wave Maxwell's equations are difficult to obtain but are required when the characteristic dimension of the object under consideration is on the same order of magnitude as the distance an electromagnetic wave covers during the characteristic time. With unipolar, rectangular pulses used in a majority of electroporation experiments, the characteristic time is often taken as the rise time of the pulse (Chen et al., 2009). When the object is electrically small compared to both the wavelength and skin depth in a given tissue, propagation effects are negligible and solutions are easier to come by. By ignoring the dynamics of electromagnetics, changes in current or charge distribution have an instantaneous effect in space. Practically, this can be applied to Maxwell's equations by implementing the electro-quasistatic approximation, which neglects magnetic induction, such that Equation 2 becomes:

$$\nabla \times E = 0 \tag{5}$$

This assumption is valid if the electric energy density exceeds the magnetic energy density (Steinmetz et al., 2006). Equation 5 allows for expression of the electric field only in terms of the electric potential (ϕ):

$$E = -\nabla\phi \tag{6}$$

Combining Equation 1 with the constitutive relations for dielectric materials:

$$D = \varepsilon E \tag{7}$$

$$J = \sigma E \tag{8}$$

where ε is the dielectric permittivity and σ is the conductivity, and Equation 6 yields:

$$\nabla \times H = -\sigma\nabla\phi - \varepsilon\frac{\partial\nabla\phi}{\partial t} \tag{9}$$

Because the magnetic field is not essential to the motion of charges under the electro-quasistatic approximation (Haus et al., 1989), it can be eliminated by taking the divergence of Equation 9,

which results in a conditional equation for the spatial and temporal distribution of electric potential:

$$0 = -\nabla \cdot (\sigma \nabla \phi) - \varepsilon \nabla \cdot \left(\frac{\partial \nabla \phi}{\partial t}\right) \qquad (10)$$

Equation 10 simplifies into a steady-state equation in the electrostatic case when the time derivative vanishes:

$$0 = -\nabla \cdot (\sigma \nabla \phi) \qquad (11)$$

This further simplification is valid when the duration of a rectangular pulse is much larger than the charging time constant of cellular membranes. The time constant is defined as the time required for the TMP to reach 63% of its steady state value, such that transient effects occurring during the pulse rise time are neglected (Natasa Pavselj et al., 2011). This is not always the case, especially when studying nsPEFs or H-FIRE (Arena, Sano, Rossmeisl, et al., 2011; Arena, Sano, Rylander, et al., 2011). Both Equations 10 and 11 can be solved by employing analytical techniques (separation of variables) or numerical techniques (finite element modeling), which form the basis of the remaining sections of this chapter, as well as Chapter 4.

3.2.2 – Analytical Techniques for Cell-scale Modeling of TMP and Pore Formation during Unipolar PEFs

Predictions of TMP are often made under the assumption that a cell is geometrically and electrically representative of a dielectric, spherical shell (plasma membrane) containing and surrounded by an electrolytic solution (cytoplasm and extracellular space, respectively). Under this treatment, Equation 11 is readily solved using separation of variables in spherical coordinates with the center of the cell aligned at the origin. The details of this derivation including definitions of boundary conditions are given by Kotnik and Pucihar (Tadej Kotnik et

al., 2010), and the general solution for electric potential with an arbitrary number of concentric shells is:

$$\phi(\varsigma, \theta) = \left(A_i \varsigma + \frac{B_i}{\varsigma^2}\right) cos\theta \qquad (12)$$

where ς is the distance from the origin, θ is the angle between the electric field and a chosen point on the cell membrane (Figure 3.1), and *A* and *B* are constants specific to different cellular regions (i). Due to axial symmetry, the 3D spherical problem reduces to a 2D circular problem. Without accounting for the presence of intracellular organelles or including permittivity terms in calculations, the steady state TMP in a uniform electric field (*E*) is (Tadej Kotnik et al., 2010):

$$\Delta\phi = (\phi_i - \phi_o) = f_s ER \cos\theta \qquad (13)$$

where ϕ_i and ϕ_o are the electric potentials at the inner and outer surface of the membrane respectively, *R* is the cell radius, and f_s is a function reflecting the plasma membrane thickness and conductivity of the extracellular space (*e*), plasma membrane (*pm*), and cytoplasm (*c*). This model is accurate for exposures that are much longer than the charging time of the plasma membrane, which is typically less than one microsecond (Figure 3.1). By adding a concentric shell inside the plasma membrane, the model is expanded to include the effect of an organelle, often regarded as the nucleus, on the electric field distribution. It is then possible to predict the TMP on intracellular membranes, such as the nuclear envelope (*ne*) that surrounds the nucleoplasm (*n*), when nsPEFs are applied across the cell. Further, when each cellular region is characterized by both a dielectric permittivity and conductivity, the model is accurate for alternating fields with frequencies in the MHz range or for pulsed fields with rise times in the nanosecond range (T. Kotnik et al., 2000). In this formulation, the constants *A* and *B* are determined by solving the boundary conditions of continuity of electric potential (Eq. 14, 15, 16,

17) and electric current density (Eq. 18, 19, 20, 21), in addition to the assumptions of a finite field at $r = 0$ and a uniform field at $r = \infty$. In order to accurately predict the TMP in a time-varying electric field, the admittivity operator ($\Lambda_i = \sigma_i + \varepsilon_i(\partial/\partial t)$) is used in the formulation for the boundary conditions (Yao et al., 2007):

$$\phi_n(R_n - d_{ne}, \theta) = \phi_{ne}(R_n - d_{ne}, \theta) \quad (14)$$

$$\phi_{ne}(R_n, \theta) = \phi_c(R_n, \theta) \quad (15)$$

$$\phi_c\big(R_c - d_{pm}, \theta\big) = \phi_{pm}\big(R_c - d_{pm}, \theta\big) \quad (16)$$

$$\phi_{pm}(R_c, \theta) = \phi_e(R_c, \theta) \quad (17)$$

$$\Lambda_n \frac{\partial \phi_n}{\partial \varsigma}\Big|_{R_n - d_{ne}} = \Lambda_{ne} \frac{\partial \phi_{ne}}{\partial \varsigma}\Big|_{R_n - d_{ne}} \quad (18)$$

$$\Lambda_{ne} \frac{\partial \phi_{ne}}{\partial \varsigma}\Big|_{R_n} = \Lambda_c \frac{\partial \phi_c}{\partial \varsigma}\Big|_{R_n} \quad (19)$$

$$\Lambda_c \frac{\partial \phi_c}{\partial \varsigma}\Big|_{R_c - d_{pm}} = \Lambda_{pm} \frac{\partial \phi_{pm}}{\partial \varsigma}\Big|_{R_c - d_{pm}} \quad (20)$$

$$\Lambda_{pm} \frac{\partial \phi_{pm}}{\partial \varsigma}\Big|_{R_c} = \Lambda_e \frac{\partial \phi_e}{\partial \varsigma}\Big|_{R_c} \quad (21)$$

where d represents membrane thickness. To avoid working with differential operators, the admittivity operator is transformed into the frequency domain ($\Lambda_i = \sigma_i + s\varepsilon_i$), where s is the complex frequency ($j\omega$) of the applied field. The resulting solutions for TMP ($\Delta\varphi$) across the plasma membrane and nuclear envelope can then be expressed as (Yao et al., 2007):

$$\Delta\phi_{pm}(s) = \phi_e(R_c, \theta) - \phi_c\big(R_c - d_{pm}, \theta\big) = H_{pm}(\mathrm{s})E(s)\cos\theta \quad (22)$$

$$\Delta\phi_{ne}(s) = \phi_c(R_n, \theta) - \phi_n(R_n - d_{ne}, \theta) = H_{ne}(\mathrm{s})E(s)\cos\theta \quad (23)$$

where $H_{pm}(s)$ and $H_{ne}(s)$ are transfer functions that reflect the geometric and dielectric properties of the various cellular regions, the exact formulations of which are given in detail in (T. Kotnik

et al., 2006). $E(s)$ was obtained by taking the Laplace transform ($\mathcal{L}$) of the time-varying electric field, which was composed of a series of step functions. Any time varying electric field can be constructed with a series of step functions, whose Laplace transforms are readily available. By exposing the system to each individual step, the complete time course for TMP is obtained upon taking the inverse Laplace transform of Equations 22 and 23 and performing a summation of the individual step responses. TMP development is sensitive to the geometric and dielectric properties of different cellular regions. Determination of accurate parameters is important not only for treatment planning in the field of electroporation, but in any application that relies on the complex interaction of cells with electric fields, such as cancer cell detection with dielectrophoresis (Gascoyne et al., 2002).

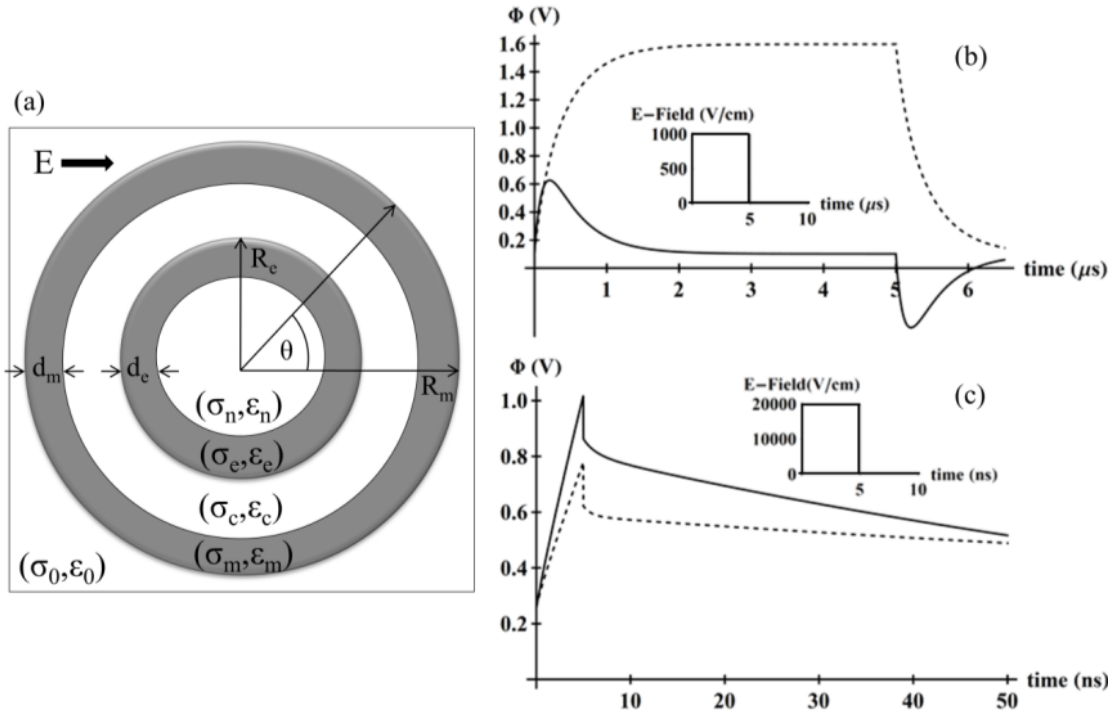

Figure 3.1. TMP development on a spherical cell subject to microsecond and nanosecond order pulsed electric fields. (a) Schematic diagram of the different cellular regions and their geometric and dielectric properties. (b) Response of the plasma membrane (dashed line) and nuclear envelope (solid line) to a 1000 V/cm, 5 μs pulse at $\theta = 0$. (c) Response of the plasma membrane (dashed line) and nuclear envelope (solid line) to a 20,000 V/cm, 5 ns pulse at $\theta = 0$. Adapted from (T. Kotnik et al., 2006).

To illustrate the concept of TMP development, parameters typically used in the literature for electroporation of cells in physiologic saline are implemented in this example (T. Kotnik et al., 2006). Figure 3.1 shows a comparison between a microsecond order pulse used to target the plasma membrane in IRE, ECT, and EGT treatments versus a nanosecond order pulse that acts predominantly on organelles in nsPEF treatments. At the onset of the microsecond pulse, the TMP of the plasma membrane rises at a slower rate than the nuclear envelope. The results are taken at the cell pole ($\theta = 0$), which depicts a maximum. Once the plasma membrane becomes sufficiently charged, it begins to effectively shield the inside of the cell from the electric field. As a result, the TMP on the nuclear envelope begins to decrease. The process continues until steady state is reached and the nuclear envelope TMP returns to a baseline. The baseline here was set to 100 mV on both membranes to simulate a resting potential seen physiologically (Pavlin, Pavselj, et al., 2002). The premise behind nsPEF treatment protocols is that the system is exposed to an impulse that occurs on a faster timescale than the plasma membrane charging time constant. Depending of the dielectric properties, the charging time of an organelle is typically faster than the plasma membrane due to its smaller size. As a result, when the amplitude of a nanosecond pulse is increased 10 fold above the microsecond pulse, the nuclear envelope TMP increases before any shielding effect sets in due to plasma membrane charging. This would also be the case for other intracellular organelles, such as the mitochondria and endoplasmic reticulum. It is then theoretically possible for organelles to undergo electroporation without first electroporating the plasma membrane. Initial experimental results on cells *in vitro* supported this claim based on the fact that intracellular membranes were disrupted while the plasma membrane remained intact (Schoenbach et al., 2001). However, recent studies suggest that plasma membrane electroporation occurs simultaneously with organelle electroporation (Vernier et al., 2006).

These controversial results are influenced by the fact that membrane charging times are sensitive to the geometric and dielectric properties of the surrounding regions. To emphasize the desired effect of nsPEFs in this demonstration, the nucleoplasm conductivity was increased from 0.3 to 0.7 S/m, which remains physically realistic (T. Kotnik et al., 2006).

The TMP on the plasma membrane in the previous example reaches a steady state of around 1.6 V at the cell pole. Experimentally, the maximum TMP measured is ~1 V for most cell types (Tsong, 1983). This discrepancy is due to the formation of pores in the plasma membrane. Above a critical TMP, in this case ~1 V, the formation of pores greatly increases the effective plasma membrane conductivity. Therefore, electromagnetic theory for predicting TMP must be supplemented with equations for predicting the role of pore formation on membrane conductivity. The theory of pore formation describes the presence of both hydrophobic and hydrophilic pores in the plasma membrane (Figure 3.2). Hydrophobic pores are naturally occurring nonconductive gaps in the lipid bilayer due to thermal fluctuations. They are the precursor for hydrophilic pores, which conduct electricity. The transition of a hydrophobic pore to a hydrophilic pore depends on the energy function for each type of pore (Abidor et al., 1979):

$$U(r) = U_p \left(\frac{r}{r_p}\right)^2 \text{ (hydrophobic)} \qquad (24)$$

$$U(r) = 2\pi\gamma r - \pi\delta r^2 + \left(\frac{D}{r}\right)^4 \text{ (hydrophilic)} \quad (25)$$

where r is the pore radius, γ is the edge energy of a pore, δ is the membrane surface tension, D is a constant, and r_p and U_p are the minimum radius and energy for a hydrophilic pore, respectively (Glaser et al., 1988). The values for the different parameters can be found in (Neu et al., 1999), and each term is given in units of Boltzmann constant multiplied by temperature, kT, where 1 kT = 4.11×10^{-21} J. Both curves are shown in Figure 3.2. In attempt to minimize energy, a pore with a

given radius assumes the lesser of the two curves. The peak at point (r_p, U_p) represents the energy barrier for the creation of hydrophilic pores, while the maximum at point (r_e, U_e) is the energy barrier for the spontaneous expansion of hydrophilic pores. When a hydrophobic pore is created with a radius greater than r_p it naturally transitions into a hydrophilic pore. Thermal fluctuations cause the hydrophilic pore radius to settle at a minimum energy radius of r_m, and spontaneous expansion of pores is unlikely when TMP equals zero. An increase in TMP due to the application of an external electric field reduces the pore energy in Equations 24 and 25 by the capacitive contribution of the membrane to pore energy, $\pi a_p \Delta\phi_m^2 r^2$ (Neu et al., 1999), where a_p is a constant based on the dielectric properties of the membrane and surrounding medium. In Figure 3.2, as TMP is increased, the likelihood of spontaneous pore expansion increases due to the reduction and eventual elimination of the maximum at point (r_e, U_e).

Following a description of pore energy, the pore formation process can be described by a Smoluchowski advection-diffusion partial differential equation (PDE) (Pastushenko et al., 1979). Through an asymptotic reduction of the PDE, Neu and Krassowska derived an ordinary differential equation (ODE) for pore density (DeBruin et al., 1999):

$$\frac{dN}{dt} = \alpha e^{(\Delta\phi_m/\phi_{ep})^2}\left(1 - \frac{N}{N_0} e^{-q(\Delta\phi_m/\phi_{ep})^2}\right) \quad (26)$$

where N_0 is the equilibrium pore density, α is the creation rate coefficient, ϕ_{ep} is the characteristic voltage of electroporation, and q is the pore creation rate. Values for these constants are derived from expressions for pore energy and the original PDE (DeBruin et al., 1999; Neu et al., 1999). Pore density can be related to the membrane conductivity through (Pucihar, Miklavcic, et al., 2009):

$$\sigma_m = \sigma_{m0} + N(t)\sigma_p \pi {r_m}^2 A \quad (27)$$

where σ_{m0} is the non-electroporated membrane conductivity and σ_p is the conductivity inside a pore. The variable A is a lengthy formulation that includes the non-dimensional TMP and can be found in (Pucihar, Miklavcic, et al., 2009).

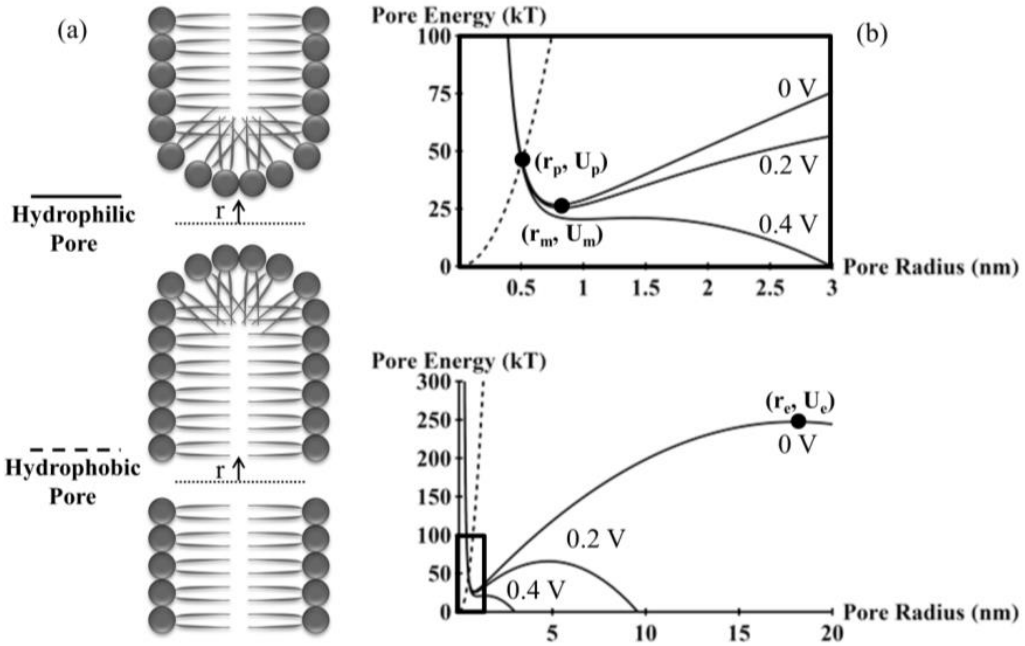

Figure 3.2. Theoretical illustration of pore formation in a planar bilayer membrane. (a) Schematic diagram of hydrophobic and hydrophilic pores with radius, *r*. (c) Energy of hydrophobic (dashed line) and hydrophilic (solid line) pores as a function of radius and the influence of increasing TMP on each. The cutout (b) represents a zoomed in view of pore energy around the energy barrier for the creation of hydrophilic pores (r_p, U_p). The point (r_e, U_e) is the energy required for the spontaneous expansion of hydrophilic pores and (r_m, U_m) is the minimum stable energy of a hydrophilic pore. Adapted from (Neu et al., 1999)

The step response method described previously for calculating the TMP induced by an arbitrary electric field can be modified to include Equation 27. To reiterate, the electric field time course is approximated by a series of step functions. The response of the system to the first time step is used to calculate pore density and dynamically alter the membrane conductivity. The next time step then proceeds with the updated value of membrane conductivity acting as an initial condition. A similar procedure is described by Talele and Gaynor (Talele et al., 2007).

Figure 3.3 shows a comparison between the TMP traced around one half of a cell (-90° to 90°) at different time points for the passive model of TMP and the active model of TMP that includes varying membrane conductivity. Without accounting for pore formation, the TMP at the cell pole increases with time until steady state is reached. If pore formation is included, once the TMP exceeds a critical threshold for electroporation (~1 V) the membrane conductivity increases. This results in a decreased TMP around the cell pole. In this example, membrane resting potential was neglected, such that the results are symmetric around the other half of the cell. Experimentally, similar spatial distributions are obtained using a voltage sensitive fluorescent dye that interacts with the cell membrane (Hibino et al., 1991; Pucihar, Kotnik, et al., 2009) for the time courses investigated. However, at later times, an additional mechanism is seen experimentally that is not included in the current model. Membrane conductivity continues to increase even though the model approaches steady state. It is hypothesized that pore radius can increase over time and small pores can merge into larger pores. This phenomenon has been the focus of theoretical electroporation research in the past decade (Neu et al., 2003; Smith et al., 2004), and molecular dynamics simulations of pore formation are advancing to bridge the gap between computational and experimental results (Tarek, 2005).

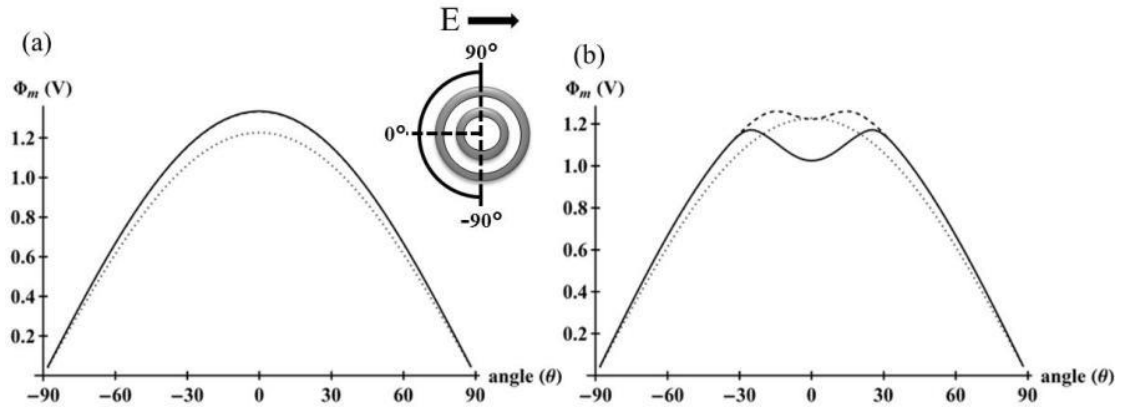

Figure 3.3. Influence of pore formation on the spatial variation of TMP around one-half of a spherical cell. (a) TMP versus angle without pore formation. (b) TMP versus angle with pore formation. The different curves on each graph represent time points of 1 μs (dotted line), 2 μs (dashed line), and 4 μs (solid line) throughout a 900 V/cm, 4 μs pulse.

3.3 – Fluctuations in TMP and Pore Formation during Bipolar PEFs

The techniques presented in the previous section can be utilized to study how high-frequency bipolar waveforms affect the plasma membrane in terms of the induced TMP and extent of pore formation. Here, an 8 μs unipolar pulse is compared to bipolar bursts with frequencies ranging from 125 kHz to 500 kHz. The frequency is defined as the inverse of twice the duration of single polarity (e.g., a 500 kHz signal's duration of single polarity is 1 μs). The top rows of Figures 3.4 and 3.5 illustrate the waveforms under investigation. Cell specific parameters required to solve Equations 22, 23, 26, and 27 are the same as those found in (Talele et al., 2010), and the model was validated based on qualitative comparisons to their results using a constant PEF stimulus. The step size was set at 125 ns as further reductions in step size did not significantly affect the results. Mean simulation time for the response to an individual input signal was 13.8 min.

The results for a PEF amplitude of 600 V/cm are shown in Figure 3.4. For a unipolar pulse (Figure 3.4 a, e, and i), the TMP reaches a peak around 2 μs. This corresponds to the point of inflection in the pore density curve. After 3 μs, the pore density reaches a plateau causing the TMP level off around 1 V. These kinetics result from the fact that pore formation increases membrane conductivity, which restricts any further increase in TMP above 1V. If pore formation is omitted, the TMP unrealistically approaches 1.5 V (data not shown). When a bipolar pulse with a duration of single polarity greater than 3 μs is used (Fig 3.4 b, f, and j), the model predicts that there is no difference in TMP or pore density kinetics. For a duration of single polarity of 2 μs (Fig 3.4 c, g, and k), there is a slight reduction in pore density and increase in peak TMP. However, electroporation is still thought to occur if the pore density is greater than $3\times10^{13}m^{-2}$, which was calculated as being an appropriate level of reversible electroporation (Hibino et al.,

1991). Based on this criterion, no electroporation occurs for bipolar pulses with durations of single polarity of 1µs (Fig 3.4 d, h, and l) when the applied amplitude is 600 V/cm. This introduces the trade-off between increased frequency and the extent of electroporation, which is discussed more in the next chapter. Additionally, the action of repetitive pulses in a burst sequence has a minimal influence on the pore density following the initial spike due to the first pulse (Fig 3.4 l).

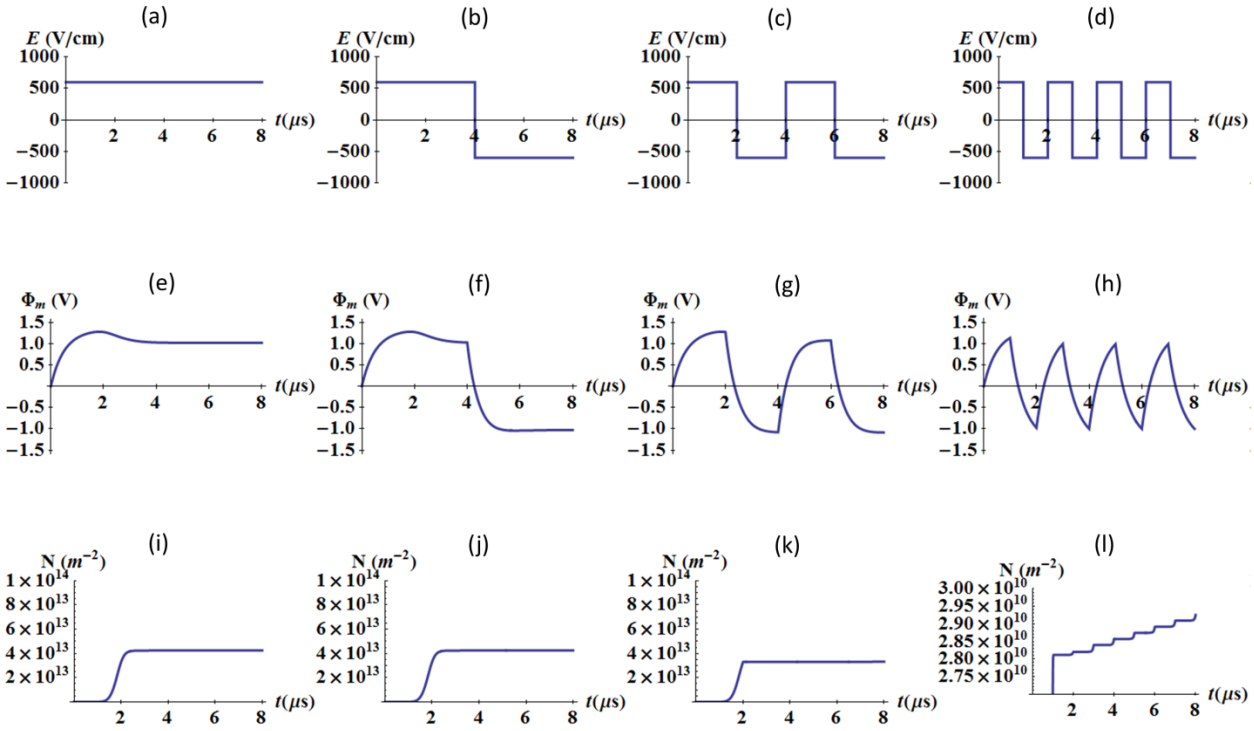

Figure 3.4. TMP and pore density during various bipolar PEFs. (a-d) Input signals with an amplitude of 600 V/cm. (e-h) Resulting TMP development as a function of time. (i-l) Resulting pore density as a function of time.

The results for a PEF amplitude of 900 V/cm are shown in Figure 3.5. For a unipolar pulse (Figure 3.5 a, e, and i), the peak in TMP occurs earlier, around 1 µs, when compared to a PEF amplitude of 600 V/cm. Additionally, pore density plateaus earlier, and the TMP levels off at a lower voltage, around 0.2 V. In this case, if pore formation is omitted, the TMP unrealistically approaches 2 V (data not shown). Because the pore formation kinetics occur much

faster, bipolar pulses with a duration of single polarity as short as 1 µs produce pore densities comparable to the unipolar pulse (Figure 3.5 l).

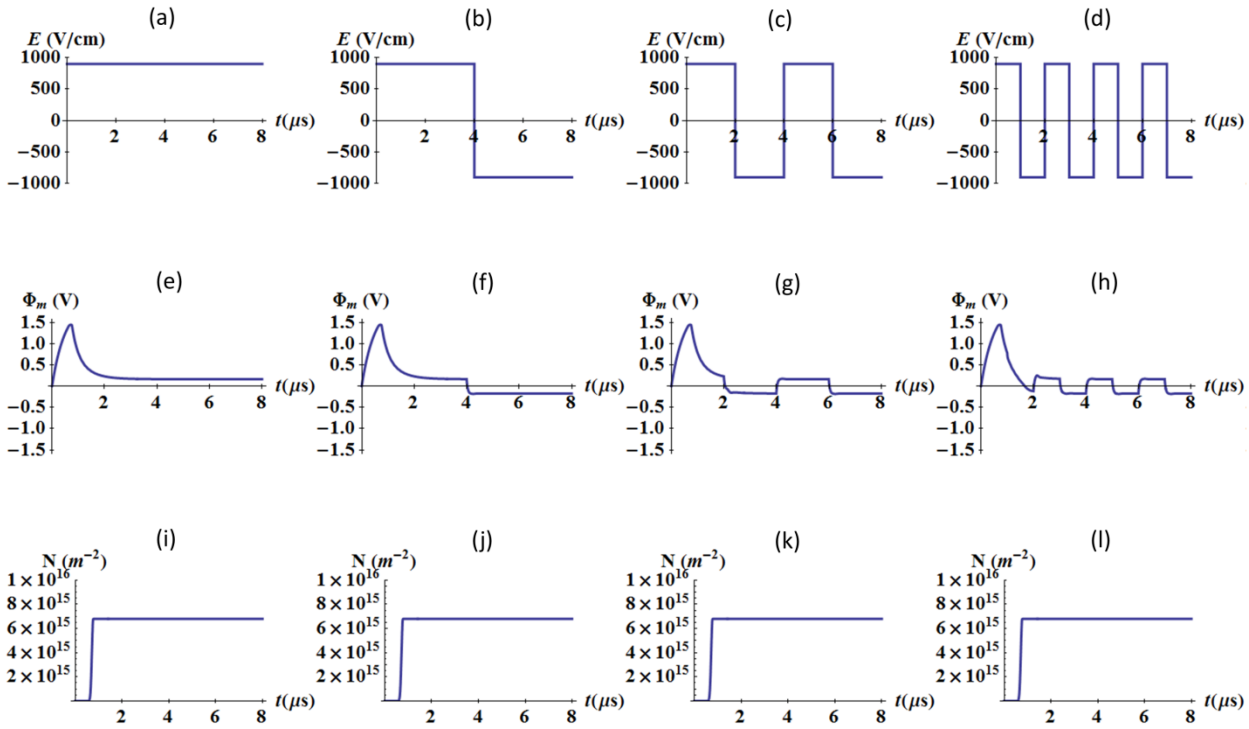

Figure 3.5. TMP and pore density during various bipolar PEFs. (a-d) Input signals with an amplitude of 900 V/cm. (e-h) Resulting TMP development as a function of time. (i-l) Resulting pore density as a function of time.

3.4 – Limitations and Conclusion

The results presented above provide strong evidence that high-frequency, bipolar pulses of sufficient amplitude can produce a structural rearrangement of the lipid bilayer membrane that is characteristic of electroporation. One limitation of the current model is that it does not allow for pore expansion or merging of pores. This may explain why having multiple pulse cycles in a burst has a minimal influence on the pore density over time (Fig 3.4 l). These features are incorporated in the model developed by Talele *et al*. (Talele et al., 2010), which does not include an organelle. In their work, all peaks in a two-cycle 1 MHz sinusoidal waveform significantly increase the pore radius over time. Future work will be directed towards including this feature in

the current model of a cell with an organelle, which will be a useful tool in designing appropriate pulsing protocols. It is likely that a burst of bipolar pulses will increase the extent of tissue electroporation when compared to a single cycle.

4 – Modeling the Effects of High-Frequency Pulsed Electric Fields on Whole Tissues[1]

4.1 – Introduction

Common protocols for IRE, ECT, and EGT involve delivering multiple, unipolar pulses with a duration on the order of microseconds through electrodes inserted directly into, or adjacent to, the malignant tissue. When the tumor is located deep within an organ, a minimally invasive needle or catheter based device is needed for the electrodes to reach the tumor. In some instances, the organ puncture required by these designs can, in itself, damage the surrounding healthy cells (Lamsa et al., 2009). There is also the possibility of reseeding cancer cells upon device removal. Therefore, the use of non-puncturing plate electrodes placed around the organ is desirable in some instances. Plate electrodes are best suited to treat tumors lying close to the skin, because a high potential drop occurs across the skin, where the field is the largest, limiting the amount of deeper tissue that can be permeabilized without first permeabilizing the skin (N. Pavselj et al., 2005; N. Pavselj et al., 2007). However, the high electric field in the skin can lead to deleterious thermal damage through the mechanism of Joule heating (R. C. Lee et al., 1996). Plate electrodes will have similar problems when placed around internal organs to treat tumors. Most organs are covered by the peritoneum, where the presence of tight junctions concentrates the field across epithelial cells, because extracellular current pathways are reduced (Jones et al., 2003). We hypothesize that these problems can be mitigated by implementing high-frequency bursts of bipolar pulses with a burst width on the order of microseconds and a duration of single polarity on the order of nanoseconds.

[1] Chapter 4 is adapted and reprinted with permission. © 2011 IEEE. Arena, C. B., Sano, M. B., Rylander, M. N., and Davalos R. V., Theoretical Considerations of Tissue Electroporation with High-Frequency Bipolar Pulses, IEEE Transactions on Biomedical Engineering, 58(5), 1474-1482, May 2011.

To the best of our knowledge, the benefits of bipolar pulses have only been studied for electroporation applications at the single-cell level. Theoretically, Talele *et al*. have shown that asymmetrical electroporation due to the resting TMP (~0.1 V) (Gowrishankar et al., 2006) of cells seen when unipolar pulses are delivered (D. C. Chang, 1989; Tekle et al., 1991) can be alleviated by switching to bipolar pulses (Talele et al., 2007). Experimentally, this leads to increased efficiency of macromolecule uptake through the membrane (D. C. Chang, 1989; Tekle et al., 1991). Depending on the extracellular conductivity, bipolar pulses with a frequency of 1 MHz (i.e. 500 ns duration of single polarity) can also lessen the dependence of electroporation on cell size (Gaynor et al., 1995), allowing more cells to be electroporated (Talele et al., 2008; Talele et al., 2010). In general, pore formation increases as long as the TMP is sustained above a critical threshold (~1 V) (Gowrishankar et al., 2006). One drawback of bipolar pulses is that they require higher field strengths to induce a given TMP as compared to a unipolar pulse of equivalent duration (see Chapter 3). This is accentuated when the frequency of the bipolar pulses is increased, because the time interval above the critical TMP is reduced (Talele et al., 2010). Kotnik *et al*. have explored the benefits of bipolar pulse trains at significantly lower frequencies, up to 1 kHz (i.e. 500 μs duration of single polarity). At lower frequencies, theoretical results show that the pore formation symmetry can also be normalized with bipolar pulses (T. Kotnik, Mir, et al., 2001). Experimentally, bipolar pulses reduce electrolytic contamination (T. Kotnik, Miklavcic, et al., 2001) and the required field strength for reversible electroporation, while the field strength required for IRE remains unchanged (T. Kotnik, Mir, et al., 2001). The authors attribute this to the fact that when the duration of single polarity is much longer than the plasma membrane charging time, permeabilized area differences on the membrane between unipolar and bipolar pulses decreases as pulse amplitude increases.

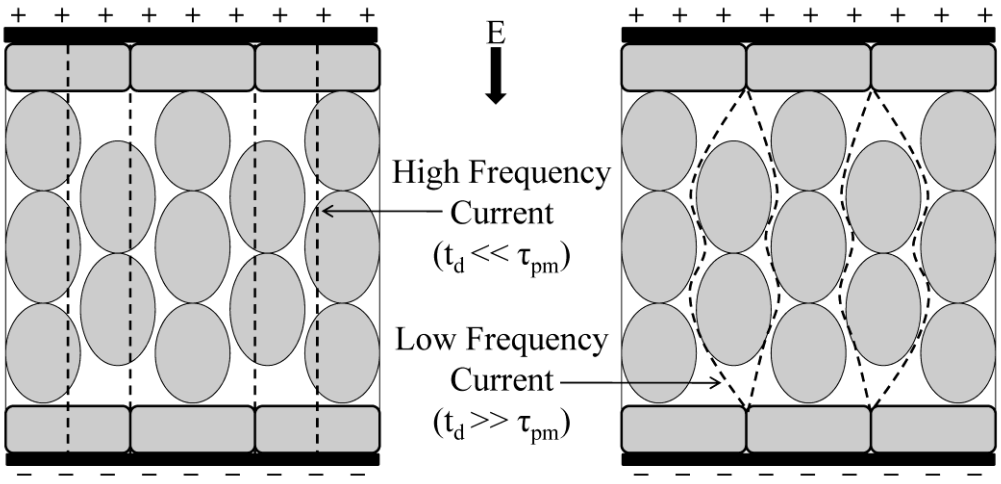

Figure 4.1. Illustration of current pathways through epithelial layers and bulk tissue prior to the onset of electroporation. When the pulse duration (t_d) is much less than the plasma membrane time constant (τ_{pm}), current flows through both intracellular and extracellular spaces (left). In the case that t_d is much greater than τ_{pm}, current flow is restricted to the narrower extracellular spaces (right).

Here, the benefits of high-frequency, bipolar pulses for electroporation of tissue enclosed by an epithelium are studied. Epithelial layers containing tight junctions are preferred sites of electroporation for pulses with duration on the order of microseconds (Gowrishankar et al., 2004; Gowrishankar et al., 2003). This has to do with the fact that the electric current associated with pulses longer than the charging time of the plasma membrane (~1 μs) (Gowrishankar et al., 2006) is confined to narrow, high resistance extracellular spaces prior to the onset of electroporation (Figure 4.1) (Esser et al., 2007; Ivorra, 2010). It is possible for the field to penetrate epithelial layers when nanosecond pulsed electric field (nsPEF) are employed, because current can flow through both extracellular and intracellular spaces (Gowrishankar et al., 2003; Ivorra, 2010). In this case, all cells present in the organ, regardless of their packing and morphology, experience a macroscopically homogeneous electric field distribution (Esser et al., 2009) (microscopic non-uniformities in the electric field are still present due to the packing of individual cells comprising the tissue). Therefore, high-frequency, bipolar pulses with a duration of single polarity on the order of nanoseconds can be applied to treat tissue layers underlying the

skin (Figure 4.2). Further, because the field is not concentrated across the epithelial cells, the potential for thermal damage in the skin should be reduced.

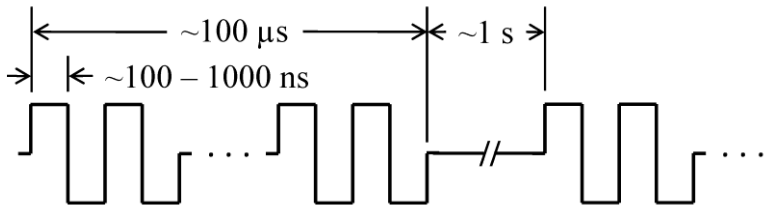

Figure 4.2. Typical pulsing protocol for the proposed electroporation-based therapy. The total burst width of the high-frequency pulses (~100-1000 ns duration of single polarity) is on the order of hundreds of microseconds, the time delay in between bursts is on the order of seconds, and the total number of bursts can be adjusted.

To quantify these apparent benefits, a finite element model (FEM) simulating plate electrodes surrounding a cylindrical tissue section through the center of a skin fold was constructed. Electroporation is often used to treat tumors that arise in fat tissue lying close to the skin (Mir et al., 1997). The FEM incorporates physics for determining the electric field and temperature distribution within the heterogeneous system. Additionally, the electric field data generated was substituted into analytical calculations of TMP in order to determine the relationships between pulse frequency and the extent of electroporation in the different tissue layers.

4.2 – Methods

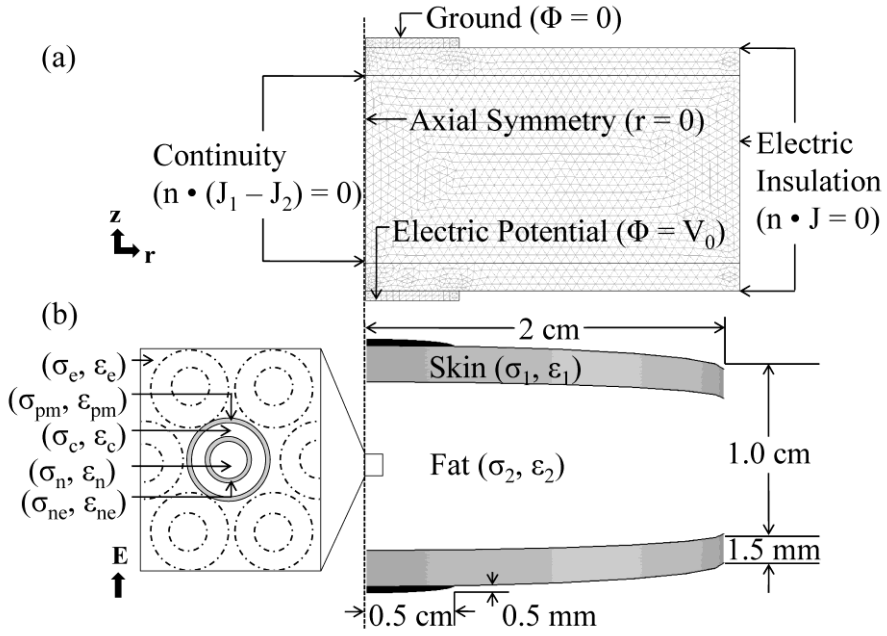

Figure 4.3. (a) Meshed geometry of the FEM with boundary settings, and (b) schematic diagram of the geometry with dimensions. The mesh consists of 3028 elements and was refined until there was < 0.1% change in the magnitude of the electric field at the center of the tissue. The box represents an expanded view of the tissue that describes the link between the macroscopic electric field (*E*) and the microscopic analysis of TMP. Adjacent cells are drawn with dashed lines, indicating their role was ignored in calculating TMP.

A 2D axisymmetric FEM representative of a cylindrical section of non-infiltrated fat encapsulated by dry skin (Figure 4.3) was simulated using COMSOL Multiphysics (version 3.5, Burlington, MA). The electric potential distribution within the tissue was obtained by transiently solving:

$$0 = -\nabla \cdot (\sigma \nabla \phi) - \varepsilon \nabla \cdot \left(\frac{\partial \nabla \phi}{\partial t}\right) \qquad (1)$$

whose derivation was discussed in Chapter 3. The dielectric properties of the bulk tissue (Table 4.1) were chosen from data generated by Gabriel *et al*. (S. Gabriel et al., 1996) available online (http://niremf.ifac.cnr.it/docs/dielectric/home.html). The data was interpolated in Mathematica 7 (Wolfram Research, Inc.) in order to estimate the dielectric properties at the desired frequencies.

Dielectric properties of the electrode were chosen to be stainless steel, as incorporated in the COMSOL material library. All electrical boundary conditions are shown in Figure 4.3.

Table 4.1. Dielectric properties of the FEM simulation domain

Frequency (Pulse Duration)	Waveform	Property	Tissue	
			Skin	Fat
250 kHz (2 μs)	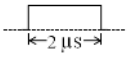	σ (S/m)	0.00216	0.0263
		ε_r	888	47
500 kHz (1 μs (×2))	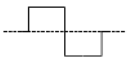	σ (S/m)	0.00485	0.0265
		ε_r	851	33
1 MHz (500 ns (×4))	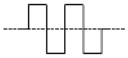	σ (S/m)	0.0119	0.0267
		ε_r	792	25
2 MHz (250 ns (×8))	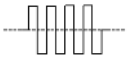	σ (S/m)	0.0290	0.0270
		ε_r	700	20

Because rectangular waveforms are comprised of components with various frequencies and amplitudes, tissue properties at frequencies associated with the frequency, defined as the inverse of twice the duration of single polarity, are chosen. Intuitively, the duration of single polarity defines the frequency at which the current changes direction in the tissue. The pulses were constructed by multiplying the applied voltage by a function consisting of two smoothed Heaviside functions with a continuous second derivative and a tolerance of 5 ns (rise and fall times). The quasi-static assumption is confirmed based on the fact that the primary frequency of the pulses is lower than 200 MHz (rise and fall times), which corresponds to a wavelength that is greater than the longest dimension in the geometry (Chen et al., 2009). The inclusion of a permittivity term in (1) differs from previous, simplified models (J.F. Edd et al., 2007; R. E. Neal, 2nd et al., 2009), and accounts for reactive component of tissue to time dependent pulsing, which is required for obtaining accurate potential distributions in heterogeneous models (Yousif et al., 2008).

The temperature distribution in the tissue was obtained by transiently solving a modified version of the Pennes bioheat equation (Pennes, 1948) with the inclusion of a Joule heating term:

$$\rho c \frac{\partial T}{\partial t} = \nabla \cdot (k \nabla T) + \rho_b w_b c_b (T_b - T) + Q_m + |J \cdot E| \qquad (2)$$

where T is the tissue temperature, T_b is the blood temperature, k is the thermal conductivity of the tissue, c and c_b are the tissue and blood specific heat, respectively, ρ and ρ_b are the tissue and blood density, respectively, Q_m is the metabolic heat source term, ω_b is the blood perfusion coefficient, and $|J \cdot E|$ is the Joule heating term. All thermal tissue properties are given in Table 4.2 (Fiala et al., 1999). Due to the presence of different tissue layers and the high frequencies under consideration (250 kHz – 2 MHz), displacement currents are considered along with conduction currents in the formulation of Joule heating:

$$J = J_D + J_C = \varepsilon_0 \varepsilon_r \frac{\partial E}{\partial t} + \sigma E \quad (3)$$

where J is the total current density, J_D is the displacement current density, and J_C is the conduction current density. In order to ensure that negative current components due to polarity changes add to the total current in the tissue, the absolute value of the resistive heating term was taken prior to temperature calculations. It was assumed that all subdomains were initially at physiologic temperature (T_0 = 310.15 K). The boundaries between the electrode-skin interface and the skin-fat interface were treated as continuous ($n \cdot (k_1 \nabla T_1 - k_2 \nabla T_2) = 0$), the centerline was defined as axial symmetry (r = 0), and the remaining boundaries were thermally insulated ($n \cdot (k \nabla T) = 0$) for conservative temperature estimates. Temperature profiles were investigated along the centerline (r = 0 mm) in the middle of the fat (z = 0 mm) and skin (z = 5.75 mm) layers. Data was imported into Mathematica, and a moving average with a period of 100 ns was taken to smooth the plots. Additionally, the data was fit with a linear trendline in order to extrapolate to longer burst widths and predict the onset of thermal damage.

Table 4.2. Thermal properties of the FEM simulation domain

Property	Tissue		
	Blood	Skin	Fat
ρ (kg/m^3)	1069	1085	850
c (J/(Kg · K))	3650	3680	2300
k (W/(m · K))	-	0.47	0.16
ω (1/s)	-	1.1	0.0036
Q_m (kg/m^3)	-	368	58

The analytical solution for induced TMP across the plasma membrane was calculated as described in the previous chapter, without the inclusion of dynamic membrane properties due to pore formation. Additionally, the natural, resting component of the plasma membrane TMP was ignored in all simulations, because it is typically an order of magnitude less than the induced TMP (Gowrishankar et al., 2006). Further, the TMP across the nuclear envelope never reached a permeabilizing threshold with the chosen pulsing protocols, and reference to TMP for the remainder of this chapter refers only to the plasma membrane. The geometric and dielectric properties of the cellular regions are given in Table 4.3 (Hu et al., 2005). Dielectric properties at the cellular level are assumed to be frequency independent, which is valid for predicting TMP up to around 100 MHz (T. Kotnik et al., 2000).

Table 4.3. Dielectric properties of the analytical TMP calculation

Region	σ (S/m)	ε_r	Dimensions
Extracellular Space	0.6	80.0	-
Plasma Membrane	5.3×10^{-6}	7.0	7.0×10^{-9} (thickness)
Cytoplasm	0.13	60.0	5.0×10^{-6} (radius)
Nuclear Envelope	4.3×10^{-3}	22.8	40.0×10^{-9} (thickness)
Nucleoplasm	0.18	120.0	2.5×10^{-6} (radius)

The analytical model was utilized in two instances. In the first scenario, the frequency dependence of the induced TMP was investigated. Both rectangular and sinusoidal electric fields with identical maximum amplitude were compared. Rectangular waveforms were constructed in Mathematica with a series of step functions (ideal rise time) of alternating polarity and duration, and sinusoidal waveforms were constructed with a single sine function of varying frequency. This analysis provided insight as to which pulse waveforms and frequencies should be simulated by the FEM.

In the second case, TMP profiles were investigated around a hypothetical cell located along the centerline (r = 0 mm) in the middle of the fat (z = 0) and skin (z = 5.75 mm) layers of the FEM. The equations for TMP are derived under the assumption that there is no influence on the microscopic electric field from neighboring cells. Therefore, the macroscopic electric field in the bulk tissue predicted by the FEM dictates the microscopic electric field experienced by the cell. The vertical z-component of the electric field was imported from the specific locations within FEM into Mathematica to account for polarity changes. The radial r-component was neglected due to the fact that it never surpassed 3 V/cm as current traveled primarily in the z-direction. Non-uniform electric field data was fit with a series of step functions (50 ns duration), such that the Laplace transform of the field could be performed and the solution for TMP could be obtained in the frequency domain as the summation of individual steps. The inverse Laplace transform of the data was then taken to obtain the complete time courses.

4.3 – Results

Results of the parametric study on TMP for frequencies spanning from 62.5 kHz to 16 MHz are shown in Figure 4.4. The maximum amplitude of the sinusoidal and bipolar rectangular electric fields was 2000 V/cm (peak). For this applied field and the given geometric and

dielectric properties of the modeled cell, the TMP never exceeds 1.46 V. Additionally, the time constant of the plasma membrane is 345 ns. All measurement were taken at the cell pole ($\theta = 0$) to depict the maximum achieved TMP after the system reached a steady oscillatory state. From the curve, as the frequency increases, the magnitude of the TMP is reduced. For the sinusoidal waveform, the reduction is evident at lower frequencies compared to the rectangular waveform. This has to do with the fact that the rectangular waveform maintains its maximum amplitude for a longer period of time than the sinusoidal waveform. It is not until the frequency of the rectangular waveform surpasses 250 kHz that a dramatic decrease in TMP occurs. For this reason, only rectangular pulses in a frequency window of 250 kHz to 2 MHz were investigated in the FEM, since they are best suited for electroporation with high-frequency, bipolar pulses.

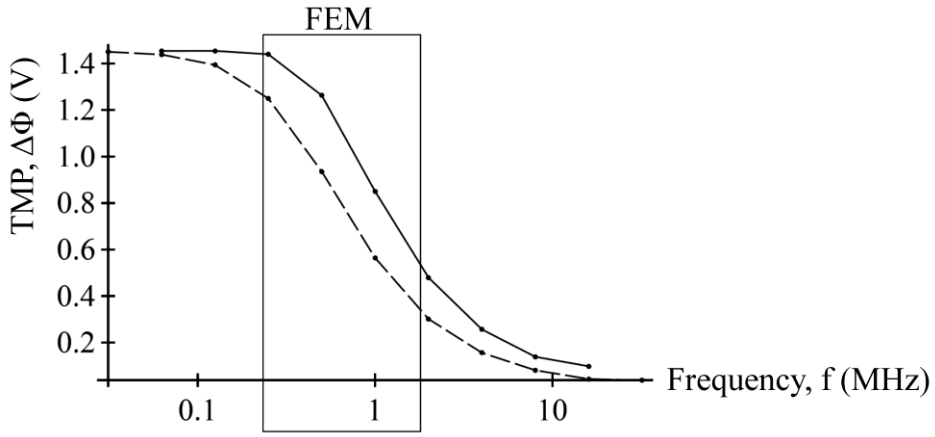

Figure 4.4. Frequency (f) response of the TMP. Values are taken at the cell pole ($\theta = 0$) for rectangular bipolar pulses (—) and sinusoidal waveforms (– –). The box illustrates the frequency window implemented in the FEM

Figure 4.5 shows the electric field distribution at the end of a 2 μs burst with various frequencies given in Table I. In each case, the maximum applied voltage was set to 2600 V (peak) in order to set up a voltage to distance ratio of 2000 V/cm between the electrodes (1.3 cm spacing). From the surface contour map, as frequency is increased, the electric field in the fat rises while the field in the skin drops. This trend extends to the point that at 2 MHz the field in the skin is lower

than the fat, which is a direct result of the tissue dielectric properties at that frequency (greater conductivity and permittivity of skin as compared to fat). Therefore, high-frequency fields, or pulses with shorter duration, are better suited to penetrate epithelial layers, such as the skin, and reach underlying tissue.

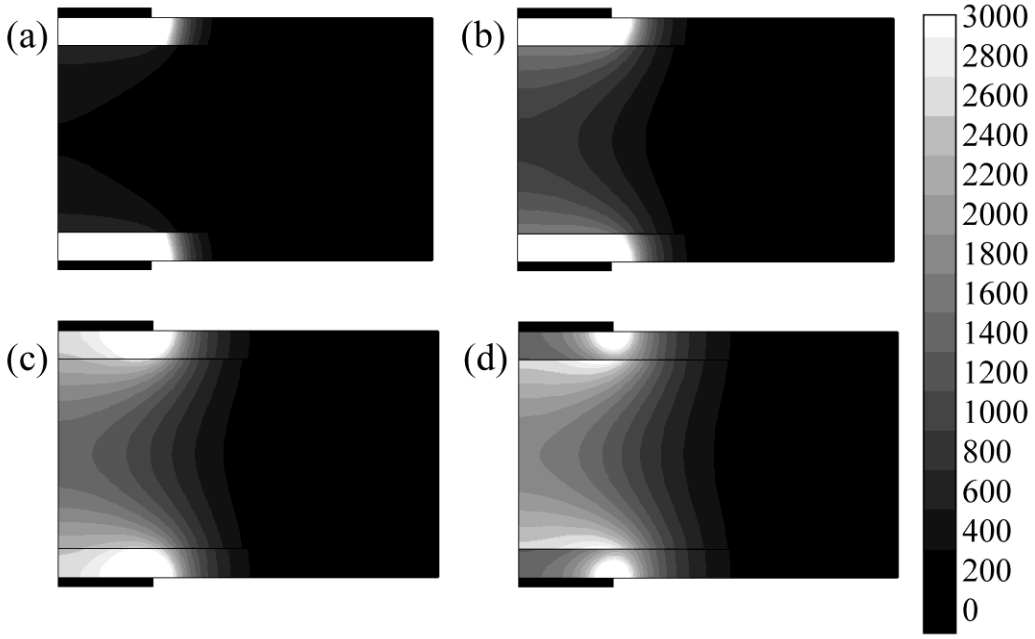

Figure 4.5. Electric field, norm (V/cm) contours predicted by the FEM. Values are taken at the end of a 2 μs burst with an amplitude of 2600 V and a frequency of 250 kHz (a), 500 kHz (b), 1 MHz (c), and 2 MHz (d).

Temperature changes predicted by the FEM at the center of the skin and fat are shown in Figure 4.6. In this case, a burst width of 4 μs was simulated in order to capture the trends in temperature development. Polarity of the 2 μs pulse (250 kHz) was switched between pulses to maintain consistency with the other waveforms that are inherently bipolar. With respect to the skin, as the frequency of the applied field increases, the temperature rises at a slower rate. This is a consequence of the fact that the electric field within the skin also decreases with increasing frequency. In the case of the fat, the temperature rises at a faster rate when the frequency of the applied field is increased. At first glance, this seems to be detrimental, however, it is merely an indication that energy is preferentially being deposited into the fat at higher frequencies. Again,

this can be correlated to the electric field profile. In both tissues, the sharp rises in temperature are due to the spikes in displacement current that occur at the onset and offset of each pulse (data not shown). The total temperature increase in all cases is less than 0.003 K for a burst width of 4 μs. As explained in the discussion, even for bursts of longer widths, the temperature increase is not enough to promote thermal damage.

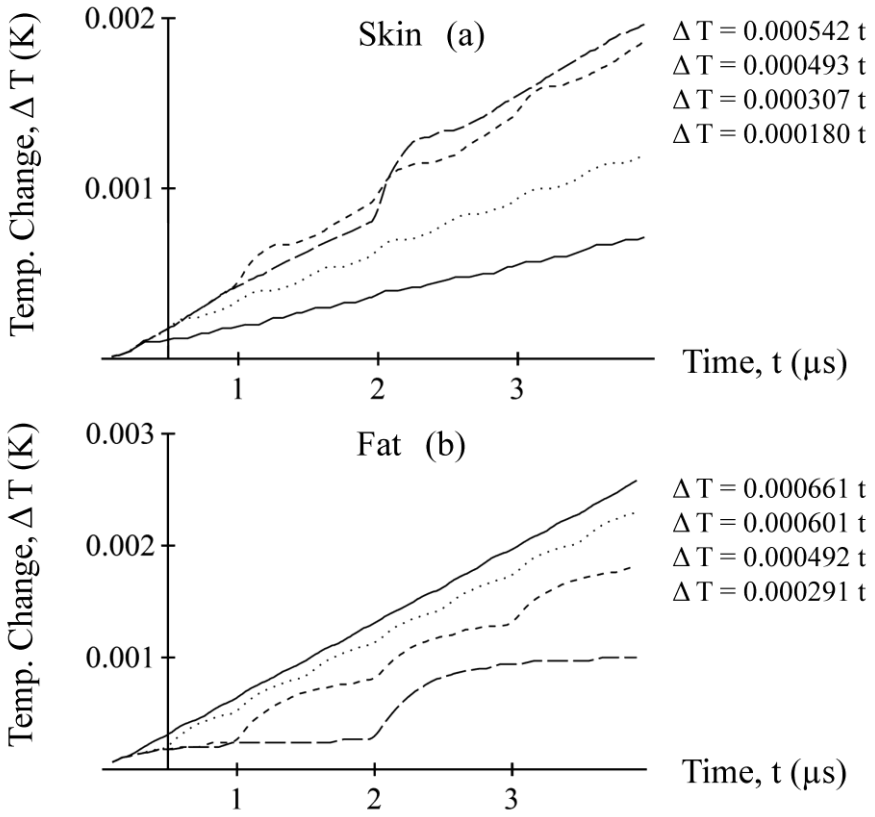

Figure 4.6. Temperature changes predicted by the FEM. Values are taken at the center of the skin (a) and fat (b) for frequencies of 250 kHz (— —), 500 kHz (- - -), 1 MHz (· · ·), and 2 MHz (—). Equations represent a linear fit to the data.

TMP profiles as predicted by the FEM on a hypothetical cell at the center of the skin and fat for a 2 μs burst width are shown in Figure 4.7. All measurement were taken at the pole ($\theta = 0$) to depict the maximum induced TMP around the cell. With respect to the skin, as the frequency of the applied field increases, the maximum oscillation amplitude of the TMP decreases. This occurs for two reasons. First, as seen in Figure 4.5, the electric field in the skin decreases with

increasing frequency. Second, as seen in Figure 4.4, even with constant field amplitude, the TMP decreases with increasing frequency, because the time during which the membrane has to charge before the polarity switches is less at higher frequencies. In the case of the fat, the behavior is slightly more complex. At lower frequencies, a majority of the voltage drop occurs across the skin, resulting in a reduced electric field in the fat. This shielding effect is best shown in Figure 4.7 along the 250 kHz trace. According to Figure 4.4, at 250 kHz, the maximum TMP should be reached. However, due to the shielding effect from the skin, a reduction in the TMP prior to the polarity change is seen. This reduction in TMP can be alleviated by increasing the frequency of the applied field. However, the tradeoff between increased frequency and reduced TMP is still evident at a frequency of 2 MHz (250 ns pulse duration).

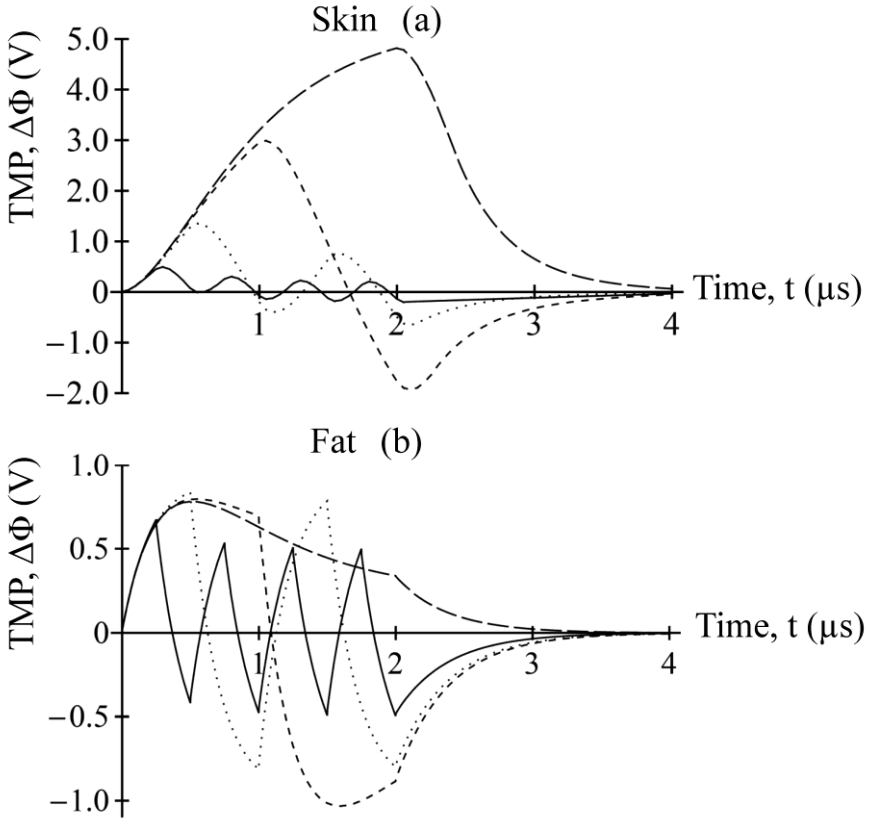

Figure 4.7. TMP predicted by the FEM. Values are taken at the center of the skin (a) and fat (b) for frequencies of 250 kHz (— —), 500 kHz (- - -), 1 MHz (· · ·), and 2 MHz (—).

4.4 – Discussion

As mentioned, electrical current associated with pulses longer than ~1 µs is confined to extracellular spaces prior to the onset of electroporation (Figure 4.1) (Esser et al., 2007; Ivorra, 2010). This can be attributed to the migration of charges towards biological membranes following the application of an external electric field. The time required for a membrane to become charged to 63% of its steady state value is defined as the charging time constant of the membrane (τ_{pm}). Based on the analytical model for TMP in this study, the time constant of the plasma membrane for a constant field (2000 V/cm) is 345 ns. Additionally, steady-state is not reached until after 1 µs. Displacement currents across the plasma membrane allow organelles to be exposed to fields during the time that it takes the plasma membrane to reach steady state (Esser et al., 2009). Once steady state is achieved, the counter-field developed along the plasma membrane due to the accumulation of charges is significant enough to shield the field from entering the cell, and current is directed through extracellular spaces. Only after permeabilization of the membrane does ionic conduction allow the field to re-enter the cell (Kolb et al., 2006). If extracellular current pathways between cells are reduced, as in layers of epithelial cells connected by tight junctions (Jones et al., 2003), the field is highly concentrated across the layer, and the extent of electroporation in underlying cells is reduced.

There is a balance between employing pulses that are delivered on a short enough timescale to flow through epithelial cells but are long enough to induce electroporation in underlying cells. The time constant of 345 ns falls between the 2 MHz (250 ns pulse duration) and 1 MHz (500 ns pulse duration) bursts. Further, the 500 kHz burst (1 µs pulse duration) is close to the time it takes the TMP to reach steady state. Table 4.4 summarizes the results based on the time that the TMP on a hypothetical cell at the center of the fat layer is above 0.5 V. This

amplitude was chosen such that even the highest frequency burst was above the set voltage level for a certain amount of time. The results would hold if the applied field was doubled and the voltage level was set to the 1 V threshold for pore formation, due to the linear dependence of TMP on the electric field. Based on this criterion, a frequency of 500 kHz is best suited to treat cells in the fat layer, followed by 1 MHz and 250 kHz. As frequency is increased, the dielectric properties and electric field distribution in the skin and fat become more macroscopically homogeneous, but above 1 MHz, the pulse duration is not adequate for the cell to charge.

Table 4.4. Pulse frequency-TMP comparison in fat layer

Frequency (pulse duration)	Time (μs), |TMP| > 0.5 (V)	% of Pulse, |TMP| > 0.5 (V)
250 kHz (2 μs)	1.2	60
500 kHz (1 μs (×2))	1.9	95
1 MHz (500 ns (×4))	1.3	65
2 MHz (250 ns (×8))	0.1	5

According to *in vitro* experiments that utilize bipolar rectangular pulses, the typical burst width required to induce either reversible electroporation or IRE increases with the frequency of the applied field. For EGT, a 60 kHz bipolar square with a burst width of 400 μs and an amplitude of 1600 V/cm has a six times greater transfection efficiency than a 1 MHz bipolar square wave with equal amplitude and width (Tekle et al., 1991). In terms of IRE, a 60 kHz bipolar square with a burst width of 400 μs and an amplitude of 4000 V/cm results in 19 % cell viability (Tekle et al., 1991). These results were obtained when a single burst was delivered to the sample, and we were unable to find any data on high-frequency electroporation with rectangular pulses that implemented multiple bursts. Similar to how multiple unipolar pulses are typically delivered in ECT, EGT, or IRE protocols to enhance the desired outcome (Belehradek et al., 1994; Garcia et al., 2010), multiple bipolar bursts would likely produce similar trends.

Data is also available for burst sinusoidal waveforms in the frequency range of 2 kHz to 50 MHz (Jordan et al., 2004; Katsuki et al., 2007), but the results are inconclusive, and sinusoidal waveforms are less efficient than rectangular bipolar pulses for inducing electroporation (T. Kotnik et al., 2003).

The onset of protein denaturation and loss of cell structure occurs above 318.15 K (Bilchik et al., 2001), which correlates to an increase in temperature of 8 K above physiological temperature. Using this information, we can calculate the maximum energy delivery period (number of pulses multiplied by pulse duration) for an amplitude of 2000 V/cm at each of the frequencies investigated using the trendlines generated by the FEM data (Figure 4.6). In the skin layer, heating is reduced by increasing the frequency of the applied field. This confirms our initial hypothesis that the potential for thermal damage in the skin is reduced when the frequency of the applied field is increased. At higher frequencies, the energy is preferentially deposited in the fat layer. For 2 MHz, the total energy delivery period required to cause an 8 K increase in temperature is 12 ms. An example treatment plan would then be 12, 1 ms pulses separated by a delay of 1 s. If the frequency is reduced to 500 kHz, which shows the greatest electroporation efficiency (Table 4.4), the allowable energy delivery period increases to 16 ms, which would permit the delivery of an additional 4, 1 ms pulses before the onset of thermal damage. The restrictions could be increased if less conservative estimates are obtained that account for heat dissipation between pulses and heat convection at the tissue surface (Lackovic et al., 2009). These projected protocols represent a maximum, and it is likely that the desired effects will be induced at a significantly lower energy (Belehradek et al., 1994; Garcia et al., 2010).

This work has been geared towards developing a better way to deposit electrical energy through the skin, but similar structures are seen in underlying tissue layers. For example,

pancreatic ducts are lined by epithelial cells that can give rise to tumors, and tumors of the breast are often surrounded by fatty tissue (Surowiec et al., 1988). These features will play an important role in how the electric field is distributed within the tissue. This complicates treatment planning, where the goal is to predict the electric field distribution in the tissue in order to select the appropriate pulsing protocol. A benefit of high-frequency bursts with nanosecond order pulses is their ability to penetrate tissue heterogeneities, resulting in more predictable treatment outcomes. These pulsing protocols would then be useful not only if implemented with plate electrodes, but also the alternative needle electrodes.

Detailed geometric considerations, such as the individual tissue layers comprising the skin, layers of conductive gel used clinically to improve electrical contact, and the outer curvature of a typical skin fold have been ignored in order to simplify our initial investigation. To be conservative in our estimates, dry skin was used in the model and the use of a conductive gel to wet the skin was not employed. The use of a gel and the properties of wet skin should further enhance the benefits of this technique. In this initial study, our goal was to elicit the benefit of high-frequency electroporation for overcoming impedance barriers without superimposing the effects from geometric intricacies and electroporation nonlinearities in the analysis. Future work should be directed towards expanding this focus.

In the analytical model for TMP, it was assumed that the electric field was applied across an isolated cell. In reality, tissues are comprised of a network of cells that create non-uniformities in the electric field at the microscopic level. In general, as the packing density of cells increases, the TMP decreases (Susil et al., 1998). Thus the overall trends presented here are valid, but the specific values for TMP should be scaled accordingly if the packing density is known. Additionally, dynamic dielectric tissue properties were neglected in both the analytical

model and FEM. At the macroscale, changes in tissue dielectric properties due to electroporation and temperature should be incorporated in the FEM. At the microscale, in order to prevent the development of unrealistic TMP in regions of high electric field, as seen here in the skin layer, the analytical calculation of TMP could be supplemented with equations for pore formation. Pores allow current to flow through the membrane, which limits the increase in TMP (Talele et al., 2008, 2007; Talele et al., 2010).

4.5 – Conclusion

Our results indicate that bursts of bipolar, nanosecond pulses can maintain a critical TMP beneath epithelial layers, while minimizing heating in the epithelial layer. This has to do with the ability of nanosecond pulses to achieve a macroscopically homogeneous field distribution in a heterogeneous system. At high frequencies, tissues with a low passive DC conductivity become more conductive. This has implications not only for skin, as presented here, but for other tissues, such as bone and lung. Experimental work needs to be conducted to optimize the total burst width, time between bursts, and total number of bursts required for inducing electroporation with high-frequency rectangular pulses. This study serves as the first step in assessing the feasibility of implementing high-frequency, bipolar pulses for tissue electroporation. Based on the theoretical analysis presented here, the predicted benefits of high-frequency electroporation will translate experimentally to enhance the efficacy of ECT, EGT, or IRE for treating electrically isolated tumors, such as those encapsulated by the skin, bone, pancreas, or lung.

5 – Evaluating the *In Vivo* Response of Brain Tissue to H-FIRE[2]

5.1 – Introduction

Here, we build on our theoretical results and investigate the *in vivo* potential of high-frequency, bipolar bursts to kill tissue through IRE. As opposed to traditional IRE that uses unipolar pulses (Figure 5.1a) synchronized with the heartbeat, we postulate that IRE can be achieved with a series of high-frequency, bipolar bursts (Figure 5.1 b and c) delivered at the same repetition rate. To the best of our knowledge, these types of waveforms have not been investigated for therapeutic IRE applications. Lesions are developed in healthy rat brain tissue with waveforms having center frequencies up to 500 kHz, which maintain the potential to overcome impedance barriers posed by epithelial layers (Arena, Sano, Rylander, et al., 2011). Similar waveforms have been studied *in vitro* for reversible applications of electroporation, and were shown to counterbalance both electrolytic reactions for the prevention of electrode breakdown (T. Kotnik, Miklavcic, et al., 2001) and asymmetrical electroporation caused by the resting TMP (T. Kotnik, Mir, et al., 2001). Additionally, for a constant electric field applied to cell suspensions or monolayers, as the frequency of the squarewave is increased up to 1 MHz (duration of single polarity equal to 500 ns), cell death decreases (Tekle et al., 1991). We explore this trend *in silico* with an analytical model that predicts the TMP in response to an arbitrary electric field and *in vivo* with the treatment of brain tissue using H-FIRE with bipolar bursts at frequencies of 250 kHz and 500 kHz.

[2] Chapter 5 is adapted and reprinted under the Creative Commons License Deed. Open Access 2011 BioMed Central Ltd. Arena, C. B., Sano, M. B., Rossmeisl, J. H., Jr., Caldwell, J. L., Garcia, P. A., Rylander, M. N., and Davalos R. V., High-Frequency Irreversible Electroporation for Non-Thermal Ablation Without Muscle Contraction, BioMedical Engineering OnLine, 10(102), Nov 2011.

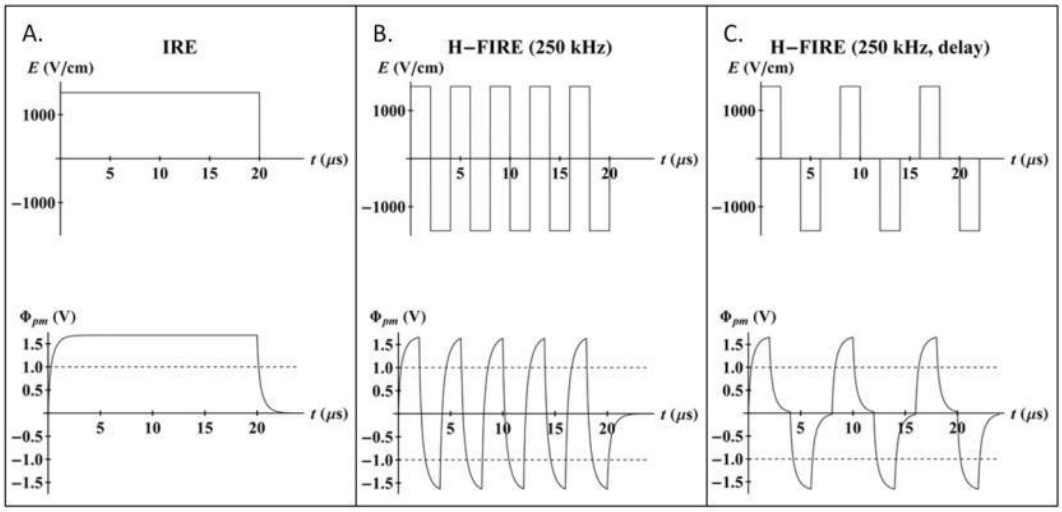

Figure 5.1. Characteristic waveforms of IRE and H-FIRE with the corresponding TMP development across the plasma membrane (Φ_{pm}). The 1500 V/cm unipolar pulse (a) causes the TMP to rise above the critical threshold for IRE (1 V, dashed line). The 1500 V/cm bipolar burst without a delay (b) and with a delay (c) causes the TMP to oscillate around the same critical threshold.

In conjunction with investigating the ability of H-FIRE to kill tissue, this work serves to evaluate its potential for reducing nerve stimulation. Currently, clinical applications of IRE require the administration of general anesthesia and paralytic agents in order to mitigate muscle contractions during each pulse (Ball et al., 2010). In some cases, without a sufficient dose of the paralytic agent, muscle contractions are still visible (Thomson et al., 2011). Muscle contractions may affect the location of implanted needle electrodes, which can invalidate treatment planning algorithms and prove harmful in treatments near vital structures. The threshold for nerve stimulation increases as the frequency of bipolar waveforms is increased (Reilly et al., 1985). An accelerometer based recording system was used to quantify muscle contractions during conventional IRE with unipolar pulses and H-FIRE at frequencies of 250 kHz and 500 kHz. Our results indicate that H-FIRE can non-thermally ablate tissue without causing muscle contractions. The non-thermal nature of the treatment is confirmed through both histological comparison to IRE controls and the development of a finite element model (FEM) for evaluating potential thermal damage in H-FIRE therapy of the brain.

5.2 – Methods

5.2.1 – Analytical Modeling of TMP

TMP development in response to a high-frequency electric field has been described in detail for a spherical cell with an organelle by Kotnik and Miklavčič (T. Kotnik et al., 2006). Here we extend this model to include squarewave bursts with a delay between the positive polarity and negative polarity pulses. This delay was implemented experimentally as a protective measure for the MOSFET based pulse generation system described below. The details of the model derivation can be found in Chapter 3. The cell specific parameters used here are shown in Table 5.1.

Table 5.1. Parameter values for TMP simulation

Quantity	Parameter	Value	Units	Reference
Conductivity	σ_e	1.2	S m^{-1}	(Sunderman, 1949)
	σ_{pm}	3×10^{-7}		(Gascoyne et al., 1993)
	σ_c	0.3		(Harris et al., 1983)
	σ_{ne}	3×10^{-7}		set equal to σ_{pm}
	σ_n	0.3		set equal to σ_c
Permittivity	ε_e	6.4×10^{-10}	A s V^{-1} m^{-1}	(Nortemann et al., 1997)
	ε_{pm}	4.4×10^{-11}		(Gascoyne et al., 1993)
	ε_c	6.4×10^{-10}		(Nortemann et al., 1997)
	ε_{ne}	4.4×10^{-11}		set equal to ε_{pm}
	ε_n	6.4×10^{-10}		(Nortemann et al., 1997)
Radius	R_c	7.5×10^{-6}	m	estimated from(Heizmann et al., 2001)
	R_n	5×10^{-6}		estimated from (Heizmann et al., 2001)
Thickness	d_{pm}	5×10^{-9}	m	(McLaughlin et al., 2005)
	d_{ne}	5×10^{-9}		set equal to (McLaughlin et al., 2005)

5.2.2 – Numerical Modeling of Temperature and Thermal Damage

A 3D finite element model (FEM) for calculating the temperature and potential thermal damage in brain tissue during IRE has been described in detail by Garcia *et al.* (Garcia, Rossmeisl, et al., 2011). A similar model has been developed here in COMSOL (version 4.2) for predicting the thermal response to the *in vivo* H-FIRE treatments. Specifically, the electric

potential distribution in the tissue was obtained by solving the time-harmonic continuity equation:

$$-\nabla \cdot [(\sigma + j\omega\varepsilon)\nabla\Phi] = 0 \qquad (1)$$

where ω is the angular frequency of the field. Equation 1 is developed from Maxwell's equations under the electro-quasistatic approximation, which is explained in Chapter 3. Dielectric tissue properties were chosen at 250 kHz to match the frequency of the waveform delivered experimentally in a majority of the H-FIRE trials. Data generated by Gabriel *et al.* for the conductivity and permittivity of grey matter (C. Gabriel et al., 1996) was interpolated in Mathematica in order to estimate the values at 250 kHz (Table 5.2). The electro-quasistatic assumption is validated based on the fact that the frequency of the field corresponds to a wavelength (3.5 m) and skin depth (0.5 m) that are greater than the longest dimension in the geometry (Chen et al., 2009). The brain subdomain was modeled as a 0.75 cm × 0.75 cm × 0.425 cm ellipsoid having a total volume of 1 cm^3 (Yücel et al., 2003). The maximum applied voltage, electrode dimensions, exposure length, and spacing were modeled to match the *in vivo* configuration described below. Electric potential boundary conditions of Φ = 400 V and Φ = 0 V were applied on the energized and grounded portions of the electrodes, respectively, while the remaining boundaries were treated as electrically insulating ($-n \cdot J = 0$), where J is the current density. The electrode subdomain was subtracted from the brain subdomain for conservative temperature estimates by preventing any heat dissipative fin effects. A fine mesh was utilized, which consisted of 23989 elements and resulted in less than a 0.5% difference in Joule heating between the electrodes upon further refinements.

Following a time-harmonic analysis of the electric field distribution, the temperature distribution in the brain was obtained by transiently solving the heat conduction equation with the inclusion of the predetermined Joule heating term ($J \cdot E = (\sigma + j\omega\varepsilon)E \cdot E$) as a heat source:

$$\frac{\partial T}{\partial t} = \frac{1}{\rho c_p}[\nabla \cdot (k\nabla T) + (J \cdot E)] \qquad (2)$$

where c_p is the specific heat capacity at constant pressure, k is the thermal conductivity, and ρ is the density of the tissue (Table 5.2). Terms associated with the Pennes' Bioheat equation that account for blood perfusion and metabolism commonly used to assess tissue heating during IRE have been neglected for conservative temperature estimates (Garcia, Rossmeisl, et al., 2011). Additionally, it was assumed that all subdomains were initially at physiologic temperature (37°C) and all boundaries were thermally insulating ($-n \cdot (-k\nabla T) = 0$).

Table 5.2. Parameter values for FEM simulation

Physics	Parameter	Value	Units	Reference
Heat conduction	k	0.565	W m^{-1} K^{-1}	(Duck, 1990)
	c_p	3680	J kg^{-1} K^{-1}	(Duck, 1990)
	ρ	1039	kg m^{-3}	(Duck, 1990)
Electric Currents	σ	0.145	S m^{-1}	(C. Gabriel et al., 1996)
	ε	1.95×10^{-8}	A s V^{-1} m^{-1}	(C. Gabriel et al., 1996)
Damage Processes	E_a	8.033×10^{5}	J mol^{-1}	(Floridi et al., 1993)
	ζ	1.676×10^{129}	s^{-1}	calculated from (Floridi et al., 1993; Wright, 2003)

Three different methods were evaluated for calculating Joule heating to determine which method was computationally efficient while generating accurate solutions during a 10 s test treatment. One method simulated ten IRE pulses (200 μs duration) at a repetition rate of one pulse per second. Another method modeled ten, 250 kHz H-FIRE bursts (200 μs on-time) at a repetition rate of one burst per second. In the last method, voltage was held constant, but the Joule heating term was scaled by the duty cycle of the burst (200×10^{-6}) for a 10 s simulation.

The parameters chosen had identical energized times, ensuring that equal quantities of energy were delivered to the tissue independent of the method used. The scaled Joule heating approach was eventually adapted for predicting the temperature increase during the entire H-FIRE protocol implemented experimentally, due to the slightly conservative yet accurate temperature distributions that were calculated in a fraction of the simulation time of the other two methods (data not shown). This technique also eliminates the need for an adaptive time stepping algorithm required to resolve microsecond order pulses that occur on the order of seconds. To account for the experimental condition of 180 bursts delivered at a rate of one per second, the Joule heating term was multiplied by the duty cycle (200×10^{-6}) and the simulation was run for 180 s.

Based on the temperature distribution, the extent of potential thermal damage in the brain was quantified at each time step using the Arrhenius equation:

$$\Omega(\mathrm{t}) = \int \zeta e^{-E_a/(R\,T(t))} dt = \int F\, dt \qquad (3)$$

where ζ is the frequency factor, E_a is the activation energy, R is the universal gas constant, and $T(t)$ is the temperature distribution for a given time (t). Due to a lack of data in the literature on Arrhenius parameters for healthy brain, parameters were chosen from glioblastoma cells in the temperature range 40°C to 45°C (Floridi et al., 1993) (Table 5.2). It is important to note that only E_a is presented in (Floridi et al., 1993), and ζ was calculated based on a linear relationship between E_a and $\ln(\zeta)$ for mammalian cells (Wright, 2003). Thermal damage can include a variety of processes including cell death, microvascular blood flow stasis, and protein coagulation (Sherar et al., 2000), each of which have different parameter values. Here, we have chosen to model the Arrhenius parameters associated with cell death. In terms of finite element modeling of tissue damage, a damage integral value $\Omega = 1$ corresponds to a 63% probability of cell death at

a specific point, and a damage integral value Ω = 4.6 corresponds to 99% probability of cell death at that point (I. A. Chang et al., 2004). Equation 3 was incorporated into COMSOL by adding a general PDE solver mode and writing the forcing function (*F*) in logarithmic form:

$$F = e^{-\ln(\zeta) - E_a/(R\,T(t))} \qquad (4)$$

in order to prevent abrupt changes in the solver. Additionally, all boundaries in the domain were assumed to be insulating ($-n \cdot \Gamma = 0$), where Γ is the general flux vector, which was assumed to be zero.

5.2.3 – In Vivo Experiments

H-FIRE was performed using a custom pulse generator (Figure 5.2). Two commercially available monopolar high voltage MOSFET switches (HV1000, Directed Energy, Inc., Fort Collins, CO, USA) were modified so that their outputs would withstand a pulse of opposite polarity. When triggered with a positive 5 V signal, these generators deliver a corresponding positive (HV1000P) or negative (HV1000N) pulse. An unregulated DC power supply was constructed to maintain a sufficient level of charge to deliver 20 A over a 100 μs burst. A center tapped 400 VA transformer (AS-4T320, Antek, Inc., North Arlington, NJ, USA) was rectified and smoothed by a capacitor bank to provide positive and negative power rails to the HV1000P and HV1000N, respectively. The voltage rails were controlled by adjusting the input voltage using a variable transformer, and the maximum output rating of the system was +/- 450 V. For each treatment, an arbitrary function generator (AFG3011, Tektronix, Beaverton, OR, USA) was used to define the parameters of the pulse train to be delivered. A delay equal to the duration of single polarity was included between the pulses in order to protect the MOSFETs from ringing. A unity gain inverting amplifier (AD844, Analog Devices, Norwood, MA, USA) was used to

invert this signal and appropriately trigger the negative pulse generator. The outputs of the two monopolar pulse generators were terminated into a 50 Ω load in parallel with the electrodes. This load was used to maintain appropriate pulse characteristics and as a safety to ensure the system was never triggered without an attached load. For comparison, the IRE treatments were performed using the BTX ECM 830 electroporation system (Harvard Apparatus, Holliston, MA, USA).

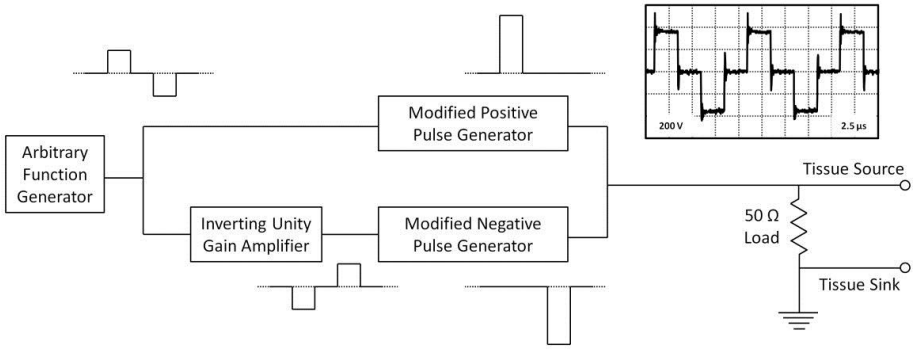

Figure 5.2. Schematic diagram of the pulse generation system. The example output is a portion of the bipolar burst delivered during *in vivo* H-FIRE of the brain.

All study procedures were conducted following Institutional Animal Care and Use Committee approval. Four, Fischer 344 male rats weighing 200-240 g were anesthetized by intraperitoneal injection of 10 mg/kg xylazine and 60 mg/kg ketamine hydrochloride, and a surgical plane of anesthesia was assessed by loss of the tail pinch reflex. To monitor muscle contractions, a 3-axis accelerometer breakout board (ADXL335, Adafruit Industries, New York, NY, USA) with a sensing range of ± 3 g's was sutured to the dorsum of each rat in the interscapular region at the cervicothoracic junction using 5-0 monocryl suture. Low-pass filter capacitors (0.1 µF) were included at the x, y, and z outputs of the accelerometer for noise reduction. The hair of the skull was clipped and aseptically prepared using povidone-iodine and alcohol solutions. Anesthetized rats were placed in a small animal stereotactic head frame (Model 1350M, David Kopf Instruments, Tungisten, CA, USA). A routine lateral rostrotentorial

surgical approach to the skull was made, and 6 mm by 3 mm rectangular parieto-occipital craniectomy defects were created in the right and left aspects of the skull of each rat using a high-speed electric drill. Custom electrodes were inserted into the center of the forelimb area of the sensorimotor cortex of each rat (coordinates relative to Bregma: 1 mm anterior, 2.5 mm lateral, 2 mm dorsoventral) and advanced to a depth of 2 mm beneath the surface of the exposed dura. The electrodes were fashioned by blunting stainless steel acupuncture needles (0.45 mm diameter, Kingli Medical Appliance Co., Wuxi, China) with high grade sandpaper. Exposure length was set to 1 mm by insulating the electrodes with miniature polyimide tubing (25 AWG, Small Parts, Seattle, WA, USA), and the edge-to-edge electrode spacing was set to 1 mm by molding the electrodes in liquid phase polydimethylsiloxane (PDMS) cured in a 10:1 ratio with Sylgard 184 (Dow Corning Corp., Midland, MI, USA) at 150°C for 30 min.

Pulse parameters were chosen based on the results from the analytical and numerical models to ensure the greatest potential for non-thermal tissue ablation. Following electrode insertion, pulses were applied to the right and left cerebral hemispheres, resulting in two treatments per rat (Table 5.3). All H-FIRE experiments were performed using 180 bursts with a pulse on-time of 200 μs within each burst, and all bursts were delivered at a rate of one per second. In Rat #1 and Rat #2, H-FIRE was applied at voltages of 100 V and 200 V, respectively, to the right hemisphere with a frequency of 250 kHz (duration of single polarity equal to two microseconds). The left hemisphere of Rat #1 and Rat #2 were treated with 180 IRE pulses (200 μs duration) of equivalent energy. In Rat #3, H-FIRE was applied to the left and right hemispheres at voltages of 300 V and 400 V, respectively, with a frequency of 250 kHz. In Rat #4, H-FIRE was applied at a voltage of 400 V to the right hemisphere with a frequency of 500 kHz (duration of single polarity equal to one microsecond). The left hemisphere of Rat #4 was

treated with 90 IRE pulses (200 μs) and an applied voltage of 50V. This lower energy scenario was designed to compare H-FIRE treatment outcomes to traditional IRE protocols in the brain (Ellis et al., 2011).

Table 5.3. Treatment matrix for *in vivo* experiments

Rat Number	Treatment	Hemisphere	Frequency (kHz)	Voltage (V)
1	IRE	Left	-	100
	H-FIRE	Right	250	100
2	IRE	Left	-	200
	H-FIRE	Right	250	200
3	H-FIRE	Left	250	300
	H-FIRE	Right	250	400
4	IRE	Left	-	50
	H-FIRE	Right	500	400

Immediately following treatment, Rats #3 and #4 were subjected to MRI examinations of the brain while under general anesthesia. The MRI was performed with a 0.2 T MRI scanner using a dual phased array hand/wrist coil for RF signal transmission and reception. Sequence acquisition parameters were as follows: T1-weighted images were acquired using spin echo pulse sequence (TR = 200 ms, TE = 16 ms, FOV = 6 cm, matrix = 256 × 196, slice thickness = 2 mm), and T2-weighted images were acquired using a gradient echo pulse sequence (TR = 3000 ms, TE = 90 ms, FOV = 6 cm, matrix = 256 × 196, slice thickness = 3 mm). T1-weigthed images were obtained following intraperitoneal injection of 0.1 mmol/kg of gadopentetate dimeglumine (Magnevist, Berlex Laboratories, NJ, USA). In all rats, humane euthanasia was performed by cervical dislocation approximately 1 hr post-treatment, and the brain was removed and fixed intact in 10% neutral buffered formalin. Following fixation for 48 hours, an adult rat brain matrix slicer (Zivic Instruments, Pittsburg, PA) was used to obtain contiguous 2 mm coronal brain sections from each animal. Brain and sections were embedded routinely in paraffin, sectioned at 5 μm, and stained with hematoxylin and eosin (H&E).

5.3 – Results

5.3.1 – Analytical Modeling of TMP

The critical TMP (Φ_{cr}) across the plasma membrane required to induce IRE is approximately 1 V (Weaver et al., 1996). This threshold is illustrated in Figure 5.1 by the dashed, horizontal line on the TMP profiles. All results are presented at the cell pole ($\theta = 0$) to show the maximum TMP around the cell. Further, results are only shown for TMP across the plasma membrane, as the TMP across the nuclear envelope never approached the permeabilizing threshold. For an electric field of 1500 V/cm, results indicate that a unipolar pulse (Figure 5.1 a), a 250 kHz bipolar burst (Figure 5.1 b), and 250 kHz bipolar burst that includes delays between the pulses (Figure 5.1 c) are all capable of inducing IRE. However, the time above the threshold TMP varies between the different cases. This is investigated further in Figure 5.3 for center frequencies of 0, 100, 250, 500, and 1000 kHz, with the 0 kHz case representing the unipolar pulse, and electric fields of 1000 V/cm and 1500 V/cm. The burst width of the bipolar waveform that included delays was twice as long (40 μs) as the corresponding burst with no delays in order to generate an equivalent pulse on-time (20 μs). The amount of time that the TMP was above the critical value was normalized by the on-time and converted to a percentage. Figure 5.3 illustrates that, for a given frequency, as the electric field is increased from 1000 V/cm to 1500 V/cm, the percentage of the burst above the critical TMP also increases. At 250 kHz, IRE is possible during all waveforms, but at 500 kHz, only the waveforms with amplitudes of 1500 V/cm are capable of inducing IRE. As the frequency of the burst increases, the percentage of the burst above the critical TMP decreases. However, with the inclusion of delays between the pulses, this characteristic dispersion is shifted towards higher frequencies. At 1 MHz, only the 1500 V/cm waveform with delays can theoretically cause IRE.

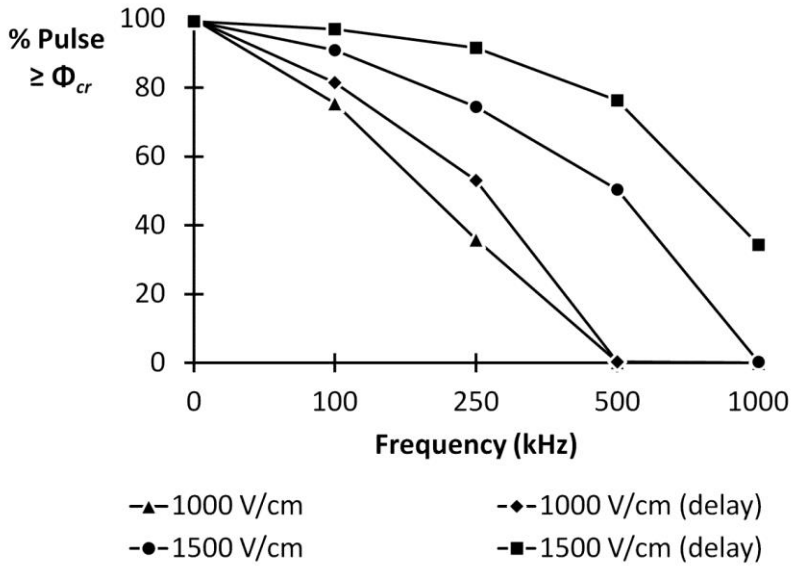

Figure 5.3. Comparison of time above the critical threshold (Φcr) for IRE at various center frequencies. Bipolar bursts were simulated with an electric field of 1000 V/cm and 1500 V/cm and an on-time of 20 µs. As the frequency of the applied field is increased, the time above the critical threshold diminishes. This characteristic dispersion is shifted towards higher frequencies for bursts that have a delay between the positive and negative polarity pulses. A conventional IRE pulse is depicted by the 0 kHz data point.

5.3.2 – Numerical Modeling of Temperature and Thermal Damage

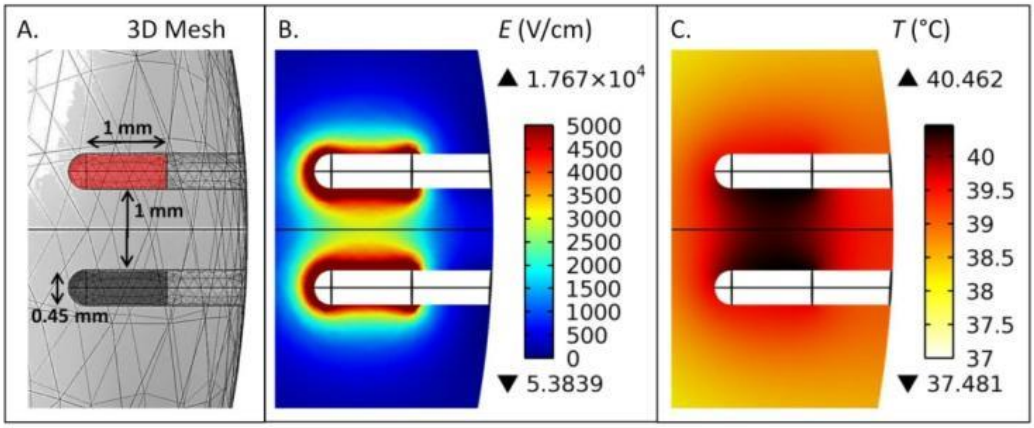

Figure 5.4. Schematic diagram of the FEM alongside the predicted electric field (E) and temperature (T) distributions in brain tissue. The 3D mesh (a) consisted of 23989 elements. An energized electrode (red) and ground electrode (black) with a 0.45 mm diameter were spaced 1 mm apart (edge-to-edge) and had an exposure length of 1 mm (not including the blunt tip). (b) The resulting electric field distribution in the x-z plane for an applied voltage of 400 V along the energized electrode. (c) The resulting temperature distribution in the x-z plane following the simulation of 180, 200 µs pulses. Upper and lower triangles in the legends depict maximums and minimums within the entire subdomain, respectively.

Results from the simulated H-FIRE treatment of brain tissue are shown in Figure 5.4. The FEM was developed in 3D, as visualized by the mesh (Figure 5.4 a), and 2D slices were taken in the x-z plane through the center of the brain geometry to display the electric field (Figure 5.4 b) and temperature (Figure 5.4 c) distributions. The electric field decays rapidly with increasing distance from the electrodes, due to their relatively small diameter. The applied voltage-to-distance ratio of 4000 V/cm resulted in a peak electric field of 2979 V/cm along the centerline between the electrodes. Because the electric field relates directly to temperature through the Joule heating term, the application of 180, 200 μs long bursts causes only a 3.5°C increase in temperature near the electrode boundaries. This resulted in a maximum damage integral value of 0.003 at the electrode/tissue interface, which corresponds to a 0.3% probability of cell death from thermal processes. Therefore, all cell death *in vivo* is likely to be a direct result of IRE and not thermal modes.

5.3.3 – In Vivo Experiments

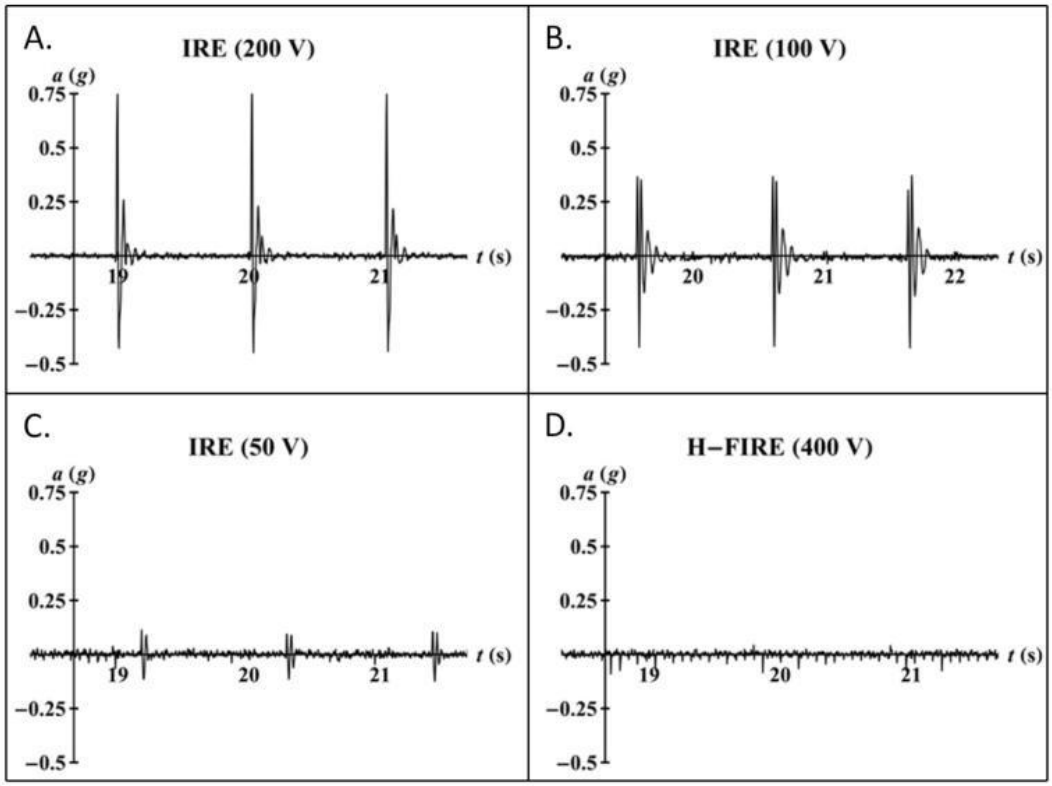

Figure 5.5. Snapshot of acceleration (a) versus time during IRE and H-FIRE treatments. Acceleration at the cervicothoracic junction was detected by the accelerometer based recording system during all IRE protocols. None of the H-FIRE protocols resulted in detectable acceleration of the cervicothoracic junction (e.g. shown, 400 V/250 kHz).

All IRE pulsing protocols were associated with macroscopic muscular contractions of the cervicothoracic junction, which were also palpable to the neurosurgeon, while no visual or tactile evidence of muscular contraction was seen during any of the H-FIRE bursts (Additional File 1). These results were quantitatively confirmed by the data recordings from the accelerometer (Figure 5.5). Peak acceleration was determined during the first 90 bursts of the highest energy H-FIRE protocol (400 V/250 kHz) and the first 90 pulses of each IRE protocol (50 V, 100 V, 200 V). A one-way ANOVA was used to investigate the effects of each protocol on the ranks of peak acceleration at the cervicothoracic junction. In the event of a significant main effect, pairwise comparisons were completed using Tukey's Honestly Significant Difference (HSD). All statistical analyses were conducted using JMP 7 (Cary, North Carolina, USA) with a significance

level of $p \leq 0.05$. Results indicate that, even in the highest energy H-FIRE protocol, there are no detectable peaks in acceleration above the inherent noise of the system. However, in all IRE protocols, peaks in acceleration associated with each pulse are detectable above the baseline noise. Further, pairwise comparisons between the various IRE protocols indicated that the mean peak acceleration during each treatment was energy dependent. Specifically, the mean peak acceleration decreased as the applied voltage decreased (Figure 5.6).

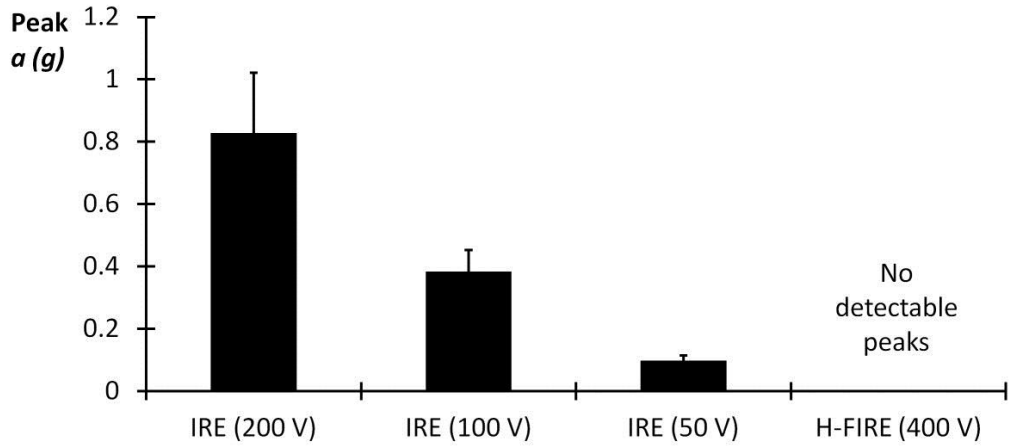

Figure 5.6. Peak acceleration (a) during IRE protocols averaged over the first 90 pulses. Mean peak acceleration during IRE treatments at the cervicothoracic junction for each applied voltage was significantly different from each other. H-FIRE resulted in no detectable acceleration of the cervicothoracic junction.

All treatments evaluated in this study produced ablative lesions in brain tissue, as evaluated with MRI examinations (Figure 5.7) and pathologic preparations (Figure 5.8). In Rats #3 and #4, the MRI characteristics of both H-FIRE and IRE lesions were similar. Lesions appeared as focal, ovoid to elliptical, T1 iso- to hypo-intense, uniformly and markedly contrast enhanced (Figure 5.7 a, b, c, d, and f), and T2 hyper-intense (Figure 5.7 e). All lesions were well demarcated from adjacent, normal brain tissue and appeared similar in size. A comparable size IRE lesion was produced at lower energy, as compared to the H-FIRE lesions. However, as mentioned, IRE even at the lowest energy scenario produced muscle contractions, while the highest energy H-FIRE protocol did not (Figure 5.6).

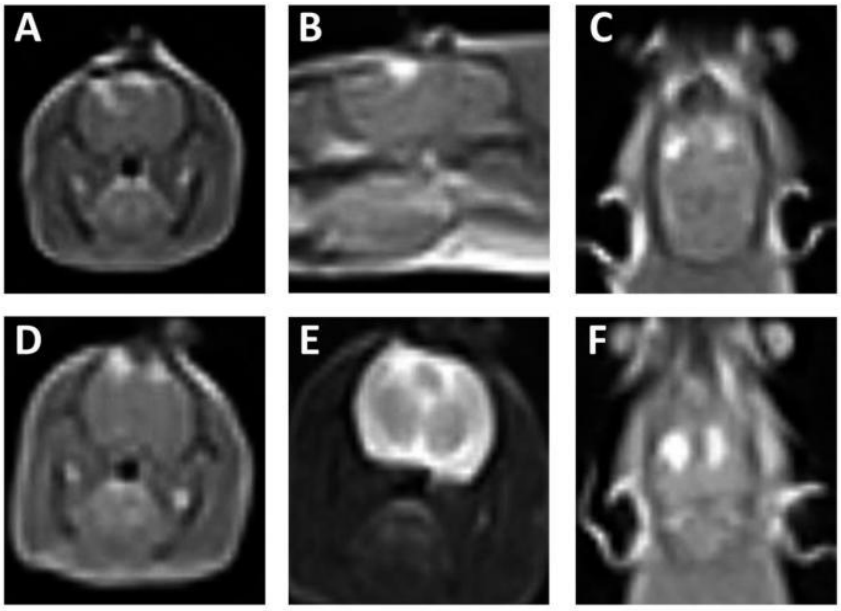

Figure 5.7. MRI appearance of H-FIRE and IRE lesions in rat brain. In all panels, IRE and H-FIRE induced lesions appear as focal hyper-intense regions (white) compared to adjacent untreated cerebrocortical tissue (gray). Top (a-c) obtained from Rat #3, in which both the left and right cerebral hemispheres were treated with H-FIRE at 300 V/250 kHz and 400 V/250 kHz, respectively. Bottom (d-f), Rat #4, which underwent H-FIRE in the right cerebrum at 400 V/500 kHz, and IRE at 50 V in the left cerebrum. (a and d) Post-gadolinium T1-weighted MRI sequences in the axial plane. (b) Post-gadolinium T1-weighted MRI sequences in the right parasagittal plane. (c and f) Post-gadolinium T1-weighted MRI sequences in the dorsal plane. (d) T2-weighted MRI sequence in the transverse plane. In all panels, the right side of the brain is on the left side of the panel.

Compared to untreated brain (Figure 5.8 a and b), histopathologic examination of brain sections from all treatments demonstrated clear areas of ablation indicated by pallor of the treated tissue that was sharply delineated from adjacent normal brain (Figure 5.8 c, Figure 5.9). H-FIRE and IRE lesions were predominantly characterized by areas of complete obliteration of cerebrocortical architecture by an eosinophilic, vacuolated amorphous debris (Figure 5.8 c and d). In Rat #1, the H-FIRE ablation zone was confined to regions of elevated electric field surrounding the electrodes, whereas all other pulsing protocols resulted in ablation zones spanning the entire region between the electrodes. Cavitary cerebrocortical defects were induced with H-FIRE in Rat #1 and IRE in Rat #4. Variably sized regions of intraparenchymal hemorrhage were most pronounced immediately adjacent to and within electrode insertion tracks

(Figure 5.9 b and e). The morphology of remnant neuronal and glial elements within H-FIRE ablated regions demonstrated features of both apoptosis and necrosis, including shrunken and hypereosinophilic cytoplasm, nuclear chromatin condensation, and nuclear pyknosis and karyolysis (Figure 5.8 d). Free glial and neuronal nuclei in various states of degeneration were scattered throughout ablation zones. Inflammation was not a significant feature of IRE or H-FIRE lesions at the time point brains were examined.

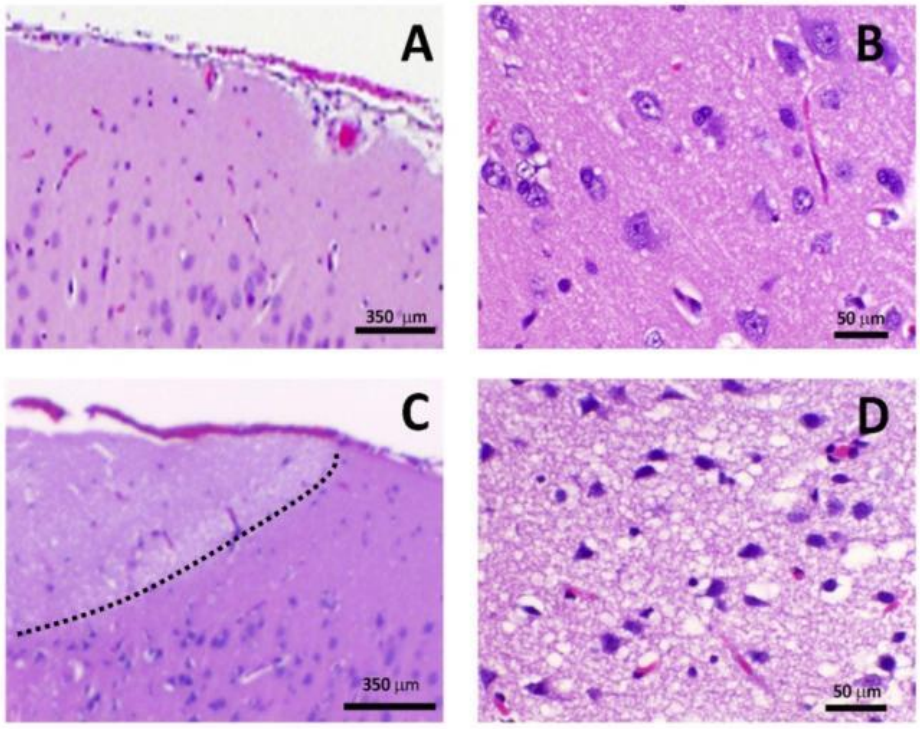

Figure 5.8. Histopathology of rat brain tissue. Untreated (a and b) and H-FIRE treated at 200 V/250 kHz (c and d, Rat #2, right hemisphere). Hematoxylin and eosin stain. The delineation between treated and untreated tissue (c, dotted line).

5.4 – Discussion

The results presented above demonstrate the feasibility of H-FIRE for non-thermally ablating tissue without causing any associated muscle contractions. Specifically, we have shown the ablation of brain tissue by applying bipolar bursts at center frequencies up to 500 kHz. While the pilot data gathered here was not designed to locate an upper limit in terms of frequency at

which IRE could still be achieved *in vivo*, the theoretical model of TMP suggests that IRE should be possible up to 1 MHz for an electric field of 1500 V/cm. Interestingly, including a delay between the positive and negative pulses comprising the bipolar burst offers a therapeutic advantage in addition to protecting the MOSFETs in the pulse generation system from ringing. By not forcing a discharge of the TMP with an immediate reversal of polarity, the cell is allowed to return to the resting TMP according to its characteristic time constant. As a result, the TMP is maintained above the critical voltage required for IRE for a longer amount of time. This metric has been recognized before as a potential indicator of treatment outcomes in electroporation-based therapies with bipolar waveforms (T. Kotnik et al., 2003).

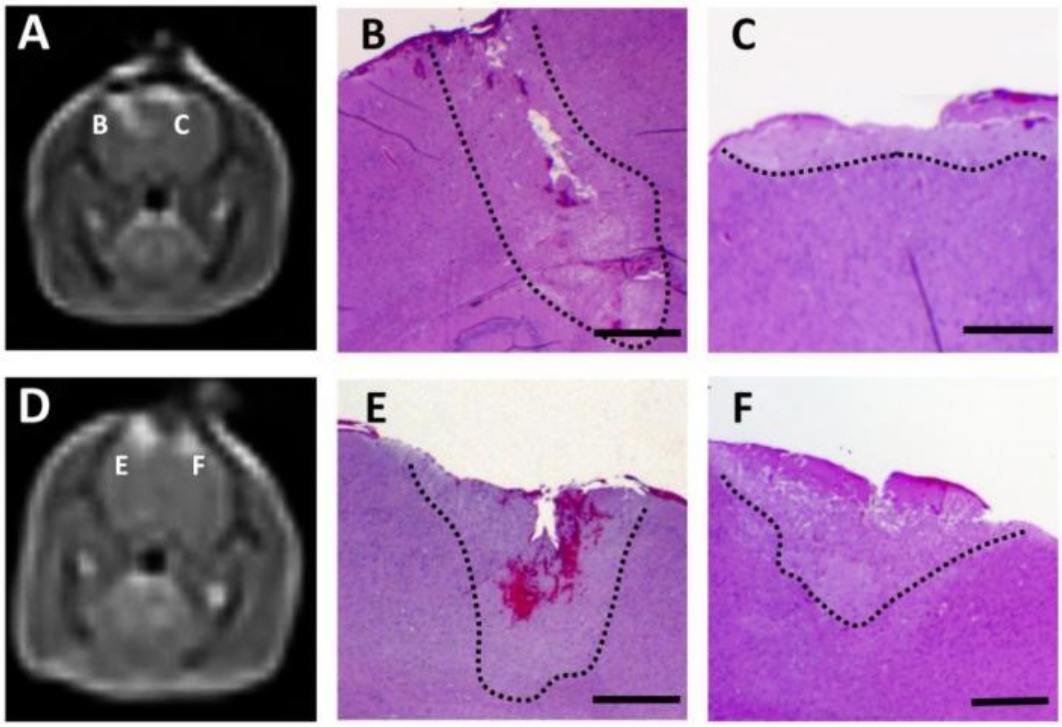

Figure 5.9. MRI and corresponding neuropathology of rat brain tissue lesioned with H-FIRE and IRE. Top (a-c) obtained from Rat #3, in which both the right (b) and left (c) cerebral hemispheres were treated with H-FIRE at 400 V/250 kHz and 300 V/250 kHz, respectively. Bottom (d-f), Rat #4, which underwent H-FIRE in the right cerebrum at 400 V/500 kHz (e), and IRE in the left cerebrum at 50 V (f). (a and d) The same as those presented in Figure 5.7 (a and d). The right side of the brain is on the left side of the panel. (b, c, e, and f) Hematoxylin and eosin stain (scale bar = 1 mm). The delineation between treated and untreated tissue is shown (black, dotted line).

Due to the small number of observations chosen to assess feasibility, quantitative comparisons between pulse parameters and ablation volumes were not performed. Qualitatively, the fact that IRE was performed with a lower applied voltage in Rat #4 suggests that H-FIRE requires a greater electric field strength than conventional IRE for inducing necrosis, as observed under MRI (Figures 5.7 and 5.9). However, even at higher fields, H-FIRE produced no muscle contractions either tactilely, visibly, or through accelerometer recordings at the cervicothoracic junction (Figures 5.5 and 5.6). In Rat #1, histopathologic examination revealed that ablation due to H-FIRE occurred only in regions of elevated electric field surrounding the electrodes. This may be explained due to the rapid decline in electric field away from the electrodes predicted by the FEM, and the relatively low percentage of the burst above the critical TMP for the 1000 V/cm waveforms predicted by the analytical model.

The gross histological lesions from the *in vivo* H-FIRE treatments, along with the results of the FEM for predicting the temperature increase in brain tissue during H-FIRE, support the claim that the ablation is not thermally mediated and a direct result of IRE. There is complete uniformity of tissue destruction within targeted H-FIRE areas (Figures 5.8 and 5.9), which is in contrast to thermal ablation procedures, such as radiofrequency (RF) ablation (Merkle et al., 2001). Additionally, H-FIRE results in a sharp transition zone between lesioned and normal brain (on the order of 10-20 μm), which is in agreement with previous intracranial studies on traditional non-thermal IRE (Ellis et al., 2011; Garcia et al., 2010). The transition zone in RF ablation is characterized by regions of partial tissue damage of anywhere from 100 μm to a few millimeters (Morris et al., 2004).

Due to the greater electric field strength required to induce IRE with high-frequency, bipolar bursts, evaluating the thermal damage probability in the tissue gains importance in H-

FIRE treatment planning. Here, the FEM was conservative in the sense that all boundaries were thermally insulating, no electrodes were present in the subdomain to dissipate heat, and the duty cycle approach was implemented for calculating Joule heating as opposed to simulating individual pulses. The *in vivo* treatments resulted in no predictable thermal damage, due to the small diameter of the electrodes and small exposure length. In the future, temperature predictions should be validated by direct measurements, and the effects of H-FIRE on the electrical conductivity of the tissue should be incorporated into the FEM, as this will have implications for Joule heating. However, it is possible that H-FIRE will produce more subtle changes in tissue conductivity compared to IRE, due to its ability to enhance the capacitive coupling across epithelial layers (Arena, Sano, Rylander, et al., 2011).

The brain was chosen here as a model system due to our expertise and specific interest in advancing electroporation-based therapies for the treatment of malignant glioma, including glioblastoma multiforme (Garcia, Pancotto, et al., 2011). Despite attempts to selectively target efferent pathways to the limbs based on electrode placement, all IRE treatment protocols produced contractions of the head, truncal, and limb musculature. Therefore, movement may be caused by direct stimulation of motor regions in the brain, as well as leak currents that directly excite muscle. No hemorrhage occurred, other than an anticipated microhemorrhage along the electrode tracks, and no inadvertent penetration into cerebrospinal fluid pathways occurred, other than traversing of the subarachnoid space at the point of electrode insertion, which might influence leak currents. It is expected that the results obtained in the brain will translate to other tissues, such as the liver, prostate, kidney, and breast, which warrant further investigations. Additionally, studies performed directly in muscle would help elucidate the mechanism

responsible for a reduction in nerve stimulation in response to H-FIRE, as the presence of the skull may provide a certain degree of electrical isolation from nearby muscle.

According to classic literature, bipolar waveforms have a higher current threshold for action potential stimulation as compared to monopolar waveforms, which becomes more evident as pulse duration is reduced (Reilly et al., 1985), and bipolar waveforms reduce muscle twitch forces as compared to monopolar waveforms (van den Honert et al., 1979). No electrically induced movement was seen in any of the H-FIRE treatment protocols, ruling out the possibility of tonic contraction. Elimination of patient motion through the delivery of high-frequency, bipolar bursts confers several significant advantages over IRE to both the neurosurgeon and neurosurgical patient that warrants higher energy demands required to achieve ablation. Although electroporation-based therapies have proven to be safe and effective in the brain (Ellis et al., 2011; Garcia, Pancotto, et al., 2011; Gehl et al., 2011), they require the use of paralytic agents. H-FIRE obviates the need for paralytic agents and, in doing so, provides the possibility for performance of minimally invasive, outpatient intracranial surgery, conscious neurosurgical interventions, procedures in proximity to eloquent areas of the brain, and eliminates the inherent risk associated with general anesthesia. Finally, although not directly evaluated in this study, previous investigators have demonstrated that bipolar pulse delivery at 1 kHz is associated with less patient pain (Daskalov et al., 1999).

For frequencies well into the megahertz range, or individual pulse durations on the order of 10-100 nanoseconds, it is possible for a significant amount of current to bypass the plasma membrane through capacitive coupling. As a result, electroporation of both the plasma membrane and intracellular structures can occur for electric field strengths on the order of 10-100 kV/cm (Beebe et al., 2003; Pakhomov et al., 2007). These nsPEFs have shown great promise

as a cancer therapy due to their ability to induce cell death through apoptotic mechanisms and reduce muscle contractions (Long et al., 2011). One challenge associated with nsPEFs that further distinguishes them from IRE is that the field strength required to induce electroporation of intracellular vesicles and organelles, such as the nucleus, is an order of magnitude greater (40 kV/cm) (Nuccitelli et al., 2006). This is predominantly due to the small size of vesicles and organelles compared to the overall cell. In H-FIRE, by targeting the plasma membrane, which encompasses the entire cell, the field required to induce cell death is closer in amplitude to IRE protocols than nsPEFs protocols. From an electrical engineering perspective, this simplifies the pulse generation system, and allows for the utilization of silicon based components and commercially available high voltage switches.

5.5 – Conclusion

This proof-of-concept study was performed to theoretically and experimentally investigate the potential of high-frequency, bipolar bursts to ablate tissue through IRE and eliminate the associated muscle contractions seen in traditional IRE treatments performed with unipolar pulses. In a rat model, H-FIRE performed with frequencies up to 500 kHz and voltage-to-distance ratios up to 4000 V/cm produced lesions in brain tissue characteristic of IRE outcomes without causing muscle contractions. Therefore, H-FIRE has the potential to be performed clinically without the administration of paralytic agents, which are used in IRE protocols to mitigate muscle contractions. While not explored explicitly in this study, H-FIRE also offers the benefits associated with charge balancing, including reduced electrolytic contamination. Additionally, high-frequency fields have the potential to overcome impedance barriers posed by low conductivity tissues, which could result in more homogenous and predictable treatment outcomes in heterogeneous systems. Future work should be directed

towards further elucidating the relationship between different H-FIRE pulse parameters and ablation volumes, in order to successfully translate this technology for the treatment of tumors. Electroporation-based therapies are gaining momentum as viable treatment options for cancer. H-FIRE has the potential to follow suit due to the added benefits that high-frequency, bipolar bursts provide.

6 – Treatment of Implanted Tumors in Mice with H-FIRE

6.1 – Introduction

This study aims to prove that, like IRE, H-FIRE is a viable treatment option for solid tumor ablation. Several IRE experiments on preclinical mouse models have been performed. These include investigations on a subcutaneous model of fibrosarcoma (92% complete regression rate) (B. Al-Sakere et al., 2007), an orthotopic model of breast adenocarcinoma (71% complete regression rate) (Neal et al., 2010), and an orthotopic model of pancreatic adenocarcinoma (25% complete regression rate) (Jose et al., 2012). Here, a subcutaneous mouse model of Glioblastoma is utilized. Results indicate evidence of profound necrosis, reduction in tumor volume, and a 38% complete regression rate.

6.2 – Methods

This study was approved by the Virginia Tech Institutional Animal Care and Use Committee (IACUC, protocol number 12-108-SBES). 6-7 week old Hsd:Athymic Nude-Foxn1^{nu} male mice (Harlan, Dublin, VA, USA) were inoculated subcutaneously in the dorsolateral flank region with human Glioblastoma cells (DBTRG-05MG) while anesthetized by inhalation of 3% isoflurane (Abbott Laboratories, Abbott Park, IL, USA). Mice were housed in individually ventilated cages in groups of five under specific pathogen free conditions and allowed access to sterilized water and feed *ad libitum*. Prior to inoculation, cells were cultivated using standard techniques in DMEM (High-glucose supplemented with L-glutamine; Thermo Scientific, Logan, UT, USA) containing 10% FBS (Sigma Aldrich, St. Louis, MO, USA) and 1% Penicillin/Streptomycin (Invitrogen, Carlsbad, CA, USA). Upon reaching 80% confluencey, cells were resuspended at a concentration of 5×10^6 cells/ml in an 85/15 mixture of PBS and Matrigel

(High Concentration, BD Biosciences, San Jose, CA, USA). 200 µl aliquots of this final suspension was used for each injection (1×10^6 cells total).

Tumor growth was measured over time using calipers, and volumes were calculated according to the modified ellipsoid formula (Jensen et al., 2008):

$$l\,w^2/_2 \qquad (1)$$

where *l* is the length of the longitudinal diameter and *w* is the width of the transverse diameter. Tumors were treated when the greatest diameter reached approximately 5 mm. Mice were anesthetized following the same isoflurane inhalation protocol, and the skin over the tumor was prepped with 70% isopropyl alcohol. Then, custom steel needle electrodes (0.4 mm Ø) were advanced into the center of the tumor. The electrodes were mounted on calipers (General Tools, New York, NY, USA) to allow for spacing adjustment, however, 0.4 cm spacing (center-to-center) was used in all treatments. Needles were chosen over the use of plate electrodes to ensure that the electric field in the tumor was above the threshold for cell death, as the pulse generator was limited to 1000 V.

Table 6.1. Treatment matrix for mouse tumor ablation

Group	Treatment	Burst Width (µs)	Frequency (kHz)/Duration of single polarity (µs)	Mouse #	Voltage (V)
1 (*n*=8)	H-FIRE	100	100/5	13, 15, 17, 18, 19, 21, 23, 24	1000
2 (*n*=4)	Sham	-	-	14, 20, 22, 25	-

H-FIRE treatments were performed using a custom high-frequency bipolar pulse generator (Applied Energetics, Tucson, AZ, USA) capable of delivering up to 100 µs long bursts repeating once every second. As with the pulse generator presented in the previous chapter, an arbitrary function generator (AFG3011, Tektronix, Beaverton, OR, USA) was used to define the parameters of the burst to be delivered. A 2 µs delay was included between the pulses

comprising a burst in order to protect the MOSFETs in the pulse generator from ringing, and the output was terminated into a 500 Ω load in parallel with the electrodes to maintain the appropriate pulse characteristics. The load in parallel reduces the RC time constant of the tissue and provides a pathway to ground for the tissue to discharge within the period between pulses. The specific pulse parameters and treatment groups are outlined in Table 6.1, and an example treatment is illustrated in Figure 6.1 a. In each trial, H-FIRE was performed for 2 min, resulting in a total of 120 bursts being delivered to the tumors.

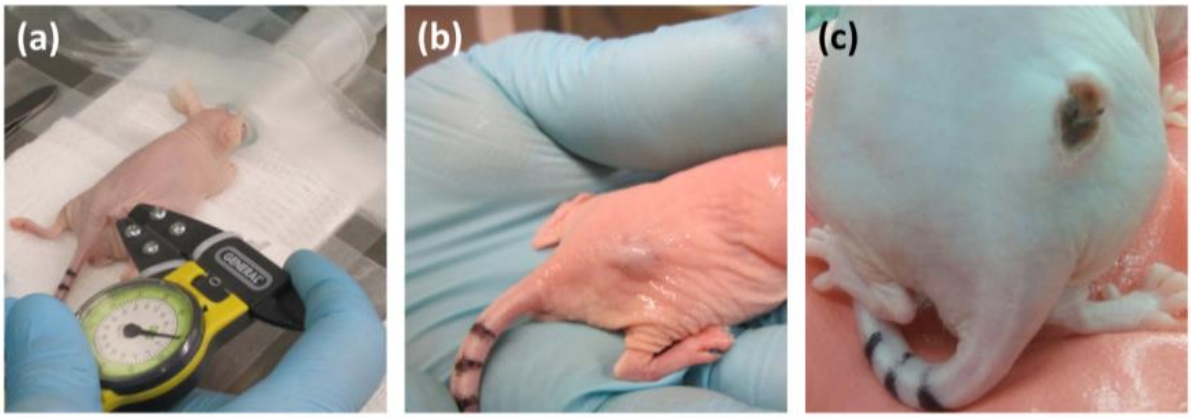

Figure 6.1. Representative H-FIRE tumor treatment. Mouse #23 during H-FIRE treatment (a), immediately post-treatment (b), and 5 days post-treatment (c).

Following treatment, topical antibiotic ointment was applied to the needle insertion wounds. Mice were removed from anesthesia and provided 5 mg/kg Ketoprofen analgesic diluted in 1 ml sterile saline solution for recovery. One mouse from Group 1 was sacrificed 24 hr post-treatment to look for early signs of necrosis and disruption of blood flow. The remaining mice were euthanized 30 days post-treatment or earlier for humane reasons if the tumor volume reached 800 mm^3.

Upon reaching the endpoint for euthanasia, samples of any present tumor tissue were excised and sectioned for processing. Representative tissues were preserved in 10% neutral buffered formalin and embedded in paraffin. Formalin preserved paraffin embedded samples

were sectioned and processed for histology using H&E. All photomicrographs were obtained with a Leica DMI 6000 inverted microscope (Leica Microsystems Inc., Buffalo Grove, IL, USA).

A one-way ANOVA was used to investigate the effects of the two experimental groups on tumor volume 30 days post-treatment. The effect size was calculated as the difference in the means divided by the standard deviation of the control group (Portney et al., 2009). The statistical analysis was performed using JMP Pro 10 (SAS Institute, Inc., Cary, NC) with a significance level $p \leq 0.05$.

6.3 – Results and Discussion

Immediately following treatment, whitening of the tumor occurred, which can be associated with reduced blood flow and the beginning stages of edema (Figure 6.1 b). This characteristic antivascular effect of electroporation-based therapies has been utilized in ECT to treat bleeding metastasis (Jarm et al., 2010). Due to the use of uninsulated electrodes, the skin overlying the tumor was killed in conjunction with the tumor. This resulted in scab formation (Figure 6.1 c) 1 day post-treatment. The presence of a scab along with the occurrence of edema led to an overestimation of tumor volumes during short-term follow-up. Within two weeks after treatment delivery, scabs resolved and there was clear evidence of tumor regression. This can be seen from endpoint images taken immediately prior to and following tissue harvesting (Figure 6.2).

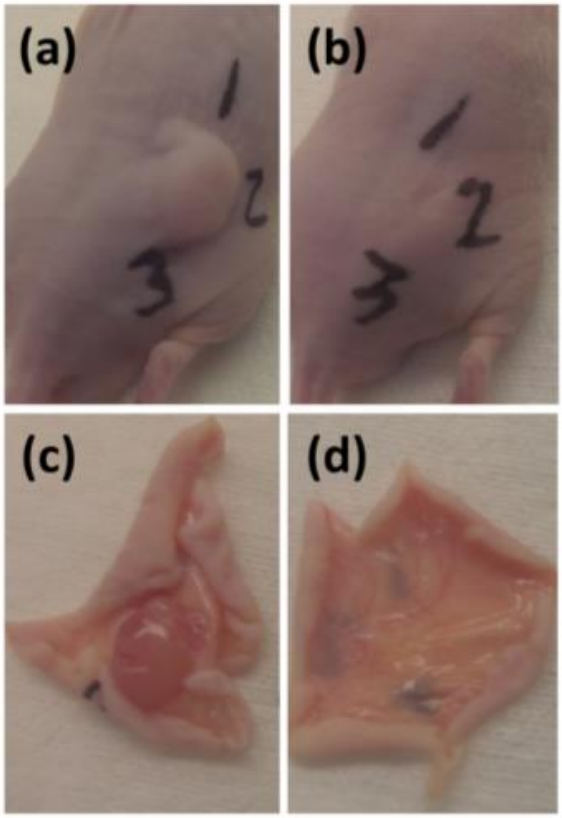

Figure 6.2. Representative endpoint images. Group 2 sham mouse #22 (a and c) and Group 1 H-FIRE treated mouse #23 (b and d). The dimensions of the tumor on mouse #22 are w = 7.9 by l = 10.8 mm. On mouse #23, there is no evidence of tumor. Numbers written on the surface of the skin are for tissue orientation during histological preparation.

Tumor growth curves from all experimental groups are shown in Figure 6.3. From this figure, it is clear that H-FIRE (Figure 6.3 a) delayed the onset of the exponential tumor growth phase, which is seen in the sham mice around day 25 (Figure 6.3 b). Further, no measureable tumors were seen at the 30 day time-point in 3 of 8 mice treated with a 100 kHz burst (38% complete regression rate). The average tumor volume from the mice treated with H-FIRE was 71 mm^3 (+/- 64 mm^3) as compared to 348 mm^3 (+/- 253 mm^3) in the sham group. Additionally, the reduction in tumor volume due to H-FIRE was statistically significant (p = 0.013) and had an effect size of 1.093. This effect size (> 0.8) indicates a large effect of the H-FIRE treatment on tumor volume (Portney et al., 2009).

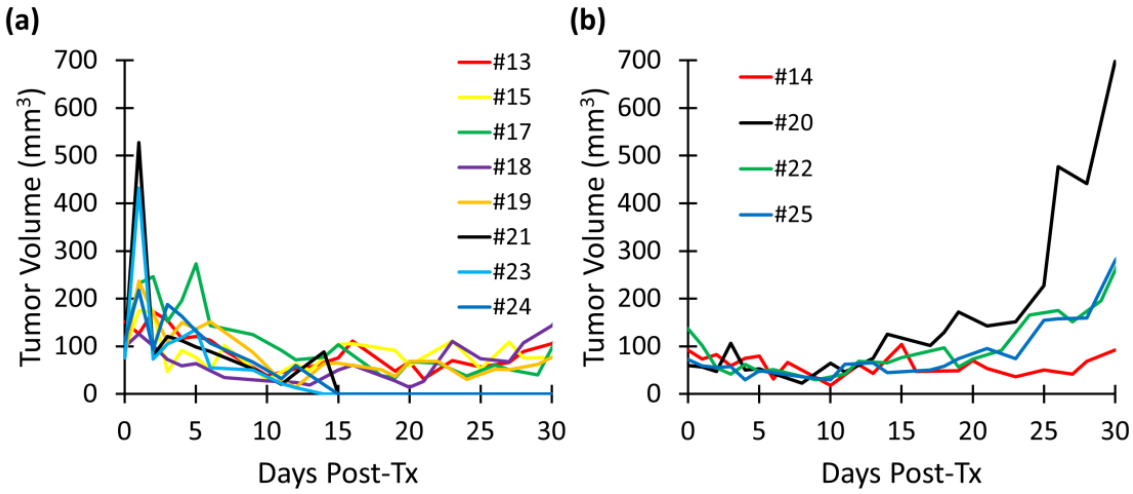

Figure 6.3. Volume curves for tumors. (a) Group 1 mice treated with H-FIRE at 100 kHz (5 µs duration of single polarity). (b) Group 2 sham mice.

The analytical solution to the Laplace equation ($\nabla^2\phi = 0$) for the H-FIRE protocol is shown in Figure 6.4. The procedure for calculating the electric field distribution is described in detail in Chapter 7. An applied voltage of 1000 V is sufficient to cover the entire length (*x*-direction) of the representative tumor with an electric field of 900 V/cm or greater. However, there exists a narrow region along the width (*y*-direction) of the tumor that may experience a sub-lethal electric field. The 900 V/cm threshold is based on experiments conducted *in vitro* on 3D tissue engineered constructs (see Chapter 8), but explains relatively well the regression profiles seen here *in vivo*. At the time of treatment, the tumors were slightly oblong, with an average across all trials of l = 7.1 mm (+/- 1.1 mm) and w = 5.2 mm (+/- 0.7 mm). Therefore, the lack of complete regression in 5 of 8 mice is likely due to suboptimal treatment planning and could be corrected in future work by performing a second H-FIRE session with the electrodes aligned along the tumor width.

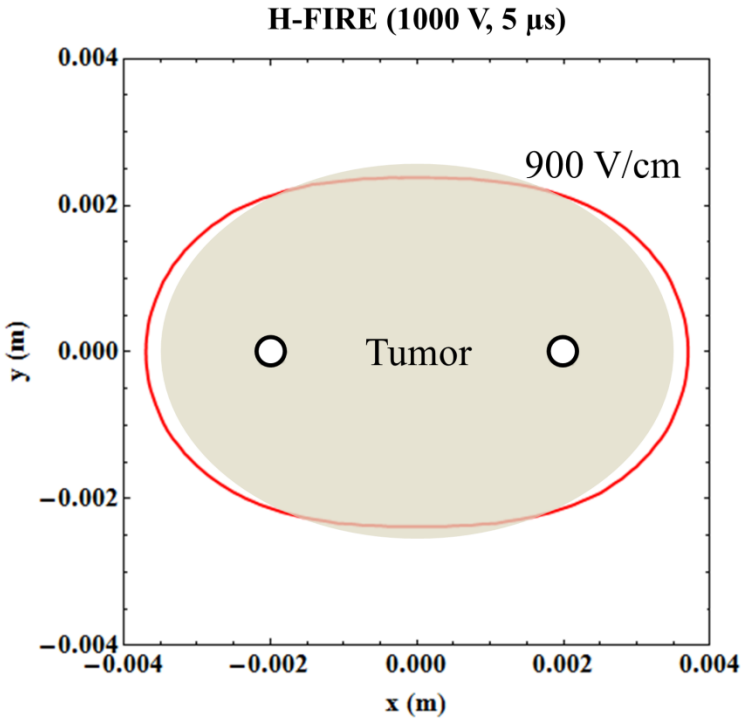

Figure 6.4. Illustration of the electric field threshold for cell death in relation to tumor dimensions. The tumor is drawn according to average length (x-direction) and width (y-direction) measurements at the time of treatment. The electrodes (black contours) are inserted directly into the tumor, and the resulting 900 V/cm electric field threshold for cell death is superimposed (red contour).

Histological examination of the targeted tissue 24 hrs after H-FIRE treatment is shown in Figure 6.5. The left panel (Figure 6.5 a) is taken superficially and shows acute damage to the skin, as well as the underlying tumor. The nuceli appear pycnotic (shrunken) and all within the same cytoplasm, indicating complete destruction of the tumor through predominantly necrotic mechanisms. Additionally, there is severe vascular congestion, hemorrhage into the surrounding tissue, and contraction of collagen fibers. The degree of collagen fiber contraction and hemorrhage is reduced in deeper portions of the tissue (Figure 6.5 b). There is also evidence of glioblastoma cells embedded into the subcutaneous fat.

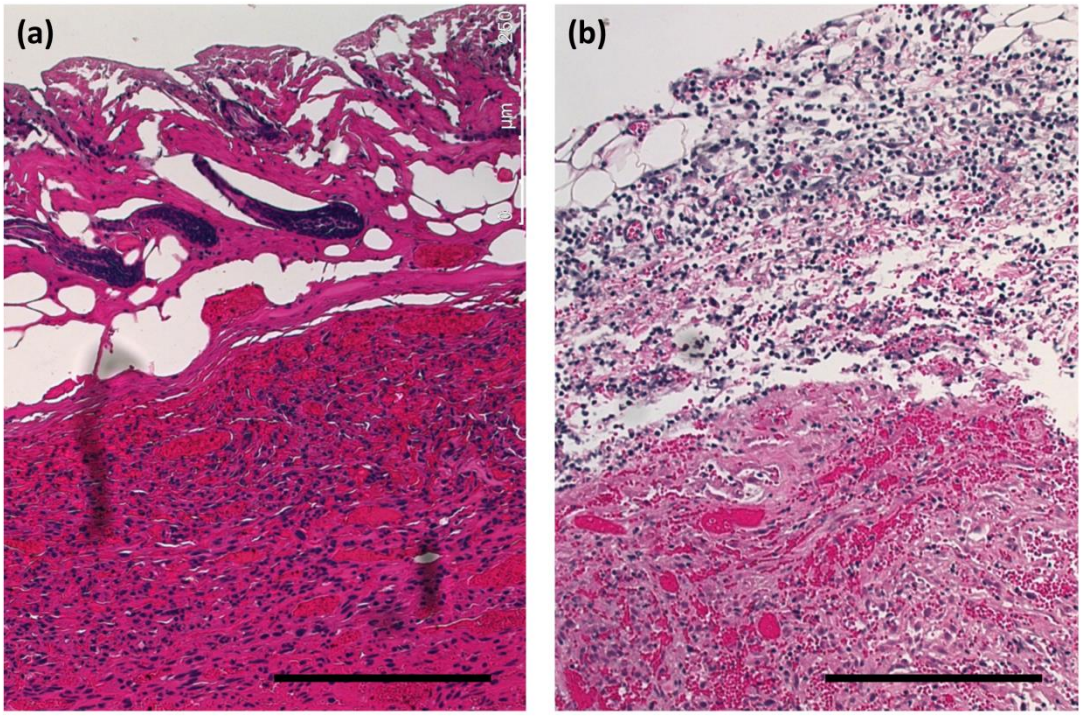

Figure 6.5. H&E stain of tumors 24 hrs post-treatment. (a) Mouse # 11 superficial skin (top of image) and underlying tumor (bottom of image). (b) Mouse # 11 subcutaneous fat (top of image) and tumor (bottom of image). Scale bars represent 250 µm.

Figure 6.6 shows histological sections from the study endpoint of an H-FIRE treated mouse (Figure 6.6 a) and a sham mouse (Figure 6.6 b). Despite the fact that no measurable tumor was observed in the H-FIRE treated mouse (# 23), pockets of viable glioblastoma cells are present surrounding blood vessels located above the musculature. Similar features are seen in the sham mouse (# 20), within the addition of a viable tumor mass beneath the muscle layer. Cells comprising the viable tumor display a large nucleus surrounded by a well-marked cytoplasm and well-defined cell membrane. Additionally, there is evidence of healthy vasculature along the margin of the tumor at the interface between the muscle and fat layer.

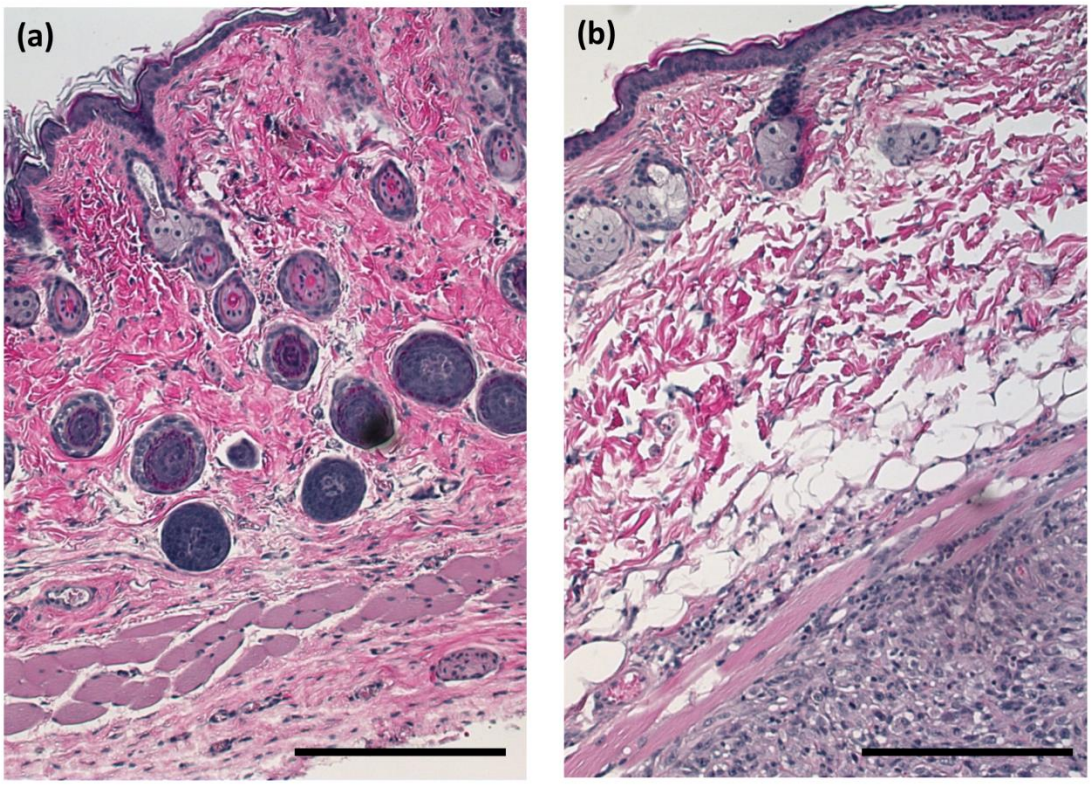

Figure 6.6. H&E stain of tumors at the study endpoint. (a) H-FIRE treated mouse # 23 superficial skin (top of image) and underlying musculature (bottom of image). (b) Sham mouse # 20 superficial skin (top of image) and underlying tumor (bottom of image). Scale bars represent 250 µm.

6.4 – Limitations and Conclusion

The use a mouse model is not ideal for evaluating the potential of H-FIRE to simultaneously cause ablation without any associated muscle contractions. Due to their low weight (< 35 g), mice present a fraction of the inertia as larger animals and are unable to resist changes in motion. Additionally, the subcutaneous tumors are large in comparison to the size of the mice. As a result, the electric field extends far beyond the tumor margin and covers a majority of the musculature, giving rise to localized movement. Another limitation of the current study was that IACUC approval allowed for only a 30 day post-treatment monitoring period. Due to the fact that onset of the exponential growth phase was later than expected, no mice had to be sacrificed due to restrictions on tumor volume. Therefore, we were not able to derive

Kaplan-Meier plots or draw any conclusions on the ability of H-FIRE to improve disease-free survival.

Despite these limitations, this study provides strong evidence that H-FIRE can be used for tumor ablation. All mice treated with H-FIRE tolerated the therapy well and experienced a significant reduction in tumor volume when compared to untreated controls. However, future work is needed to investigate the presence of pockets of neoplastic cells around blood vessels following regression of the visible tumor mass. It is possible that these features were the result of suboptimal treatment planning and could be eliminated by increasing the electric field strength or the number of bursts. Alternatively, a frequency of 100 kHz (5 μs duration of single polarity) may have been too low to electrically short through the lining of blood vessels, which could provide protection, and higher frequencies should be investigated in future work.

7 – Optimization of Pulse Parameters for Eliminating Muscle Contractions during H-FIRE

7.1 – Introduction

As mentioned, a challenge with electroporation-based therapies is that the delivery of unipolar electric pulses characteristic of electroporation causes muscle contractions. To reduce movement, muscle relaxants may be administered to patients prior to treatment (Ball et al., 2010; Billard et al., 2004; Landstrom et al., 2010; Rubinsky et al., 2007). This poses additional concerns for the anesthesiologist, as the dosage of muscle relaxants must be continually monitored to ensure an adequate neuromuscular blockade and proper respiratory function (Eikermann et al., 2003). Electrically induced movement, while not ideal, has not prevented IRE, ECT, EGT, and nsPEFs from being established as safe and effective treatment options for cancer (Daud et al., 2008; Ferraro et al., 2011; Garon et al., 2007; Marty et al., 2006; Mir, Belehradek, et al., 1991; Thomson et al., 2011) and other non-cancerous pathologies (Maor et al., 2009). However, there has been a growing emphasis in the literature on developing novel techniques for performing electroporation that reduce the intensity or extent of muscle contractions (Arena, Sano, Rossmeisl, et al., 2011; Daskalov et al., 1999; Golberg et al., 2012; Long et al., 2011).

According to classic literature on electrical stimulation, a bipolar pulse has a higher current threshold for action potential excitation as compared to a unipolar pulse of equivalent phase duration (Reilly et al., 1985). This effect is enhanced as pulse duration is reduced. When a microsecond order pulse is applied, there is a latency period between the offset of the pulse and the rising phase of the action potential. A rapid reversal of polarity falling within this latency period can accelerate passive repolarization and inhibit action potential generation (van den Honert et al., 1979). An example of this phenomenon is shown in Figure 7.1

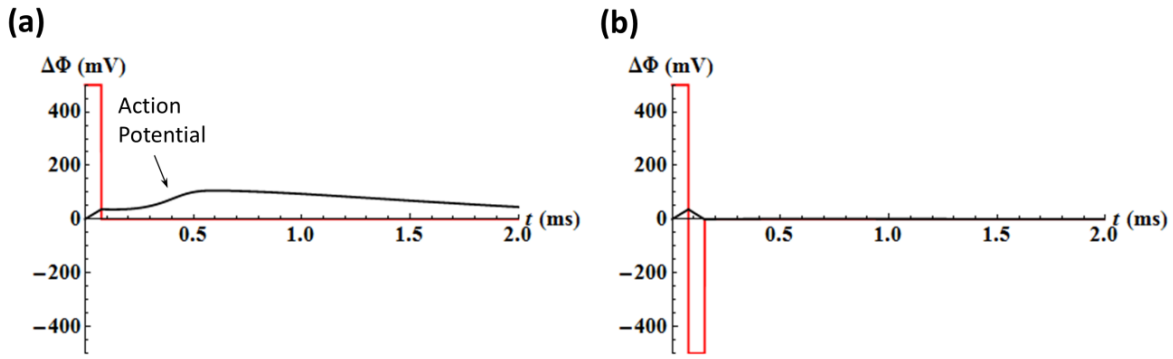

Figure 7.1. Illustration of action potential inhibition by polarity reversal. (a) Unipolar pulse with and amplitude of 500 mV and duration of 75 µs. (b) Bipolar pulse with and amplitude of 500 mV and duration of single polarity of 75 µs. This simulation of the Hodgkin-Huxley model was performed in Mathematica 9.0 using parameter values from (Hodgkin et al., 1952)

In Chapter 5, we utilized a polarity reversal in the H-FIRE waveform to non-thermally ablate brain tissue without causing muscle contractions (Arena, Sano, Rossmeisl, et al., 2011). In later work on implanted tumors in mice (Chapter 6) and spontaneous tumors in equine patients (data not shown), H-FIRE was used to successfully treat spontaneous tumors, but slight twitching was observed in adjacent musculature. Therefore, it is likely that the ability of H-FIRE to eliminate or reduce muscle contractions depends on the location of treatment relative to nervous and muscle tissue.

Here, we attempt to improve our understanding of this relationship by developing an analytical model of nerve and muscle stimulation for optimization of H-FIRE pulse parameters. For the nerve model, the Nobel Prize winning Hodgkin-Huxley dynamical set of PDEs is utilized (Hodgkin et al., 1952), and for the muscle model, a similar mathematical procedure is implemented with updated constants and membrane potentials (Adrian et al., 1968). Strength-duration curves were developed for H-FIRE waveforms of varying amplitude and frequency. The calculated thresholds for nerve and muscle stimulation were then translated to an analytical model of electric field distribution during a clinical procedure to compare the relative ablation area with the area of tissue that is excited.

7.2 – Methods

The governing equations for nerve and muscle stimulation were derived for a planar cell geometry (Figure 7.2). This allows for decoupling of geometric effects from ion channel dynamics (Boinagrov et al., 2010), as all current travels across the cell membranes and through the cytoplasm. Applying Kirchhoff's current law, the membrane voltage (V) can be described by:

$$C\frac{dV_1}{dt} = J_{stim} + \frac{-V_1+V_2}{R} + g_{Na,1}(E_{Na} - V_1) + g_{K,1}(E_K - V_1) + G_L(E_L - V_1) \quad (1)$$

$$C\frac{dV_2}{dt} = -J_{stim} + \frac{V_1-V_2}{R} + g_{Na,2}(E_{Na} - V_2) + g_{K,2}(E_K - V_2) + G_L(E_L - V_2) \quad (2)$$

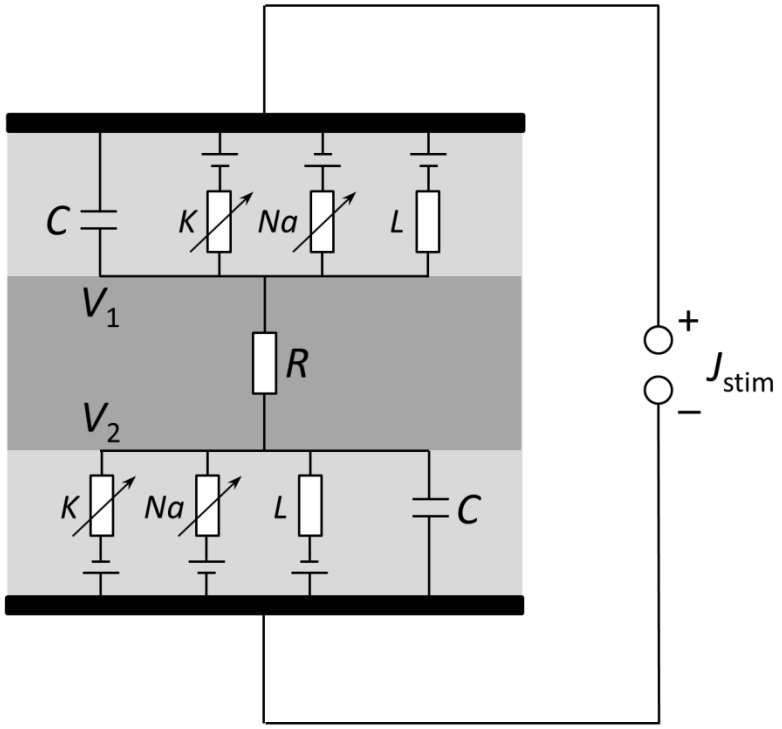

Figure 7.2. Planar cell geometry and equivalent circuit model. The upper and lower membranes (light gray) represent the faces of the soma, which is separated by the cytoplasm (dark gray). Each membrane contains a capacitive element representing the lipid bilayer as well as variable resistors representing the ion channels. The cytoplasm is represented by a constant resistance.

where $g_{Na,i}$, $g_{K,i}$, are time dependent equations for sodium and potassium conductance of each membrane (i = 1, 2), respectively:

$$g_{Na,i} = G_{Na} {m_i}^3 h_i \quad (3)$$

$$g_{K,i} = G_K n_i^4 \quad (4)$$

and *m*, *h*, and *n* are the gating variables that describe the underlying kinetics of the sodium and potassium channels:

$$\frac{dm_i}{dt} = \alpha_{m,i}(1 - m_i) - \beta_{m,i} m_i \quad (5)$$

$$\frac{dh_i}{dt} = \alpha_{h,i}(1 - h_i) - \beta_{h,i} h_i \quad (6)$$

$$\frac{dn_i}{dt} = \alpha_{n,i}(1 - n_i) - \beta_{n,i} n_i \quad (7)$$

where $\alpha_{m,\,h,\,n}$ and $\beta_{m,\,h,\,n}$ are rate constants that depend on the membrane voltage and can be found in (Adrian et al., 1968) for muscle and nerve. The parameters *m, h,* and *n* vary between 0 and 1 as functions of time to modulate the ion channel conductances from 0 to their maximum values at G_{Na} and G_K. These values, along with the remaining constants from Equations 1 – 4, are listed in Table 7.1. The resting potentials for the nerve model were normalized to – 62 mV, and the resting potentials for the muscle model were normalized to – 95 mV (Adrian et al., 1968).

Table 7.1. Constants for the analytical model of nerve stimulation.

Parameter	Nerve Value	Muscle Value	Units
G_{Na}	120	70	mS cm^{-2}
G_K	34	20	
G_L	0.3	0.3	
E_{Na}	115	145	mV
E_K	-12	25	
E_L	11	0	
R	0.1	0.1	Ω cm^2
C	1	1	μF cm^{-2}

The value of resistance was calculated based on a 50 ns cell polarization time, τ_p (Boinagrov et al., 2010), where τ_p = RC/2, and C/2 is the capacitance of the two membranes connected in series. Bipolar stimulus waveforms were constructed as a series of step functions with variable durations of single polarity and a constant delay of 2μs between the pulses. Pulses were repeated until an equivalent on-time of 100 μs was reached. These pulse characteristics are consistent with experimental waveforms used in Chapters 6 and 8.

The system of equations were solved in Mathematica 9.0 (Wolfram, Champaign, IL, USA) using the *NDSolve* function. In order to calculate strength-duration curves, a specific H-FIRE waveform was selected, and the amplitude was slowly increased using the *Manipulate* function until an action potential was observed. This procedure was repeated for all pulse durations (*d*). During the evaluation of muscle thresholds, the solution became unstable for durations less than 10 μs. This was alleviated by raising the resistance to 10 Ω cm^2, however, increasing the resistance also decreases the stimulation threshold. It was determined that at the higher resistance, the threshold for muscle stimulation was approximately five times greater than nerve stimulation at all pulse durations tested. This is in agreement with published results (Sobotka et al., 2011). Therefore, muscle thresholds at the correct, low resistance value were determined by multiplying the nerve thresholds by a factor of five.

Following the determination of stimulation thresholds for muscle and nerve, the analytical solution to Laplace's equation for two infinite cylinders was computed in Mathematica to simulate clinical IRE and H-FIRE procedures. The electrodes (1 mm Ø) were spaced 1 cm apart, and the electric field distribution was solved according to (Corovic et al., 2007):

$$E(z) = \left| \frac{V/2}{\log(d/r)} \frac{1}{z-d} - \frac{V/2}{\log(d/r)} \frac{1}{z+d} \right| \quad (8)$$

where d is the distance from the center of the electrodes to the origin, r is the radius of the electrodes, and $z = x + iy$. Using the electric field thresholds (E_T) for cell death determined in Chapter 8, an equivalent applied voltage was determined that resulted in the same ablation area for various H-FIRE and IRE pulse durations. These results are summarized in Table 7.2.

Table 7.2. Equivalent ablation parameters and stimulation thresholds

Frequency (kHz)/Duration of single polarity (μs)	Equivalent Voltage (V)	E_T – ablation (V cm^{-1})	E_T – stimulation (muscle/nerve) (V cm^{-1})
2000/0.25	5000	2500	5223.0/1044.6
250/2	2000	1000	409.8/82.0
100/5	1800	900	164.5/32.9
10/50	1350	675	15.8/3.2
-/100	1000	500	4.7/0.9

The current density values for muscle and nerve stimulation were converted to electric field strengths by solving:

$$E = \frac{J_{stim}}{\sigma} \qquad (9)$$

where σ is the electrical conductivity of the tissue. The tissue conductivity was assumed to be 0.1 S/m, which is in the range of typical values for interior muscle (Polk et al., 1996). This results in an electric field threshold for muscle and nerve stimulation of 4.72 V/cm and 0.944 V/cm, respectively, for a 100 μs unipolar pulse (Table 7.2). These values are nearly identical to those used in a study by Goldberg and Rubinsky (5 V/cm and 1 V/cm) that considers muscle contractions during electroporation-based therapies (Golberg et al., 2012). The electric field contours representing muscle and nerve stimulation were then compared to those representing tissue ablation. The area (A) within each of the contours was calculated according to Green's theorem:

$$A = \iint \left(\frac{\partial g}{\partial x} - \frac{\partial f}{\partial y}\right) dxdy = \oint f(x,y)dx + g(x,y)dy = \oint xdy \qquad (10)$$

where

$$\frac{\partial g}{\partial x} = 1 \rightarrow g = x + c_1 \text{ and } \frac{\partial f}{\partial y} = 0 \rightarrow f = c_2 \qquad (11, 12)$$

The contours were converted to a list of points [(x_1, y_1), …, (x_n, y_n)] and the integral was re-written as a summation:

$$A = \frac{1}{2}\sum_{i=1}^{N} x_n y_{n+1} - x_{n+1} y_n \qquad (13)$$

7.3 –Results and Discussion

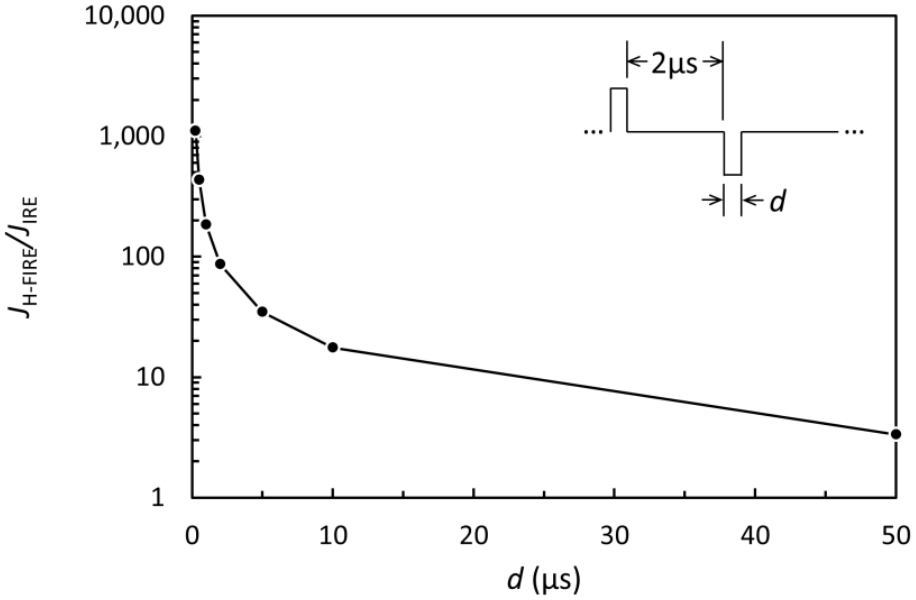

Figure 7.3. Strength-duration curve for H-FIRE waveforms. The curves for muscle and nerve stimulation are identical, because they are each normalized to their respective stimulation threshold for a 100 µs unipolar pulse.The insert describes the how the H-FIRE waveform maintains a constant 2 µs delay between pulses of alternating polarity and varying duration.

To the best of our knowledge, this is the first time a strength-duration relationship is presented for a waveform that is characteristic of H-FIRE (Figure 7.3). As mentioned, a 2 µs delay is included between square pulses of alternating polarity and varying duration. Single bipolar cycles are repeated until an equivalent on-time of 100 µs is generated. This translates to a greater number of cycles for shorter pulse durations. The total widths of the bipolar bursts exceed

that of a 100 µs unipolar pulse, with bursts containing the shortest pulses having the longest widths. However, as the pulse duration is reduced, the stimulation threshold increases. On a *log-log* plot this is a linear relationship fit by the equation ($y = 207.44x^{-1.079}$) with an R^2 value of 0.997. It is important to note that the curves for muscle and nerve are identical, as each were normalized by their stimulation threshold value for a 100 µs unipolar pulse, 4720 µA cm^{-2} and 944 µA cm^{-2}, respectively.

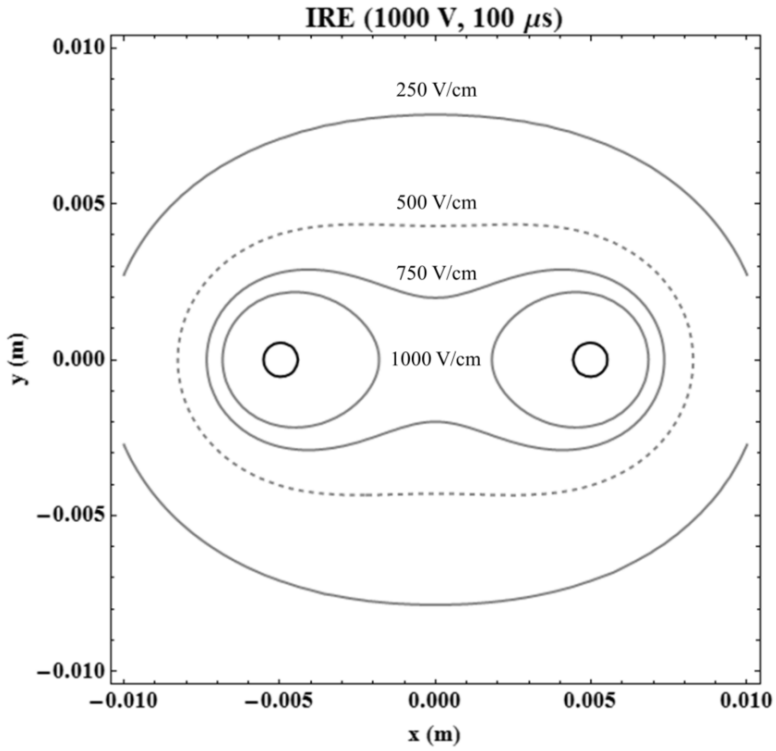

Figure 7.4. Electric field distribution in the tissue during a clinical IRE procedure. The 500 V/cm contour (dashed) indicates the threshold for cell death when a series of 80, 100 µs unipolar pulses are applied. The location and size of the electrodes are indicated as the smallest contours.

The analytical solution to Laplace's equation for a clinical IRE procedure is shown in Figure 7.4. In this case, the applied voltage is 1000 V, and the electric field threshold for cell death is 500 V/cm. In Figure 7.5, the same ablation area is achieved for different H-FIRE waveforms by altering the applied voltage according to Table 7.2. By overlaying the corresponding electric field contours for muscle and nerve stimulation, it is possible to visualize how the tissue would respond in each case. As the duration of single polarity is reduced, the area

of tissue being stimulated is also reduced. For a duration of single polarity of 250 ns, it becomes theoretically possible to ablate the tissue without causing muscle contractions (assuming the muscle cells within the ablation area do not contract). Additionally, at this pulse duration, the area of possible nerve stimulation only exceeds the ablation area by approximately 3 mm in length and 5 mm in width.

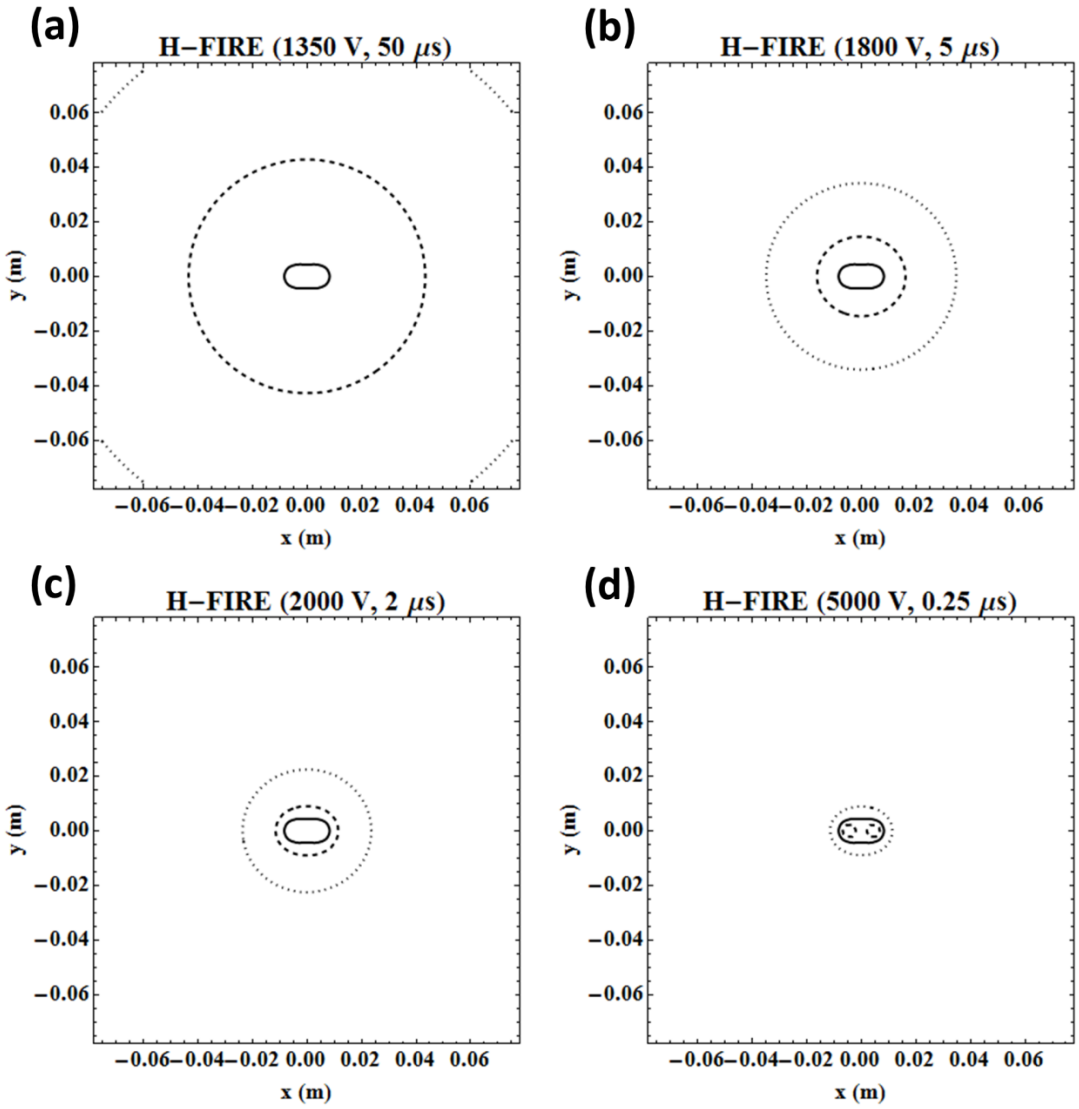

Figure 7.5. Illustration of volume of tissue being stimulated versus ablated. Duration of single polarity is reduced from (a) to (d) while the applied voltage is increased to maintain a constant ablation area (solid line). Stimulation thresholds for muscle (dashed) and nerve (dotted) are superimposed.

A quantitative comparison of the areas of tissue being stimulated versus ablated is shown in Figure 7.6. For a 100μs unipolar IRE pulse, the area of muscle and nerve stimulation is 116 and 581 times greater than the area being ablated, respectively. These numbers are reduced drastically as bipolar H-FIRE waveforms are implemented. For a 2 μs duration of single polarity, the area of muscle stimulation is only 2.6 times the ablation area. Depending on the proximity of the treatment site to the surrounding musculature, it then becomes feasible to perform ablations without causing muscle contractions. By fitting power relationships to the data, it is estimated that concerns associated with direct stimulation of muscle should be alleviated for pulse durations less than 896 ns, and concerns associated with muscle contractions through indirect nerve stimulation should be alleviated for pulse durations less than 99 ns.

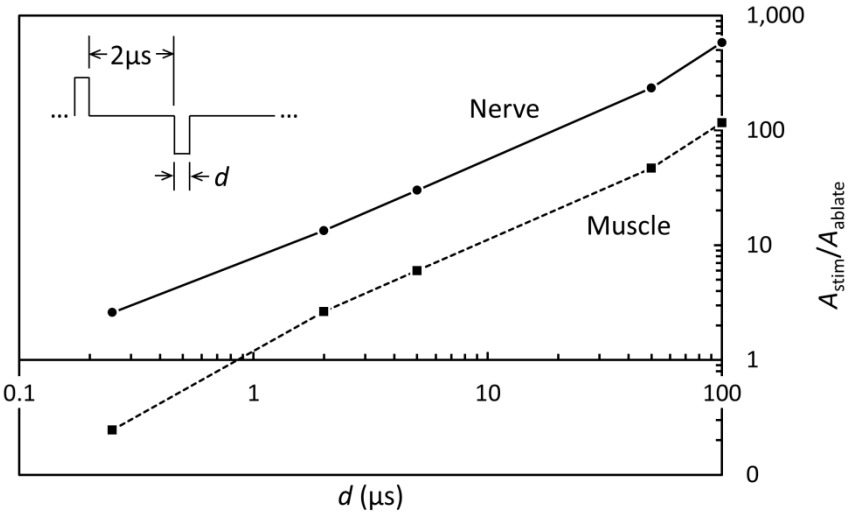

Figure 7.6. Stimulation area normalized to ablation area. For a given treatment protocol, the area of nerve stimulation (solid line) exceeds the area of muscle stimulation (dashed line). The linear relationships on *log-log* axes are fit by the equations $y = 7.8989x^{0.8944}$ ($R^2 = 0.9959$) and $y = 1.1153x^{0.9982}$ ($R^2 = 0.996$) for nerve and muscle, respectively.

7.4 – Limitations and Conclusions

The constants used in the analytical models for nerve and muscle stimulation were based on experimental data from squid giant axon and frog sartorius muscle, respectively. New

constants should be determined in future work based on human recordings. Additionally, the planar cell geometry employed to study stimulation is a simplification of real cell morphologies. The uniform voltage values present on planar cell membranes vary continuously for spherical (soma) and cylindrical (axon) membranes as a function of the angle of the field. Boinagrov *et al.* have shown that qualitatively, stimulation trends are the same for all three geometries, but that stimulation thresholds are lower for spherical and cylindrical cells by a factor of 1.75 due to varying degrees of membrane polarization (Boinagrov et al., 2010). Finally, the model presented is for an unmyelinated nerve, and myelinated nerves have a lower chronaxie value (minimum duration required to double the threshold of an infinite pulse duration). This means that myelinated nerves are easier to stimulate using pulse durations around their chronaxie value (30 to 600 µs), assuming similar rheobase values (stimulation threshold of an infinite pulse duration) (West et al., 1983). Future work should account for these added complexities in order to improve the accuracy of the calculated stimulation thresholds.

The results indicate that H-FIRE is capable of producing IRE size lesions with a fraction of the associated nerve and muscle stimulation. Additionally, the lack of muscle contractions seen in Chapter 5 during H-FIRE of brain tissue using pulse durations of 2 µs may be linked to the fact that neck musculature was outside the zone of direct muscle stimulation. During H-FIRE of implanted tumors in mice (Chapter 6), pulse durations of 5 µs resulted in localized twitching around the treatment site due to the nearby leg musculature. Based on these results, a strong argument can be made for developing a new pulse generator capable of producing comparable ablation areas with 250 ns pulses. This has the potential to eliminate direct muscle stimulation altogether independent of the location of muscle tissue.

8 – Development of a 3D *In Vitro* Tumor Platform for Treatment Planning of IRE and H-FIRE[3]

8.1 – Introduction

Developing accurate IRE treatment planning models is essential in order for the technology to achieve widespread clinical use. Currently, the predictability of IRE outcomes relies upon one's ability to predict the electric field distribution in the tissue and an *a priori* knowledge of the electric field threshold for cell death given a specific set of pulse parameters (duration, number, repetition rate). This is a complicated task. Altered membrane permeability leads to non-linear changes in the dielectric tissue properties. Additionally, while thermal damage is avoided by properly tuning the pulse parameters, there can still be significant Joule heating within the tissue that influences the dielectric response. Many studies have been performed to investigate the physiological response of various tissue types to IRE pulses without focusing on the engineering aspects of treatment planning (Appelbaum et al., 2012; Ben-David et al., 2012; Bower et al., 2011; Charpentier et al., 2010). To the best of our knowledge, the electric field threshold for cell death has only been well documented *in vivo* for liver tissue (J. F. Edd et al., 2006; Miklavcic et al., 2000; Sano et al., 2010), brain tissue (Garcia et al., 2010), and an orthotopic model of mammary tumors in mice (Neal et al., 2010). Additionally, studies conducted to elucidate the dynamic relationship between IRE and changes in dielectric properties are limited to experiments on liver (Ivorra et al., 2007; Miklavcic et al., 2004), skin (N. Pavselj et al., 2005), brain (Garcia, Rossmeisl, et al., 2011), kidney (Neal et al., 2012), and a subcutaneous model of fibrosarcoma in mice (Ivorra, Al-Sakere, et al., 2009). Many types of tissue remain unexplored, including a variety of tumors. This can partially be attributed to the cost and

[3] Chapter 8 is adapted and reprinted with permission. © 2012 Elsevier. Arena, C. B., Szot, C. S., Garcia, P. A., Rylander, M. N., and Davalos R. V., A Three-Dimensional In Vitro Tumor Platform for Modeling Therapeutic Irreversible Electroporation, Biophysical Journal, 103(9), 2033-2042, Nov 2012.

difficulty associated with performing *in vivo* experiments.

A broader literature exists on *in vitro* cell suspensions (Miller et al., 2005; R. E. Neal et al., 2009; Shafiee et al., 2009). In this platform, the electric field threshold for cell death can be readily determined by using commercially available indicators of membrane integrity or mitochondrial activity. However, there are significant limitations associated with using information derived from this model for treatment planning. Cells in suspension do not provide an accurate representation of their *in vivo* morphology, and the cellular response obtained from these cultures is altered in the absence of cell-cell and cell-matrix interactions. Additionally, cells in suspension lack the structural foundation necessary to provide useful spatial information following pulse delivery. To account for spatial information, researchers have proposed using vegetable tissue, such as potato. Potatoes are useful for economically determining field thresholds, because regions subject to IRE are markedly darker (Hjouj et al., 2010; Ivorra, Mir, et al., 2009). Additionally, changes in potato dielectric properties during IRE have been shown to mimic those seen *in vivo* (Ivorra, Mir, et al., 2009). However, while vegetables are useful for economically investigating trends, it is difficult to draw direct comparisons to tissue with the absence of physiologically responsive cancer cells.

There is a clear need for a system that can be used to model IRE-based cancer therapies and improve treatment planning in a more physiologically relevant manner without requiring the use of animal models. It has been well established in the fields of tissue engineering and cancer biology that cells cultured within a three-dimensional (3D) *in vitro* environment are capable of acquiring phenotypes and responding to stimuli analogous to *in vivo* biological systems (Griffith et al., 2006; Kim, 2005; Yamada et al., 2007). We hypothesize that engineering a platform for 3D tumor growth that mimics an *in vivo* tumor microenvironment will allow the cells to respond

to IRE-based therapies in a manner that can be directly related to an *in vivo* response, and therefore, have direct clinical impact. Several groups have investigated the phenotypic response of culturing cancer cells in a 3D *in vitro* environment (Fischbach et al., 2007; Szot et al., 2011; Verbridge et al., 2010). Specifically, our group has developed 3D bioengineered tumors that exhibit phenotypic characteristics representative of *in vivo* cancer progression (Szot et al., 2011). This model involves culturing cancer cells within dense collagen I hydrogels, which facilitates proper cell-cell and cell-matrix interactions and encourages the development of a necrotic core, intra-cellular levels of hypoxia, and angiogenic potential. Therefore, these collagen I hydrogel-based bioengineered tumors can potentially be used for more accurate modeling of IRE-based cancer therapies in an *in vitro* setting.

In this study, a 3D cancer cell culture model is introduced for improving IRE treatment planning. Changes in electrical conductivity and temperature were measured for a range of applied voltages. Additionally, the role of cell concentration was explored in producing an electrically relevant model of tissue. Following treatment, a live/dead assay was performed on intact constructs to demonstrate the relationship between the applied voltage and the extent of cell death. Select samples were fixed and processed for H&E staining. All data generated was incorporated into a numerical model. This allowed for the accurate determination of the electric field threshold for cell death (500 V/cm). These results were then compared to experiments using *in vitro* cell suspensions, which predicted a much higher threshold for cell death (1500 V/cm), illustrating the benefits of 3D cell culture models for IRE treatment planning. Following the evaluation of IRE on the *in vitro* tumors, H-FIRE was performed and analyzed in a similar fashion to determine electric field thresholds for cell death at varying burst frequencies.

8.2 – Materials and Methods

8.2.1 – Cell Culture

Primary dispersed murine pancreatic cancer cells (provided by Dr. Dieter Saur) were established from pancreatic ductal adenocarcinomas (PDAC) of *Ptf1a*$^{Cre/+}$*; LSL-Kras*$^{G12D/+}$ mice on a C57Bl/6J genetic background. Specifically, primary pancreatic tumors (PPT) were removed from a mouse (number 8182) and digested in 10 ml DMEM containing 150 U/ml collagenase Type 2 (Worthington, Lakewood, NJ, USA) as described (von Burstin et al., 2009). Single PPT-8182 cell suspensions were cultivated in DMEM (supplemented with L-glutamine; ATCC, Manassas, VA, USA) containing 10% FBS (Sigma Aldrich, St. Louis, MO, USA) and 1% Penicillin/Streptomycin (Invitrogen, Carlsbad, CA, USA). These cells have been shown to replicate human pancreatic cancer in terms of histology, metastasis, and genetic alterations (Saur et al., 2005; Seidler et al., 2008; von Burstin et al., 2009).

8.2.2 – Collagen I Hydrogel In Vitro Tumors

Collagen I hydrogel-based *in vitro* tumors were fabricated as described previously (Szot et al., 2011). Briefly, Sprague Dawley rat tail tendons were dissolved in 10 mM HCL under agitation overnight, the suspension was centrifuged at 22,500 g for 45 min, and the supernatant containing the collagen I was decanted. The concentration of the collagen I solution was calculated using dry weight measurements, and the solution was sterilized by layering chloroform beneath the collagen I for 24 hr. A neutralizing buffer containing 10x DMEM (Mediatech Inc., Manassas, VA, USA), 1N NaOH, and dH_20 was used to re-suspend a pellet of PPT-8182 cells to obtain a final seeding density of 5×10^6 or 50×10^6 cells/ml. The cell suspension was then gently mixed on ice with an appropriate volume of collagen I to achieve a concentration of 8 mg/ml, which provides a matrix stiffness close to measured values for *in vivo* tumors

(Paszek et al., 2005), and pipetted into 10 mm diameter cylindrical molds. Following a 20 min polymerization period at 37°C, the cancer cell-seeded hydrogels were removed from the molds and cultured in complete media overnight prior to IRE pulse delivery. It is important to note that the 5×10^6 cells/ml seeding density was used in a majority of the experiments, because this was found to adequately maintain cell viability throughout the construct over a 24 h period. The seeding density of 50×10^6 cells/ml was used to investigate if a higher concentration of cells could modulate the electrical properties of the *in vitro* tumors. Control hydrogels were also fabricated using the neutralizing buffer alone without cells as a comparison to elucidate any effects due to electroporation.

8.2.3 – IRE Pulse Delivery and Viability Analysis for In Vitro Tumors

In vitro tumors were temporarily removed from media and placed in 6-well plates for IRE pulse delivery. Pulses were applied through custom electrodes (1.3 mm Ø) fabricated from stainless steel hollow dispensing needles (Howard Electronic Instruments Inc., El Dorado, KS, USA) using the ECM 830 electroporation system (BTX-Harvard Apparatus, Holliston, MA, USA) (Figure 8.1 a). The pulse duration (100 µs), number (80 pulses), and repetition rate (1 pulse/sec) were held constant and chosen based on established protocols (B. Al-Sakere et al., 2007; Onik et al., 2007). In the 5×10^6 cells/ml seeded *in vitro* tumors, the applied voltage was varied (0 V, 150 V, 300 V, 450 V, and 600 V) to generate voltage-to-distance ratios of 0 to 1800 V/cm across the 3.35 mm electrode spacing (center-to-center). In the no cells control and 50×10^6 cells/ml seeded *in vitro* tumors, the applied voltage was held constant at 300 V. Prior to the full IRE protocol, a pre-pulse was delivered at 30 V to determine the baseline electrical conductivity of the *in vitro* tumors. A port located 2.3 mm below the center point between the electrodes was included in the electrode design to monitor temperature in real-time during treatment with a fiber

optic probe (Luxtron m3300, LumaSense Technologies Inc., Santa Clara, Ca, USA). Additionally, current (TCP305 and TCPA300, Tektronix, Beaverton, OR, USA) and voltage (P5200, Tektronix, Beaverton, OR, USA) were recorded non-invasively during treatment. The generated temperature, current, and voltage data was used to validate the numerical model for predicting the electric field threshold for IRE (see Results section 5.3). Further, to eliminate the influence of the temperature probe on the electrical measurements, samples used for monitoring temperature were separate from those used for performing the viability analysis. Following each treatment, the tumor diameter and thickness were measured with calipers for use in determining electrical properties. Each parameter combination was tested a minimum of three times (n = 3).

Following IRE pulse delivery, the *in vitro* tumors were incubated in complete media for 2 h before conducting a live/dead assay to allow any cells experiencing reversible electroporation to fully recover (Kanduser et al., 2006). Calcein AM (4 μM; λ_{em} = 515 nm, Invitrogen) was added to the media 30 min prior to analysis, and propidium iodide (1.5 mM; λ_{em} = 617 nm, Invitrogen) was added to the media 5 min prior to analysis. Calcein AM stains live cells, as it can be transported across the cell membrane and fluoresces when intracellular esterases remove the attached acetomethoxy (AM) group. Propidium iodide (PI) fluorescently labels dead cells, as it only enters compromised cell membranes and binds to nucleic acids. A Leica DMI 6000 fluorescent microscope (Leica Microsystems Inc., Buffalo Grove, IL, USA) was used to tile a set of images and reconstruct the entire surface of the IRE-treated *in vitro* tumors. A Zeiss LSM 510 laser scanning confocal microscope (Carl Zeiss, Thornwood, NY, USA) was used to analyze the live-dead cell interface and reconstruct a Z-stack.

In addition, cytoskeletal disruption within the IRE-treated regions was investigated. The tumors were stained with rhodamine phalloidin (Invitrogen), a high-affinity probe for F-actin,

and NucBlue™ Fixed Cell Stain (Invitrogen), to visualize nuclei, The samples were then routinely fixed in 10% formalin, paraffin embedded, and sectioned at 5 µm for histological analysis. A hemotoxylin and eosin (H&E) stain was performed to further analyze cell death within the IRE-treated regions.

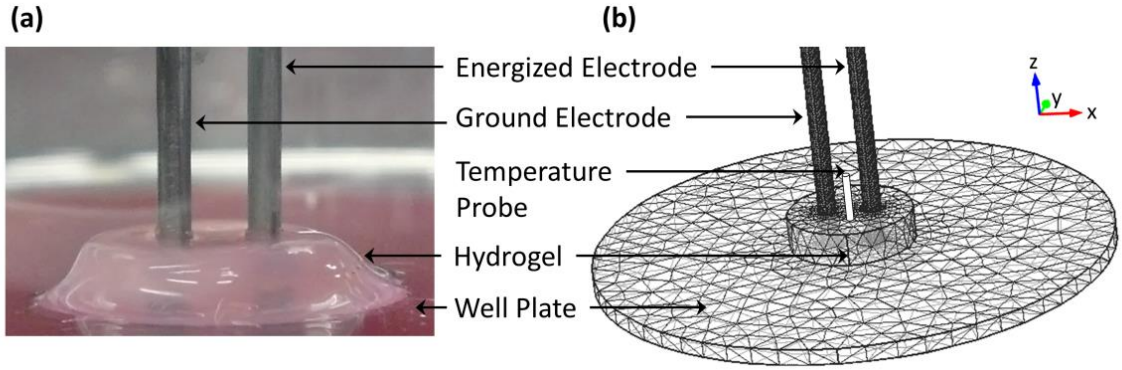

Figure 8.1. Collagen I hydrogel-based *in vitro* tumor experimental overview. (a) Experimental setup for IRE pulse delivery in collagen I hydrogel-based *in vitro* tumors, in which PDAC cells are embedded. (b) Geometry and mesh used in the finite element model for simulating the electrical and thermal response of the *in vitro* tumors to IRE.

8.2.4 – IRE Pulse Delivery and Viability Analysis for Cell Suspensions

PPT-8182 cells were suspended at a concentration of 5×10^6 cells/ml in electroporation buffer, which was created by mixing (3:1) complete culture media with dielectrophoresis buffer (8.5% sucrose, 0.3% glucose, and 0.725% basal media). This mixture was selected to obtain a solution with an electrical conductivity of 1 S/m, as determined by a conductivity meter (B-173, Horiba, Kyoto, Japan). A conductivity of 1 S/m resembled the baseline conductivity of the collagen I hydrogels and allowed for the delivery of electric fields up to 1500 V/cm without arcing or significant bubble formation due to electrolysis. A micro-osmometer (3MO Plus, Advanced Instruments Inc., Norwood, MA, USA) was used to confirm that the osmolality of the buffer (315 mOsm/kg) was near the value for complete culture media (320 mOsm/kg) and well within the physiological range (300 to 340 mOsm) (Puttaswamy et al., 2010).

For each treatment, 250 µl of cell suspension was pipetted into an electroporation chamber (HT-P96-4, BTX-Harvard Apparatus, Holliston, MA, USA) with parallel plate electrodes. IRE pulses were applied as described above with a fixed pulse duration (100 µs), number (80 pulses), and repetition rate (1 pulse/sec). The applied voltage was varied (0 V, 200 V, 400 V, 500 V, and 600 V) to generate electric fields ranging from 0 to 1500 V/cm across the 4 mm electrode gap (edge-to-edge). Each parameter combination was repeated five times (n = 5).

Following IRE pulse delivery, samples were removed from the electroporation chambers, pipetted into 1.5 ml microcentrifuge tubes, and kept on ice for 1 h to allow adequate time for the cells to recover from any reversible electroporation effects (Kanduser et al., 2006). A dye exclusion assay was performed by mixing samples 1:1 with a 0.4% Trypan Blue solution (T8154, Sigma-Aldrich, St. Louis, MO, USA). Samples were then pipetted into an Ultra-plane Neubauer's hemocytometer (Hausser Scientific, Horsham, PA, USA) and placed under an inverted light microscope (Olympus CKX41, Center Valley, PA, USA). Live and dead cell counts were obtained assuming that live cells exclude Trypan Blue and dead cells absorb it, providing a clear indicator of cell death. Percent viability was based on the ratio of the number of blue cells to the total number of cells and normalized to the 0 V sham group.

8.2.5 – H-FIRE Pulse Delivery and Viability Analysis for In Vitro Tumors

To evaluate H-FIRE thresholds, *in vitro* tumors were constructed and analyzed in a similar fashion to that described above. The main difference was that the cell line was selected from a human patient with a grade IV astrocytoma (U-87 MG, ATCC, Manassas, VA, USA). The same custom pulse generator described in the mouse study (Chapter 6) was utilized here to deliver high-frequency, bipolar bursts with center frequencies of 2 MHz, 250 kHz, 100 kHz, and 10 kHz, which corresponds to a duration of single polarity of 250 ns, 2 µs, 5 µs, and 50 µs,

respectively. The applied voltage was held constant at 540 V_{peak} for a center-to-center voltage-to-distance ratio of 1612 V/cm. Additionally, the total on-time for each burst was 100 μs (50 μs in each polarity), and 80 bursts were delivered once per second.

8.2.6 – Numerical Modeling

Using similar techniques to those presented in Chapter 4, COMSOL was used to solve for the electric field and temperature distributions within the *in vitro* tumor during IRE therapy. A 3D geometry was constructed with equivalent dimensions to the experimental setup (Figure 8.1 b). Each treatment was performed in a single well of a polystyrene six well plate with a thickness of 1.2 mm and radius of 1.9 cm. The stainless steel electrodes had a length of 5.5 cm through which heat could dissipate. A finer mesh was used that consisted of 67,557 tetrahedral elements. This resulted in less than a 0.02% difference in temperature calculations at the site of the fiber optic probe upon successive refinements.

In order to solve for the baseline electrical conductivity of the *in vitro* tumors, a 3 variable parametric study was performed on the tumor radius (4.5, 4.75, and 5 mm), thickness (2, 2.5, and 3 mm), and conductivity (0.25, 0.5, 0.75, 1.0, 1.25 S/m) using the numerical model. Based on the pulse characteristics associated with IRE and the subdomain dielectric (Table 8.1) and geometry properties, propagation effects and transients were assumed to be negligible, and the quasistatic approximation was implemented. This is consistent with others who have developed techniques for modeling electroporation performed with pulse durations on the order of 100 μs (J.F. Edd et al., 2007; Natasa Pavselj et al., 2011) and allows for definition of the electric field as $E = -\nabla\phi$, where ϕ is the electric potential. Therefore, the spatial distribution of electric potential can be expressed as:

$$0 = -\nabla \cdot (\sigma_0 E) \qquad (1)$$

where σ_0 is the baseline electrical conductivity. Equation 1 was used to solve for the total current flowing in the *in vitro* tumor when a constant 30 V pre-pulse was applied to the energized electrode, with the other electrode set as ground. Specifically, the magnitude of the current density (J) was integrated over a cut plane dividing the geometry in half between the electrodes. All outer boundaries, excluding the electrodes, were assumed to be electrically insulating ($-n \cdot J = 0$), and the initial voltage (V_0) within each subdomain was 0 V.

Table 8.1. Physical properties used in the numerical simulations.

Parameter	Tumor	Electrode[†]	Plate[‡]
k (W m^{-1} K^{-1})	0.6	14	0.14
c (J kg^{-1} K^{-1})	4181.8	477	1300
ρ (kg m^{-3})	997.8	7900	1050
σ_0 (S m^{-1})	1.2	2.22×10^{6}	1×10^{-16}

The resulting data relating current (I) to each parameter combination was imported into Mathematica 8.0 (Wolfram, Champaign, IL, USA). A regression analysis was performed to determine the baseline electrical conductivity using the measured current from the pre-pulse routine along with the corresponding tumor dimensions. For comparison to the experimentally determined values for *in vitro* tumor baseline electrical conductivity, a theoretical calculation was performed using effective medium theory (EMT) (Pavlin, Slivnik, et al., 2002). Specifically, Maxwell's equation for a dilute suspension was solved for the effective conductivity, σ:

$$\frac{\sigma_e - \sigma}{2\sigma_e + \sigma} = f\frac{\sigma_e - \sigma_p}{2\sigma_e + \sigma_p} \qquad (2)$$

where σ_e is the extracellular medium conductivity (1.2 S/m), σ_p is the homogeneous particle conductivity (0.2×10^{-4} S/m for an equivalent cell (Pavlin, Slivnik, et al., 2002)), and f is the volume fraction of particles dispersed in the medium. Equation 4 is valid for predicting the low-

frequency effective conductivity of a cell suspension for volume fractions up to 0.8 (Polk et al., 1996). This allowed for extrapolations of tumor baseline conductivity at cell concentrations higher than those tested experimentally in order to estimate what cell concentration would be required to be electrically similar to tissue.

The temperature distribution (T) within the *in vitro* tumor was obtained by transiently solving a modified heat conduction equation with inclusion of the Joule heating source term ($J \cdot E$):

$$\rho c \frac{\partial T}{\partial t} = \nabla \cdot (k \nabla T) + \frac{\tau(\sigma |E|^2)}{P} \qquad (3)$$

where τ is the pulse duration, P is the period of the pulses, k is the thermal conductivity, c is the specific heat at constant pressure, and ρ is the density (Table 8.1). References values are taken from (B. Al-Sakere et al., 2007)[†] and (Chiu et al., 1979)[‡]. Due to the fact that the collagen I hydrogel-based tumors have a water content of greater than 98%, the thermal properties of the tumor were chosen to be the same as water. The tumor baseline electrical conductivity (1.2 S/m) was determined experimentally from the average of the no cells and 5×10^6 cells/ml trials (Table 8.2), as there was no statistical difference between those two groups (see Results section 8.3.2). Additionally, the tumor radius (4.705 mm) and thickness (2.45 mm) was also selected by averaging the measurements from the same groups. Equation 1 was modified to include a temperature dependence on electrical conductivity:

$$0 = -\nabla \cdot (\sigma(T) E) \qquad (4)$$

where

$$\sigma(T) = \sigma_0 \big(1 + \alpha (T - T_0)\big) \quad (5)$$

and α is the coefficient that describes how the conductivity varies with temperature. This parameter was estimated to be 2 %/°C by optimizing the measured change in temperature and current throughout treatment to match the theoretical changes. The optimization was performed by running a parametric study on α at 0.5 %/K increments. A value of 2 %/°C is similar to values observed in biological tissue (Schwan et al., 1980).

At each time step, the conductivity and electric field are determined and updated in the Joule heating term. As opposed to simulating individual pulses, a duty cycle approach was employed to calculate the temperature increase resulting from various IRE protocols. A constant voltage (150, 300, 450, and 600 V) was applied to the energized electrode, with the other electrode set as ground. The Joule heating term was scaled by the duty cycle ($\tau/P = 100\times10^{-6}$) to ensure that equal amounts of energy were deposited into the tissue by the onset of each "pulse." This approach has been validated in our previous work (Arena, Sano, Rossmeisl, et al., 2011; Neal et al., 2012) as providing an accurate prediction of the temperature distribution with a fraction of the computational requirements necessary to resolve microsecond order pules within a treatment lasting several seconds.

All outer boundaries, excluding the outer vertical edge of the well plate, were treated as convective cooling ($-n \cdot (-k\nabla T) = h(T_{ext} - T)$) with an exterior temperature of 22°C and a heat transfer coefficient of 25 (W m^{-2} K^{-1}). The vertical edge of the well plate was treated as thermally insulating ($-n \cdot (-k\nabla T) = 0$), and the initial temperature (T_0) within each subdomain was the same as the exterior temperature. Intermediate time stepping was used to ensure that at least one time step was taken each second.

8.2.7 – Determination of Electric Field Threshold for Cell Death

Following the *in vitro* tumor viability analysis, the area, height, and width of the treated region was measured using Image J (National Institutes of Health, Bethesda MD, USA) for three samples of each parameter combination and averaged. All measurements were made on the surface of the tumors. The width measurements were taken in the x-direction and the height measurements were taken in the y-direction. The electric field threshold for cell death was determined in three ways, using the area, height, and width measurements (Table 8.3). For determining the threshold from the area measurement, the electric field on the top surface of the tumors was integrated at the end of the treatment (t = 80 s) for values greater than the threshold. The threshold value was varied until the area calculation best matched the measured values within 1 V/cm (excluding the area of the electrodes). For determining the threshold from the height and width measurements, the value of the electric field at a point on the surface corresponding to the measurements was taken at the end of treatment.

8.3 – Results

8.3.1 – Physiological Response to IRE Pulse Delivery within In Vitro Tumors

When the 30 V pre-pulse was delivered to determine the baseline electrical conductivity of the *in vitro* tumors, no cell death was observed as a result of the treatment (Figure 8.2 a). At this low voltage-to-distance ratio (90 V/cm taken from center-to-center electrode spacing), any electroporation that may have occurred was reversible (Miklavcic et al., 2000). Minimal cell death was observed where the electrodes punctured the surface of the tumors. When the electric field strength was increased to 150V, cell death was observed on the medial side of both electrodes, but the treated regions did not expand far enough to completely connect (Figure 8.2 b). Rather, a transition zone of both live and dead cells was observed at the center of the two

electrodes. At the higher electric field strengths (300V, 450V), the treated region was amplified with increasing electric field strength, expanding in both the *x*- and *y*-directions (Figure 8.2 c, d). The non-specific regions of cell death present around the periphery of the tumors were a result of handling the samples with tweezers.

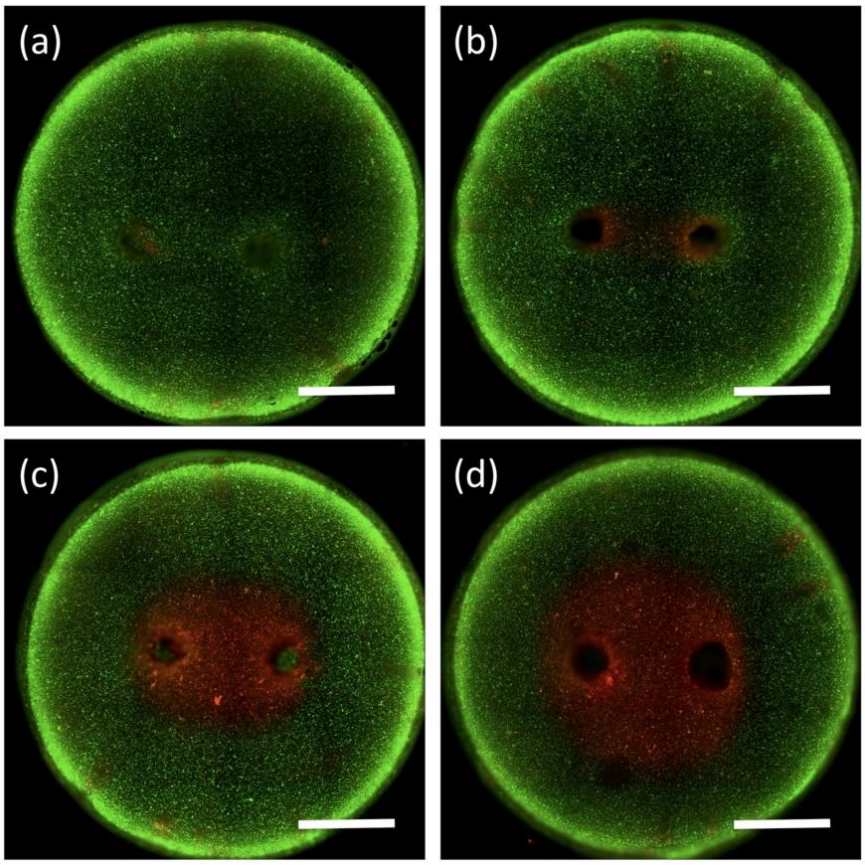

Figure 8.2. A live/dead assay for assessment of cell death following IRE. Pulses were delivered at (a) 30V, (b) 150V, (c) 300V, and (d) 450V. Live cells were stained green using Calcein AM and dead cells were stained red using propidium iodide. Images were tiled to reconstruct the entire surface of the IRE-treated *in vitro* tumors. The bright rings encircling the hydrogels are a consequence of out of plane fluorescence at the rounded edges. Scale bars represent 2.5 mm.

A sharp interface between live and dead cells was observed at the threshold boundary for cell death with sub-millimeter resolution (Figure 8.3 a). The specificity of these treatments was similar to what has been achieved during *in vivo* IRE pulse delivery (J. F. Edd et al., 2006; Onik et al., 2007). Confocal microscopy was used to show that the IRE-induced cell death was uniform in the z-direction (Figure 8.3 b), demonstrating that the *in vitro* tumors can provide

spatial information in both the *x*-*y* and *z* planes. In addition, the 3D reconstruction highlighted the transition zone at the live/dead cell interface where there were clear contrasting gradients of live and dead cells that converged at the threshold boundary for cell death.

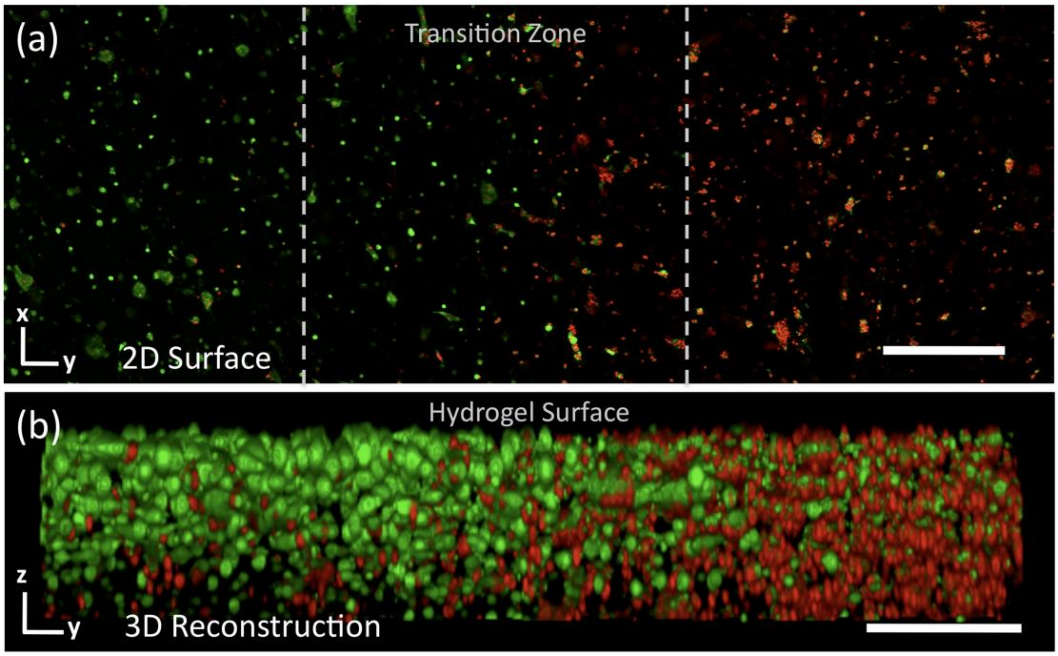

Figure 8.3. Confocal microscopy of live/dead stained *in vitro* tumors. (a) A sharp interface between live (green; left) and dead (red; right) cells at the threshold boundary for cell death with sub-millimeter resolution. (b) 3D reconstruction at this interface highlights the transition zone between live and dead cells and demonstrates that IRE-induced cell death was uniform throughout the *in vitro* tumors. The dotted lines in panel (a) indicate a representative region from which panel (b) was taken. Scale bars represent (a) 400 μm and (b) 200 μm.

Histology was used to further assess the IRE-induced cell death in the *in vitro* tumors. Again, a sharp interface between live and dead cells was evident from an H&E stain (Figure 8.4 a). The PPT-8182 cells within the un-treated regions appeared normal with healthy nuclei and complete cytoplasms, signifying that they were not affected by the IRE pulse delivery (Figure 8.4 c). Conversely, the cells within the IRE-treated regions were completely destroyed except for their remaining nuclei, which appeared abnormal and no longer contained nucleoli (Figure 8.4 b). The absence of cytoplasmic material indicated that the IRE pulses had irreversibly

compromised the cell membranes, leaving clear voids in the collagen hydrogel where the cells had been.

An F-actin stain was performed to determine the effect of the IRE pulses on the actin cytoskeleton of PPT-8182 cells cultured within the *in vitro* tumors (Figure 8.4 d and e). PPT-8182 cells within the un-treated regions had spherical morphologies with high concentrations of actin present around the periphery of the cells (Figure 8.4 e). Since the tumors were only cultured overnight prior to IRE pulse delivery, the cells did not proliferate into large clusters or develop invasive processes, as observed previously (Szot et al., 2011). The cytoskeleton of cells within the IRE-treated regions seems to be permanently disrupted, appearing speckled and faded (Figure 8.4 d). This suggests that the IRE pulses led to degradation of the actin filaments, which differs from reversible electroporation, where actin filaments have been shown to reassemble 1h following electroporation (Kanthou et al., 2006). The presence of a disrupted cytoskeleton within the IRE-treated cells revealed that some cytoplasmic material was still present following IRE pulse delivery. Over time, this remaining cytoplasm was either fully degraded or washed away during histology preparation (Figure 8.4 b). In treatment groups where the live/dead stain was not performed until 24 h following IRE-treatment, there were no visible PI-stained dead cells within the treated regions, indicating that the nuclei had also been fully degraded or washed away (data not shown).

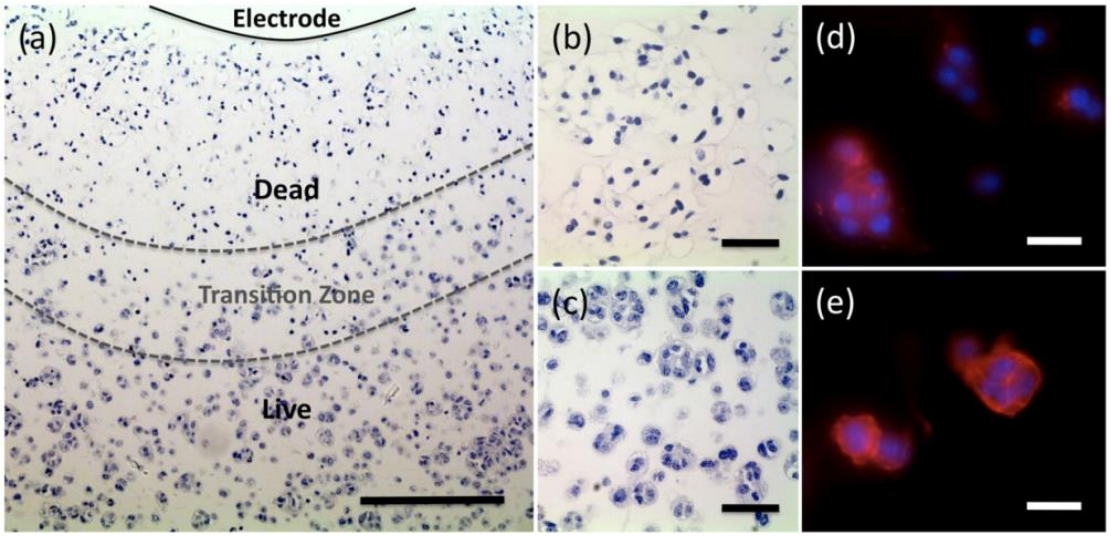

Figure 8.4. H&E and F-actin stain for assessment of cell death following IRE. (a) Pulses were delivered at 450V through *in vitro* tumors seeded with 50×10^6 cells/ml. (b) Cells stained with H&E located within the IRE-treated regions appeared to be devoid of most cytoplasmic material while (c) cells located within the un-treated regions appeared normal with intact cell membranes. The dotted lines in panel (a) highlight the transition zone at the live/dead cell interface. The F-actin stain (red) was used to determine the effect of IRE-pulse delivery on the cytoskeleton of PPT-8182 cells cultured within the (d) IRE-treated and (e) un-treated regions of the *in vitro* tumors. The actin cytoskeleton within the IRE-treated cells appears permanently disrupted. Nuclei were stained with DAPI (blue). Scale bars represent (a) 250μm, (b, c) 50μm, and (d, e) 25μm.

8.3.2 – Determination of Baseline Electrical Properties

The baseline electrical conductivity of the *in vitro* tumors is given in Table 8.2. A one-way ANOVA was used to investigate the effect of cell concentration on the rank of baseline conductivity. In the event of a significant main effect, pairwise comparisons were completed using Tukey's Honestly Significant Difference (HSD). All statistical analysis were conducted using JMP 9 (Cary, North Carolina, USA) with a significance level of $p <= 0.05$. Results indicate that a cell concentration of 50×10^6 cells/ml is high enough to produce a detectable decrease of around 0.1 S/m in baseline conductivity when compared to the 5×10^6 cells/ml group. Further, there is no significant difference in baseline conductivity between the no cells and 5×10^6 cells/ml groups. These results agree well with the theoretical calculations based on EMT. Specifically, a cell concentration on the order of 48×10^6 cells/ml is required to reduce the baseline conductivity by 0.1 S/m. This corresponds to a volume fraction of cells of approximately 0.06.

Table 8.2. Baseline electrical conductivity from pre-pulse measurements and EMT theory

Conc. (cells ml^{-1})	Experimental σ_0 (S m^{-1})	Theoretical σ_0 (S m^{-1})
0 (n = 6)	1.18 +/- 0.09	1.2
5×10^6 (n = 15)	1.24 +/- 0.11	1.2
50×10^6 (n = 6)	1.08 +/- 0.08	1.1

8.3.3 – Numerical Model Validation

The numerical model was validated through comparisons to experimentally measured changes in current and temperature between the first and last pulse of treatment (Figure 8.5). The predicted change in current delivered through the *in vitro* tumors was accurate around one standard deviation at all voltages tested (Figure 8.5 a). As the applied voltage increased, the change in current during treatment also increased. This change is non-linear due to the inclusion of a temperature dependent conductivity. The predicted change in temperature at the location of the fiber optic temperature probe was accurate within a single standard deviation at all voltages tested (Figure 8.5 b). The temperature change during treatment also increased non-linearly with the applied voltage. The inclusion of the actual metal electrodes and polystyrene plate was required to dissipate the heat and match experimental temperatures using a reasonable heat transfer coefficient for free convection with air of 25 (W m^{-2} K^{-1}) (Chapman, 1987).

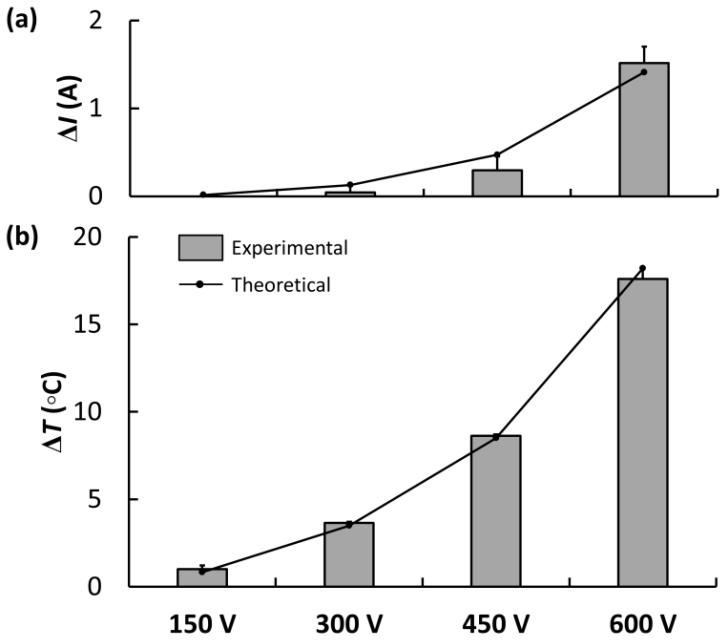

Figure 8.5. Comparison of experimental and numerical results. Change in current (a) and temperature (b) delivered through the *in vitro* tumors during IRE performed at 150 V, 300 V, 450 V, and 600 V. The treatment consisted of 80, 100 µs long pulses delivered once per second. The bars with one standard deviation indicate the experimentally measured values. The data points along the line illustrate the results of the numerical model, which was optimized to match the measured change in current and temperature from the onset to offset of pulsing.

8.3.4 – Determination of Transient Current and Temperature Development

Representative surface plots of the predicted electric field, temperature, and electrical conductivity distributions for an applied voltage of 300 V are shown in Figure 8.6. The maximum temperature at the end of treatment occurred at the center of the domain. For all simulated voltages, the maximum temperature was calculated to be 23°C, 27°C, 35°C, and 51°C for an applied voltage of 150 V, 300 V, 450 V, and 600 V, respectively, with the baseline set at 22°C. Experimentally, an applied voltage of 600 V resulted in the formation of a void at the center of the *in vitro* tumors, presumably due to collagen denaturation (data not shown) (Bozec et al., 2011). By comparing the dimensions of the void with the temperature distribution, it was conservatively estimated that temperatures above 45°C should be avoided in future experiments on this *in vitro* platform.

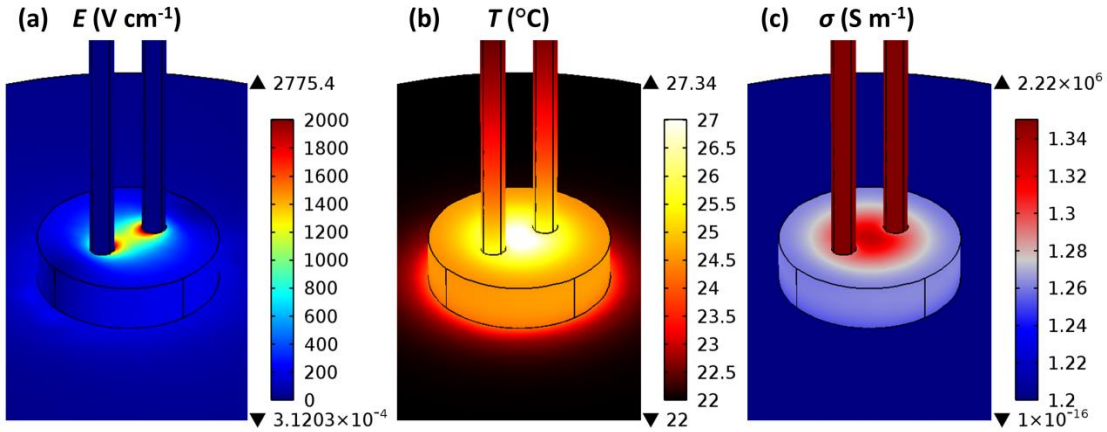

Figure 8.6. Surface plots from the numerical model of the *in vitro* tumor. (a) Electric field distribution, (b) temperature distribution, and (c) conductivity distribution at the end of an 80 s IRE treatment at 300 V. The upper and lower triangles along the scale bars indicate maximum and minimum values present within the entire domain, respectively. In the case of part (c) these values are consistent with those reported in Table 1 for the electrode and plate domains. Regions experiencing values outside the given color range (e.g., electrode and plate conductivity) assume the color associated with the limits of the displayed data.

Due to the inclusion of a temperature dependent electrical conductivity, the maximum conductivity at the end of treatment also occurred at the center of the domain. For all simulated voltages, the maximum conductivity was calculated to be 1.2 S/m, 1.3 S/m, 1.5 S/m, and 1.9 S/m for an applied voltage of 150 V, 300 V, 450 V, and 600 V, respectively, with the baseline set at 1.2 S/m. Even at the highest voltages, the noticeable increase in conductivity had an insignificant effect on the electric field distribution in the current experimental setup. For example, between the onset and offset of pulsing, the area of the top surface of the *in vitro* tumors exposed to an electric field above 500 V/cm changed by 0.01 mm^2, 0.02 mm^2, 0.09 mm^2, and 0.4 mm^2 for an applied voltage of 150 V, 300 V, 450 V, and 600 V, respectively. This correlates with a slight change in the dimensions of the 500 V/cm electric field contour from the onset to offset of pulsing. However, even at 600 V, the height of the area encompassed by the contour (y – direction) changed by only 0.08 mm, and the width (x – direction) changed by only 0.04 mm. All of these variations are within one standard deviation of experimentally measured values (Table 8.3).

8.3.5 – Determination of IRE Threshold for Cell Death in In Vitro Tumors

Only applied voltages of 300 V and 450 V were used to determine the electric field threshold for cell death (Table 8.3). As mentioned, an applied voltage of 150 V did not produce a complete lesion extending past the lateral surfaces of the electrodes or completely connecting in the center (Figure 8.2), which eliminated the possibility for accurate width measurements. At 600 V, void formation at the center of the *in vitro* tumors, presumably due to collagen denaturation, also eliminated the possibility for accurate measurements. There was a close agreement in the electric field threshold for cell death as determined by both the 300 V and 450 V treatment groups. In the 300 V group, averaging the electric field threshold as determined by each separate measurement resulted in a threshold of 497 V/cm. Similarly, in the 450 V group, the average threshold from each measurement was 490 V/cm. Between the groups, the highest variability was present within thresholds determined from width measurements. This is likely due to the difficulty in measuring lesion width near the electrodes and the steep gradient in electric potential near the lateral electrode surfaces. If width measurements were omitted from the analysis, the electric field threshold for cell death became 496 V/cm and 500 V/cm for the 300 V and 450 V groups, respectively.

Table 8.3. Treatment dimensions and IRE threshold for cell death

Voltage (V)	Conc. (cells ml^{-1})	Area (mm^2)	Height (mm)	Width (mm)	E_T (Area, Height, and Width) ($V\ cm^{-1}$)
300 (n = 3)	5×10^6	16.28 +/- 2.73	4.02 +/- 0.40	4.91 +/- 0.34	491, 501, 500
450 (n = 3)	5×10^6	25.80 +/- 1.48	5.83 +/- 0.40	5.58 +/- 0.13	498, 502, 470

Overlaying the 500 V/cm contour on the live/dead stained images of the *in vitro* tumors from each of these groups illustrates the accuracy of the numerical model for determining the electric field threshold for cell death (Figure 8.7). While no data is present in the literature on the

threshold in pancreatic tumors, our result is comparable to that obtained *in vivo* for brain tissue (Garcia et al., 2010) when a similar pulsing protocol was implemented. Results citing a higher threshold of 637 V/cm *in vivo* for liver tissue were likely due to a ten-fold reduction in the number of pulses delivered (Miklavcic et al., 2000), and this effect could be elucidated in future experiments.

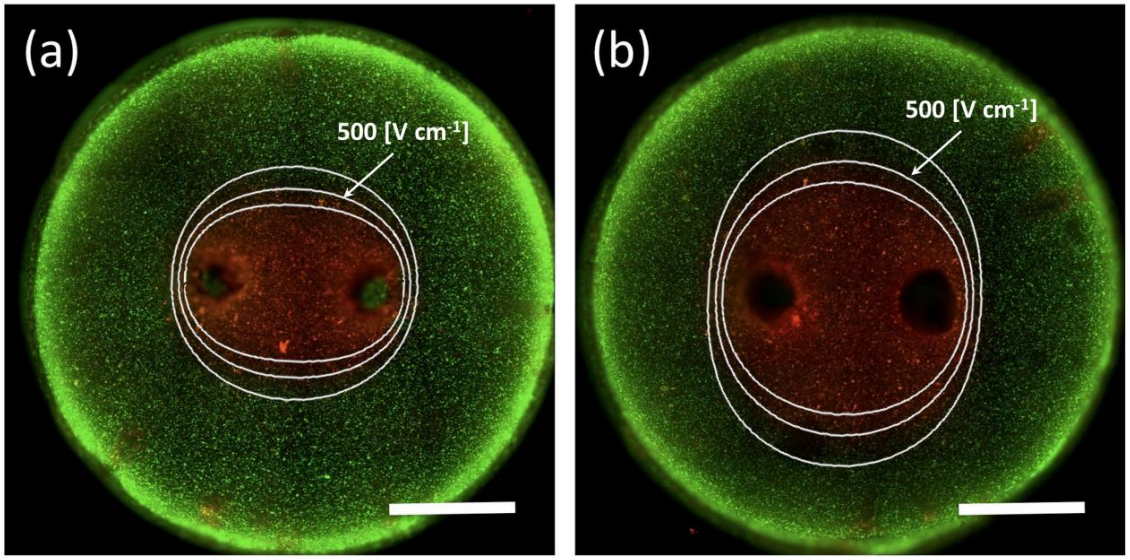

Figure 8.7. Overlay of electric field contours predicted by the numerical model. Values were taken at the end of an 80 s IRE treatment at (a) 300 V and (b) 450 V with the corresponding live/dead tiled images from Figure 8.2. The field contours shown are at 400 V/cm (inner), 500 V/cm (middle), and 600 V/cm (outer). The contour labeled 500 V/cm denotes the threshold for cell death. Scale bars represent 2.5mm.

8.3.6 – Determination of IRE Threshold for Cell Death in Suspension

It is difficult to determine a distinct electric field threshold for cell death from the viability analysis on cell suspensions. In the past, conservative estimates have been made under the assumption that the threshold *in vivo* corresponds to the value of the electric field resulting in less than 5 % viability in suspension (R. E. Neal et al., 2009). Under the same logic, our results suggest that a conservative estimate of the electric field threshold for cell death *in vivo* would be around 1500 V/cm (Figure 8.8). Additionally, at 500 V/cm there was no corresponding reduction of cell viability in suspension. Similar results have been shown for the onset of reversible

electroporation, which was found to occur at a significantly lower electric field strength *in vivo* compared to the same cells in suspension (Belehradek et al., 1994).

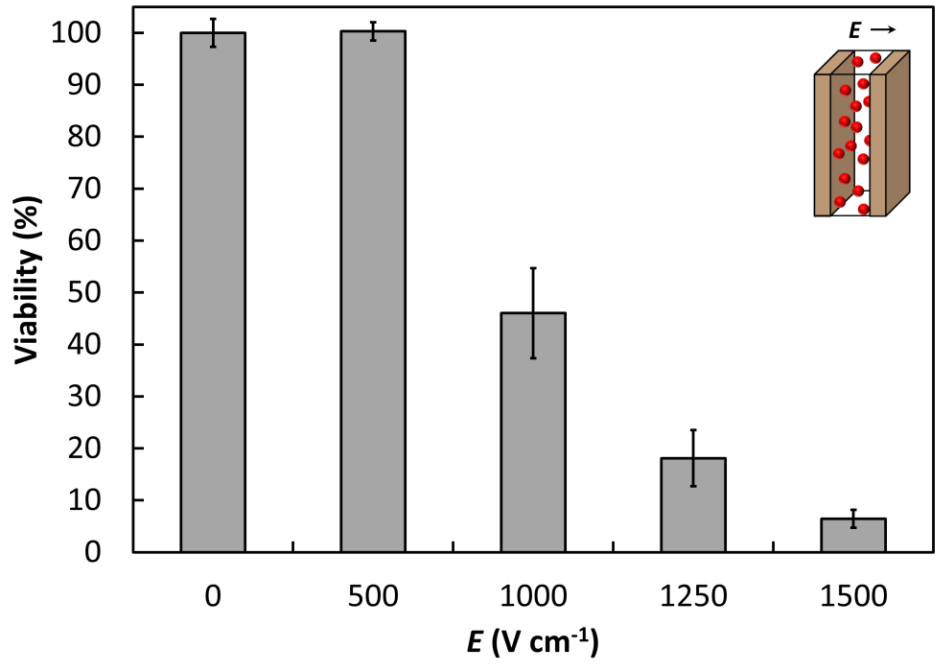

Figure 8.8. Percent viability following IRE of PPT-8182 cells in suspension. The applied electric field ranged from 0 V/cm to 1500 V/cm. At the field threshold for cell death determined from the *in vitro* tumors (500 V/cm), there was no significant reduction in cell viability determined from suspension experiments performed in cuvettes. The results were normalized to the raw percent viability for the sham group (95 %).

8.3.7 – Determination of H-FIRE Threshold for Cell Death in In Vitro Tumors

As the frequency of the H-FIRE waveform was increased, a greater electric field strength was required to induce cell death (Table 8.4). Contiguous lesions of decreasing height were seen as the frequency was increased from 10 kHz to 250 kHz (data not shown). The 2 MHz waveform did not produce a complete lesion extending past the lateral surfaces of the electrodes or completely connecting in the center. The field threshold in this case was estimated by computing distance measurements from the medial surface of the electrodes towards the center of the domain and drawing similar comparisons to the numerical model.

Table 8.4. Treatment dimensions and H-FIRE threshold for cell death

Frequency (kHz)/Duration of single polarity (μs)	E_T (Height) (V cm^{-1})
2000/0.25	2500
250/2	1000
100/5	900
10/50	675

8.4 – Discussion

Cancer cells cultured in 3D collagen I hydrogels were shown to respond to IRE pulse delivery comparable to published *in vivo* results. This included a similar electric field threshold for cell death (Table 8.3) (Garcia et al., 2010), sparing of the underlying collagen network (Onik et al., 2007), and sub-millimeter resolution at the boundary between treated and untreated regions (Figure 8.3) (J. F. Edd et al., 2006; Onik et al., 2007). H-FIRE results showed similar features, however, quantitative *in vivo* data for direct comparison of electric field thresholds is currently unavailable. Recently, collagen I hydrogels have been used to study reversible electroporation and electrogene transfer (Haberl et al., 2010). In this study conducted by Haberl and Pavlin, it was found that electrogene transfer had a similar dependency on plasmid concentration and pulse duration to that seen *in vivo* when performed in a 3D *in vitro* environment. Further, transfection was more pronounced on the surface of the collagen I hydrogels, due to diffusion limitations through the collagen mesh, which is also a characteristic seen *in vivo* (Henshaw et al., 2008).

Compared to conventional *in vitro* IRE treatment planning models, such as cell suspensions and cell culture monolayers, the 3D *in vitro* tumor model generated more accurate predictability of IRE outcomes. This is likely due to the ability of the cells cultured in 3D to reproduce the cell-cell/cell-matrix interactions seen in the original tissue that are important for dictating an *in vivo*-like morphology. As a result of cell protrusions interacting with the collagen matrix, the cell diameters in the hydrogel are larger than when in suspension (13.1 μm). This

may contribute to the decreased electric field threshold for cell death, as a larger diameter increases the calculated TMP (Schwan, 1957):

$$\Delta\phi(\theta) = \frac{3}{2} Ea\cos\theta \qquad (6)$$

where *a* the radius of the cell and θ is the polar angle measured from the center of the cell with respect to the direction of the electric field. The induced TMP creates a supraphysiologic electric field in the membrane that is thought to be responsible for permeabilization. For a membrane thickness of 5 nm, an external electric field of 500 V/cm applied across a cell in suspension ($\Delta\phi_{max}$ = 0.98 V) generates a voltage-to-distance ratio on the order of ~2 MV/cm within the membrane. In cell monolayers, 2D spatial information and limited cell-cell/cell-matrix interactions can be obtained, but the path taken by electrical current is significantly altered when compared to a 3D environment (a majority of current flows through the culture media over the top of cells that are adhered to a highly insulative surface), which may alter the TMP and electric field threshold for cell death. Furthermore, analysis of dead cells is complicated by the fact that they can detach from the culture surface.

Current measurements were unable to detect any dynamic change in bulk electrical conductivity due to electroporation for *in vitro* tumors consisting of 5×10^6 cells/ml. Specifically, at an applied voltage of 300 V, there was no statistical difference in the change in current between the first and last pulse when comparing the 5×10^6 cells/ml group to the no cells control group. Therefore, any dynamic changes in bulk tissue electrical conductivity due to electroporation that have been reported *in vivo* could be neglected from the numerical model of the *in vitro* tumor. This greatly reduced the number of parameters contributing to an accurate determination of the electric field threshold for cell death.

When the cell concentration was increased to 50×10^6 cells/ml, there was a significant decrease in the measured current during treatment at 300 V compared to the no cells control and 5×10^6 cells/ml groups (data not shown). This is unlike what happens *in vivo*, and may be the result of the fact that the cytoplasm has a lower electrical conductivity than the extracellular space (Mezeme et al., 2012). Upon electroporation, the release of cytosol into the extracellular space may dominate the bulk electrical properties at this specific cell concentration. At higher cell concentrations in tissue, the bulk electrical properties during electroporation are dominated by the creation of membrane defects, which greatly increase the conductivity and resulting current during treatment. According to the EMT model, a cell concentration on the order of 340×10^6 cells/ml would be required to cut the baseline conductivity of the *in vitro* tumors in half, from 1.2 S/m to 0.6 S/m, which is more electrically relevant to tissue and corresponds to a volume fraction of 0.4. Due to diffusion limitations through the collagen hydrogel, obtaining such high concentrations while maintaining cell viability is a challenging task. This will be the subject of future work directed towards replicating the dynamic conductivity changes seen *in vivo* on a 3D *in vitro* platform.

A current limitation of the relatively high electrical conductivity of the *in vitro* tumors compared to an *in vivo* environment is the added heat generated during treatment. As a result, select protocols that do not cause significant thermal damage *in vivo* may be unsuitable for testing *in vitro* due to collagen I denaturation. Similar concerns are present when treating cells in suspension. For the range of applicable pulse parameters tested here, thermal changes had a minimal influence on the electric field distribution. This may be attributed to the small size of the *in vitro* tumor domain relative to the electrode spacing, which causes the entire tumor to experience both an elevated temperature and conductivity. In the future, the hydrogel volume

could be increased to mimic a clinical scenario, in which the electrodes are inserted into a targeted tumor and the treatment region varies in all directions. Here, the experimental setup was designed to induce a region of cell death that was symmetric in the *z*-direction (Figure 8.3).

8.5 – Conclusion

Performing IRE and H-FIRE on a 3D *in vitro* tumor platform produced an electric field dependence on cell death characteristic of an *in vivo* response. Thus, this model is suitable for generating a wide range of data that will be useful in refining treatment planning algorithms used in non-thermal ablation procedures. Specifically, studies correlating varying pulse parameters to ablation volume in a variety of cancer cell lines will help identify both protocol-specific and cell-specific parameters to enhance the reliability of predicted outcomes. Additionally, there is the possibility of growing patient-specific *in vitro* tumors from biopsied tissue. Further development of this platform will facilitate the acceptance of IRE as a viable cancer therapy.

9 – Theoretical Investigation of Latent Heat Storage Electrodes for High-Dose IRE[4]

9.1 – Introduction

To capitalize on the benefits of non-thermal ablation, energy delivery is limited to levels that minimize the potential for thermal damage. This restricts the range of applicable parameters to approximately 100 total pulses delivered at a rate of 1 Hz, amplitude of 1000 to 2000 V/cm, and duration of 50 to 100 µs. When large lesions are desired and protocols are selected towards the upper end of this parameter space, there exists a narrow region of tissue adjacent to electrode edges that has a high probability of experiencing thermal damage (Appelbaum et al., 2012; Ben-David et al., 2012). This is also true in the case of H-FIRE, where higher electric fields are required to induce cell death. We hypothesize that by incorporating phase change materials (PCMs) into the design of electrodes, the peak tissue temperature reached during IRE and H-FIRE therapy will be reduced. Due to their high latent heat of fusion, PCMs absorb heat from their environment during the solid (*s*) – liquid (*l*) transition. This effectively slows the rate of temperature increase. Therefore, these electrodes have the capacity to treat large volumes without any added potential for thermal damage. Here, we model this phenomenon using a numerical implementation of the effective heat capacity method in combination with a model for IRE in liver tissue. Results indicate that the inclusion of a PCM, which melts during treatment, can in fact moderate temperature development within the tissue.

9.2 – Methods

A 3D finite element model was developed using COMSOL for calculating the electric field and temperature distributions throughout an IRE procedure performed with needle

[4] Chapter 9 is adapted and reprinted with permission. © 2012 American Institute of Physics. Arena, C. B., Roop, M. L., Rylander, M. N., and Davalos R. V., Towards the Development of Latent Heat Storage Electrodes for Electroporation-Based Therapies, Applied Physics Letters, 101(8), 083902, Aug 2012.

electrodes (Figure 9.1). The core material was varied between a salt hydrate PCM that melts at 40°C (Sharma et al., 2009) (disodium hydrogen phosphate dodecahydrate) and a solid metal equivalent to the electrode shell. A salt hydrate PCM was chosen as this material class has a relatively high thermal conductivity and latent heat of fusion per unit volume compared to organic PCMs (Demirbas, 2006; Sharma et al., 2009), which facilitates a rapid phase change with maximum heat absorption. Additionally, many salt hydrates exist with melting points slightly above body temperature. This ensures that the phase transition and subsequent heat absorption begins near the onset of the pulsing sequence.

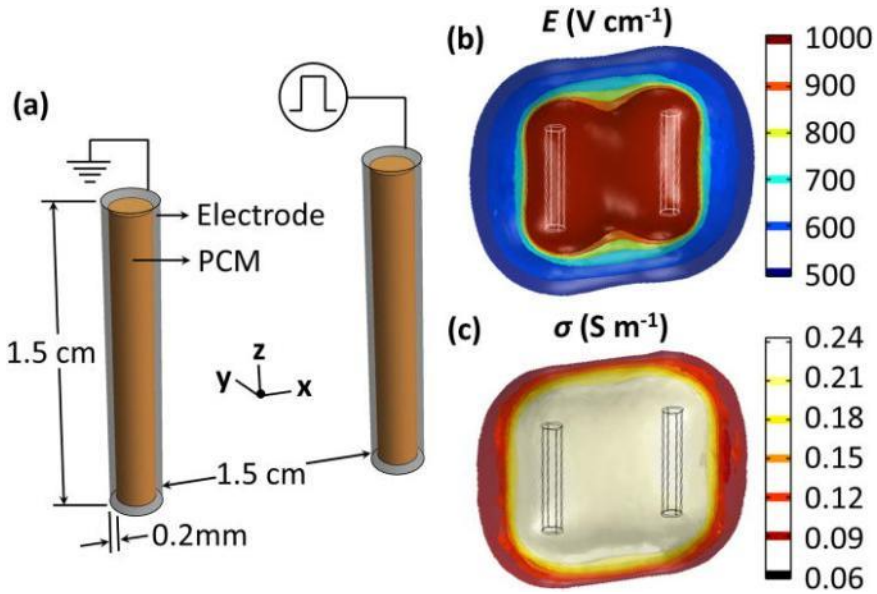

Figure 9.1. Illustration of PCM electrode design. (a) Schematic diagram of the geometry under consideration with PCM core electrodes used to perform IRE of liver tissue. (b) Electric field distribution resulting from the application of 3000 V to the energized electrode. (c) Electric conductivity distribution resulting from the application of 3000 V to the energized electrode. A non-linear increase in bulk electric conductivity occurs in regions of liver tissue subject to a critical electric field for inducing electroporation. The electrode radius illustrated here is 1.5 mm.

In the effective heat capacity method, the $s - l$ transition is accounted for by including the latent heat of fusion, λ (265.6 kJ kg^{-1}) (Hirano et al., 2000) in the volume average of the specific heat capacity at constant pressure:

$$c_{p,eq} = \Theta\left(c_{p,s} + \lambda\Pi\right) + (1 - \Theta)(c_{p,l} + \lambda\Pi) \quad (1)$$

where Θ is the volume fraction of solid material defined by *1 – flc2hs((T-T_T),R_T)*, and T_T is the transition temperature (40°C) (Sharma et al., 2009) over the transition range, R_T (1°C). This approximates the logical step Θ = 1 for $T < T_T$ and Θ = 0 for $T > T_T$ by smoothing the transition within the interval $T_T - R_T < T < T_T + R_T$ using a continuous second derivative. Similarly, the term Π is a normalized pulse around the transition temperature defined by *∂(flc2hs((T-T_T),R_T))/∂T*. Smoothing is required for the solver to handle step changes (Dantzig, 1989; Krishnan et al., 2004). In the PCM domain, the temperature, *T*, distribution was solved using a modified heat conduction equation, which includes Joule heating, Q_J, due to the application of PEFs:

$$\rho_{eq} c_{p,eq} \frac{\partial T}{\partial t} = \nabla \cdot \left(k_{eq} \nabla T\right) + Q_J \qquad (2)$$

where ρ_{eq} and k_{eq} are volume averages of the density and thermal conductivity, respectively (Table 9.1):

$$\rho_{eq} = \Theta\rho_s + (1 - \Theta)\rho_l \quad \text{and} \quad k_{eq} = \Theta k_s + (1 - \Theta)k_l \qquad (3,4)$$

Table 9.1. PCM properties

Property	Value	Ref.
k (W m^{-1} K^{-1}) (*s*/*l*)	1.0/0.6	(Hirano et al., 2000)
c_p (J kg^{-1} K^{-1}) (*s*/*l*)	1960/3430	(Hirano et al., 2000)
ρ (kg m^{-3}) (*s*/*l*)	1520/1450	(Hirano et al., 2000)
σ (S m^{-1})	1	-

The electrode shell was modeled as stainless steel (AISI 4340) according to the COMSOL material library without any *s – l* transition. In the tissue domain, additional terms accounting for blood perfusion, ω_b, and metabolic heat generation, Q_m, were included in the formulation (Table 9.2):

$$\rho c_p \frac{\partial T}{\partial t} = \nabla \cdot (k\nabla T) + \rho_b w_b c_b (T_b - T) + Q_m + Q_J \quad (5)$$

The Joule heating term:

$$Q_J = \sigma |E|^2 \quad (6)$$

was obtained by first solving for the electric field, *E*, distribution in the tissue under the electro-quasistatic approximation:

$$-\nabla \cdot (\sigma(|E|)\nabla\Phi = 0) \quad (7)$$

where Φ is the electric potential and $\sigma(|E|)$ is the dynamic electric conductivity. Equation 7 is valid on the basis that the duration of a constant voltage IRE pulse greatly outweighs the pulse rise/fall time and lends itself to a steady-state approximation. The dynamic electric conductivity function describes how the tissue conductivity changes with electric field due to electroporation. It was constructed by approximating data on electroporation of liver tissue (Sel et al., 2005) with a smoothed step function $\sigma_o(1+2.597\times flc2hs((E-T_E),R_E))$, where T_E (650 V/cm) is the location of electric field transition over the range, R_E (150 V/cm). In the electrode and PCM domains, no conductivity dependence on electric field was included in Eq. 7.

Table 9.2. Tissue properties

Property	Value	Ref.
k (W m^{-1} K^{-1})	0.502	(I. A. Chang et al., 2004)
c_p (J kg^{-1} K^{-1})	3600	(I. A. Chang et al., 2004)
ρ (kg m^{-3})	1060	(I. A. Chang et al., 2004)
ω_b (1 s^{-1})	0.0064	(I. A. Chang et al., 2004)
c_b (J kg^{-1} K^{-1})	4180	(I. A. Chang et al., 2004)
ρ_b (kg m^{-3})	1000	(I. A. Chang et al., 2004)
Q_m (W m^{-3})	33800	(Keangin et al., 2011)
σ_o (S m^{-1})	0.067	(Sel et al., 2005)

Electric potential boundary conditions of 3000 V and 0 V were applied along the outer surfaces of the energized and grounded electrode shells, respectively, and the initial tissue

temperature and blood temperature was set to 37°C. All remaining inner boundaries were treated as continuity, and the outer boundaries were treated as electrically and thermally insulating. The tissue was modeled as a cube (10 cm), and the electrode edge-to-edge spacing (1.5 cm) and height (1.5 cm) were held constant.

A parametric study was performed on electrode radius (0.5 mm to 1.5 mm) in order to investigate a range of electrode sizes that could mitigate temperature increase. A finer, free tetrahedral mesh was used, which resulted in between 145,495 and 188,916 elements, depending on the electrode radius under investigation, and less than 0.1% difference in temperature calculations at the electrode-tissue interface upon successive refinements. Additionally, strict time stepping at 1 s intervals was implemented, as the solver could take additional time steps if necessary to accurately resolve the phase transition. The time of pulsing was 70 s, and the Joule heating term was scaled by the duty cycle (90×10^{-6}) in order to simulate the delivery of 90 µs long pulses at a repetition rate of 1 Hz. This protocol was chosen based on experimental evidence of thermal damage surrounding solid metal electrodes (Appelbaum et al., 2012; Ben-David et al., 2012).

9.3 – Results and Discussion

The stationary electric field distribution and electric conductivity distribution are shown in Figure 9.1 for an electrode radius of 1.5 mm. These results are independent of the electrode core material, as the electric field is zero in those regions. According to the dynamic conductivity function, any tissue exposed to an electric field greater than 700 V/cm is subject to undergo IRE, and any tissue exposed to an electric field greater than 800 V/cm reaches a plateau in conductivity of 0.241 S/m.

The time-course of PCM melting is shown in Figure 9.2. Due to symmetry, only a single electrode from the pair is shown at each time step. The *s* – *l* transition time depends on the PCM volume and electrode radius. Transition time increases as electrode radius increases, due to the greater volume of PCM that must surpass the melting temperature. For an electrode with a 1 mm radius, the phase transition is complete after 55 s. The center portions of the electrodes are the last to melt. As mentioned, the electric field is zero within the electrode core. Therefore, heat is transferred from the surrounding tissue through the electrode shell. Due to the sharp edges at the top and bottom of the electrodes, the electric field is highest in these regions. As a result, the PCM melts preferentially at the top and bottom of the electrodes.

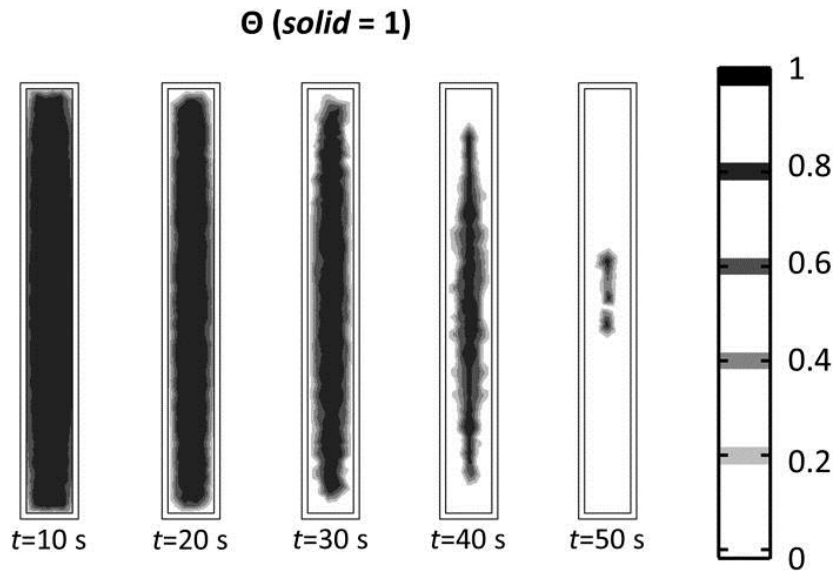

Figure 9.2. Time-lapse of the solid-to-liquid transition. For an electrode with a radius of 1.0 mm, the PCM melting process is complete after 55 s. The transition times for the electrode radii not shown (0.5 mm, 0.75 mm, 1.25 mm, and 1.5 mm) are 13 s, 33 s, 76 s, and 104 s, respectively.

Incorporating PCMs into electrode designs can limit the peak temperature reached during IRE therapy. The effect is highly dependent upon the PCM transition time and the time of pulsing. Figure 9.3 shows a plot of temperature versus time at a point at the center of the electrode-tissue interface for a solid metal electrode (Figure 9.3 a) and a PCM core electrode (Figure 9.3 b) of varying radius. In the case of the solid metal electrode, temperature increases

sharply during treatment. Additionally, as the radius increases, the maximum temperature reached during treatment decreases. This is due to a decrease in the electric potential gradient surrounding the electrode with increasing radius. In the case of the PCM core electrode, there is a minimal increase in temperature during the phase transition. However, once the PCM is completely melted, the temperature increases at a faster rate and approaches the temperature of the solid metal electrode. For the 70 pulse protocol, a PCM core electrode with a radius greater than or equal to 1.25 mm ensures that the phase transition is not complete by the end of treatment. As a result, the peak temperature at the electrode-tissue interface is well below the level for accelerated thermal damage (taken here to be 50°C (R. V. Davalos et al., 2003)). The results are also dependent upon the applied voltage. Lowering the applied voltage from 3000 V extends the transition time for a given electrode radius due to a reduced heating rate (data not shown).

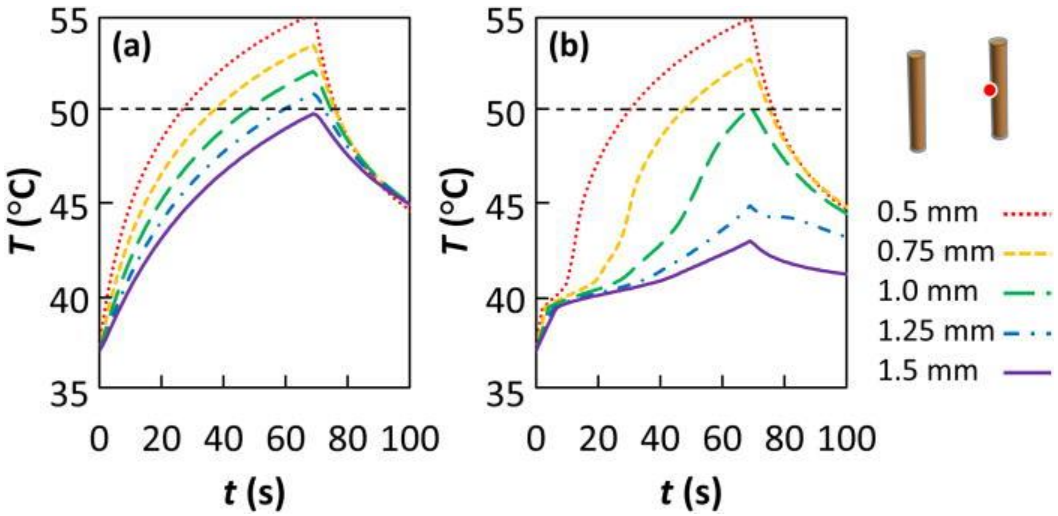

Figure 9.3. Temperature development versus time. Values were taken at the center point along the electrode-tissue interface (0.75 cm, 0, 0) for a solid metal electrode (a) and PCM core electrode (b). The IRE treatment consists of 70, 90 µs long pulses applied at a frequency of 1 Hz and voltage-to-distance ratio of 2000 V/cm. The dashed line at 50°C indicates a threshold for a dramatic increase in the rate of thermal damage.

During the phase transition, the presence of the PCM has the greatest influence on temperatures within and adjacent to the electrodes. Figure 9.4 shows the temperature distribution

at the end of treatment along a cut line through the center of solid metal electrodes (Figure 9.4 a) and PCM core electrodes (Figure 9.4 b) of varying radius. Between the electrodes, the temperature is also reduced, albeit to a lesser degree.

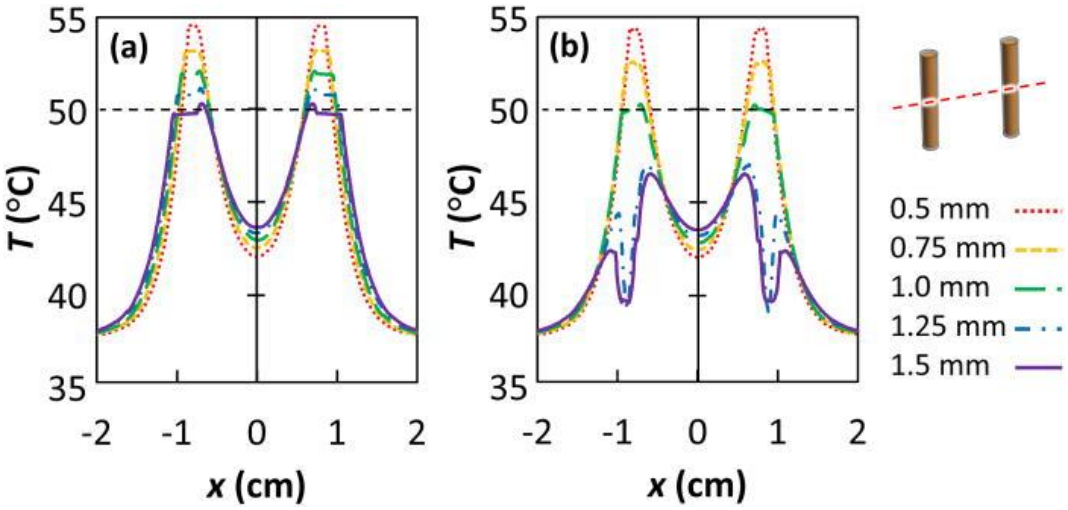

Figure 9.4. Temperature cross-section. Values were taken at the end of treatment (t = 70 s) through the center of solid metal electrodes (a) and PCM core electrodes (b). The IRE treatment consists of 70, 90 µs long pulses applied at a frequency of 1 Hz and voltage-to-distance ratio of 2000 V/cm. The dashed line at 50°C indicates a threshold for a dramatic increase in the rate of thermal damage.

Based on the temperature profiles shown in Figure 9.3, the extent of thermal damage at the electrode-tissue interface was quantified using the Arrhenius equation:

$$\Omega(t) = \int \zeta e^{-E_a/(R\,T(t))} dt \qquad (8)$$

where $\Omega(t)$ is the damage integral, ζ is the frequency factor, E_a is the activation energy, R is the universal gas constant, and $T(t)$ is the temperature at a given time, t. These parameters have been defined for protein coagulation in the liver (E_a = 2.577×10^5 J mol^{-1}; ζ = 7.39×10^{39} s^{-1}) (I. A. Chang et al., 2004), where Ω = 1 empirically marks tissue whitening (Beop-Min et al., 1996). Equation 8 was solved in Wolfram Mathematica 8.0 (Champaign, IL, USA) until the 200 s time point (130 s after the offset of pulsing). For the prescribed treatment, the results indicate that the PCM core reduces the probability of thermal damage in all cases (Table 9.3). The PCM core also

has the potential to eliminate tissue whitening seen in IRE with solid metal cores (Appelbaum et al., 2012; Ben-David et al., 2012) if the electrode radius is greater than or equal to 1.0 mm. While larger electrodes are beneficial in terms of reducing thermal damage, they are also associated with increased invasiveness. However, a 1.0 mm radius is typical of liver biopsy needles (Littlewood et al., 1982).

Table 9.3. Damage integral, Ω

Radius (mm)	Solid metal core	PCM core
0.50	2.58	2.33
0.75	1.73	1.25
1.00	1.26	0.62
1.25	0.99	0.30
1.50	0.80	0.21

This feasibility study was designed to isolate the effect of the $s - l$ transition. To simplify the initial analysis, we have neglected the influence of temperature on electric conductivity. This will likely effect the transition time and be required for experimental validation. Additionally, the dynamic electric conductivity function was modeled after data from rabbit liver, and it will be useful to investigate the influence of other species and organ types on the transition time. Electrodes were approximated as cylindrical shells within a tissue domain large enough to avoid boundary effects. Future work should include the influence of fins and convective cooling along with alternate electrode designs. For instance, plate electrodes used for transdermal applications of electroporation may also benefit from the incorporation of PCMs. The skin is highly resistive and often subject to temperatures above the threshold for thermal damage when exposed to PEFs (Becker et al., 2007). An added benefit of plate electrodes is that they are placed externally on the surface of the tissue, and their dimensions can be increased if needed to optimize the PCM transition time without increasing electrode invasiveness.

Alternative methods for reducing thermal damage at the electrode-tissue interface have been proposed. For example, electrodes can be aggressively pre-cooled prior to applying the pulses (Becker et al., 2007). However, this requires modifications to surgical procedures and may be difficult to perform with needle electrodes where electrode placement requires extended periods of time, during which the electrodes can equilibrate with their surrounding environment. Active cooling throughout treatment has also been suggested but requires external equipment.

9.4 – Conclusion

PCMs have been widely used for managing temperature changes in electronics and industrial applications (Abhat, 1983; Khudhair et al., 2004; Krishnan et al., 2004; Zalba et al., 2003). Here, we show that they may also have unique benefits when applied to electrode designs for electroporation-based therapies. Specifically, electrodes containing a salt hydrate that transitions from solid-to-liquid during treatment can reduce the peak tissue temperature. This warrants further investigations into alternative materials, including biocompatible PCMs, and electrode designs in order to maximize the reduction in thermal damage for a desired set of pulse parameters.

10 – Experimental Investigation of Latent Heat Storage Electrodes for High-Dose IRE

10.1 – Introduction

In Chapter 9, we theoretically showed that phase change materials (PCM) could be incorporated into electrode designs to reduce the probability for thermal damage adjacent to electrode boundaries during large IRE ablations of the liver (Arena, Mahajan, et al., 2012). The specific PCM studied was disodium hydrogen phosphate dodecahydrate, which is a salt hydrate that stores a large amount of latent heat upon melting during treatment, narrowly above physiologic temperature. Up to this point, PCMs have been primarily used in the biomedical field in storage devices to protect temperature sensitive substances during transport (Mondieig et al., 2003), in clothing to protect the human body from extreme temperatures (Shim et al., 2001), and in contrast agents for image enhancement (Sheeran et al., 2012). Outside the biomedical field, they are slowly becoming commonplace in industrial applications of thermal protection of electronic devices (Ge et al., 2012; Marongiu et al., 1997), green energy storage (Prakash et al., 1985), and vehicle and building temperature regulation (Benard et al., 1985).

Here, we expand upon our previous theoretical results by experimentally investigating the use of PCMs in electroporation devices. Electrodes were fabricated with a metallic PCM core and pulses were applied to ultrasound gel, which served as a tissue phantom (Etheridge et al., 2013). For comparison, solid metal electrodes were also fabricated and tested. Temperature was monitored in real-time, and numerical models were constructed to match the data generated for each electrode type. Finally, a parametric study was conducted on the experimentally validated models to elucidate the effect of varying electrode radius, PCM melting point, and PCM thermal conductivity on temperature mitigation.

10.2 – Methods

10.2.1 – Experimental Setup

To fabricate the PCM electrodes, round brass tubing (4.0 mm diameter, 0.4 mm thickness, K&S Precision Metals, Chicago, IL, USA) was machined to length (2.46 cm), and high voltage wire was soldered to one end (22 AWG, Daburn, Dover, NJ, USA) to simultaneously plug the tubing and form connections to the pulse generator (ECM 830, BTX Harvard Apparatus, Holliston, MA, USA). Then, solid gallium (99.99% pure, GalliumSouce, Scotts Valley, CA, USA) was liquefied above its melting point (29.8°C) (Wagner et al., 1952) in deionized water and injected into the remaining open end of the hollow tubing. The gallium was allowed to re-solidify in the electrode core at room temperature. Solid metal electrodes were fabricated in a similar process using brass rods of equivalent dimensions.

Electrodes were spaced 0.43 cm edge-to-edge by drilling holes into a printed circuit board. The printed circuit board also provided a convenient port for a fiber optic temperature probe (Luxtron m3300, LumaSense, Santa Clara, CA, USA), which was located -2.0 mm in the *x*- and *y*-direction relative to the center of the leftmost electrode. Real-time temperature measurements were taken every 0.25 s to validate the numerical model described below. The entire setup was placed on the surface of a 100 ml glass beaker that was filled with ultrasound transmission gel (Mojility agent, MOtion1, Nashville, TN, USA), such that the electrodes extended -1.93 cm into the ultrasound gel in the *z*-direction. The height (7.05 cm) and diameter (5.03 cm) of the beaker were large enough to avoid edge effects. Ethridge *et al.* have characterized the thermal properties of ultrasound gel (Table 10.1) and, in the process, shown that it is a viable tissue phantom material (Etheridge et al., 2013). The phosphorescent sensor at the end of the temperature probe extended -1.80 cm in the *z*-direction from the surface of the

ultrasound gel. All experiments were conducted inside an incubator (Figure 10.1 a) set to 25°C. This ensured that temperatures reached during treatment surpassed the melting point of gallium.

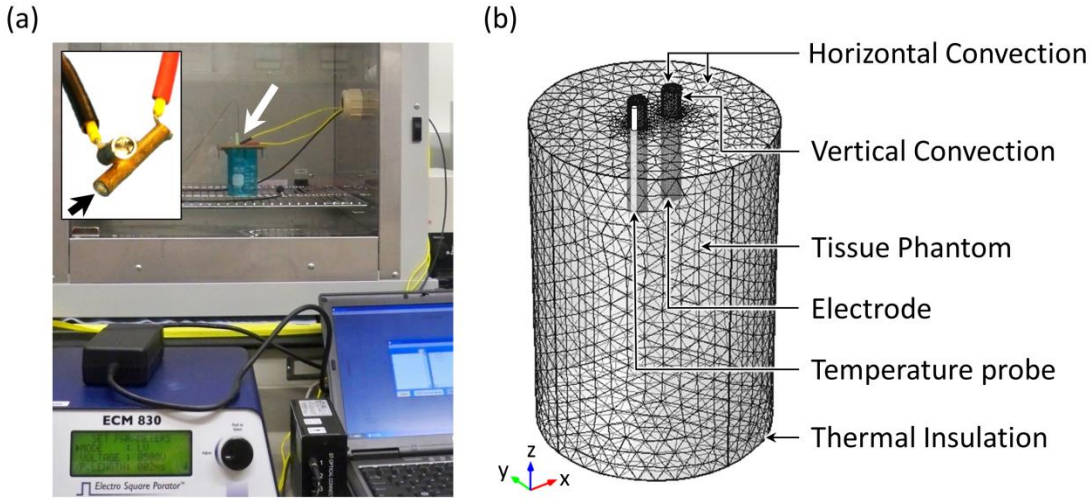

Figure 10.1. PCM electrode experimental overview. (a) Image of the experimental setup used to monitor temperature during electroporation with phase change electrodes. The electrodes and fiber optic temperature probe were spaced using a printed circuit board, inserted into the tissue phantom, and placed inside an incubator (white arrow). The insert shows the hollow brass electrodes with the inclusion of a gallium core (black arrow). (b) Representative mesh of the finite element model used to simulate the electroporation protocol.

The pulse protocol consisted of 99, 2 ms pulses delivered at a rate of 1 pulse per second. The applied voltage was set to 500 V, which was the maximum voltage at which the pulse generator could operate in low voltage mode. This produced a higher quality rectangular waveform and lowered the likelihood of arcing in the ultrasound gel. At this voltage-to-distance ratio the relatively long 2 ms pulses that are characteristic of EGT procedures were required to generate temperatures capable of initiating the gallium phase transition. A total of six beakers filled with ultrasound gel were placed in the incubator 6 hr prior to treatment in order to allow time for equilibration with the surrounding environment. Treatments with the solid electrodes ($n = 3$) and PCM electrodes ($n = 3$) were conducted at random, and a 10 min delay period was included between trials to allow the electrodes to return to their baseline temperature.

10.2.2 – Simulation of the Experimental Setup

A 3D finite element model was developed using COMSOL Multiphysics 4.2a (Stockholm, Sweden) to simulate the electric field and temperature distributions throughout the experimental procedure (Figure 10.2 b). The core material of the electrodes was varied between the proposed gallium PCM and a solid metal equivalent to the brass shell (Table 10.1). The use of the glass beaker to contain the ultrasound gel was replaced with insulative boundary conditions to reduce the total number of mesh elements and speed computation time. Specifically, a finer, free tetrahedral mesh was used, which resulted in less than 0.5% difference in temperature calculations at the location of the fiber optic probe upon successive refinements. Replicating the 99 s experimental treatment (plus an additional 51 s to observe cooling) required approximately 20 min of computational time. This relatively long time is due to the small time step (0.05 s) and low tolerance (0.001 relative, 0.0001 absolute) that was chosen in order to accurately resolve the phase transition in the PCM electrodes without oscillations in the predicted temperature. All simulations were performed on a Dell Precision T3500 Workstation (3.20 GHz, 12 GB Ram).

To account for the solid (*s*) – liquid (*l*) phase transition in the PCM domain, the effective heat capacity method was implemented using an identical formulation to Chapter 9. The electrical conductivity of the ultrasound gel (Table 10.1) was measured at 25°C using a conductivity meter (B-173, Horiba, Kyoto, Japan). All other material properties are referenced from (Wagner et al., 1952)[*], (Deri et al., 2010)[†], and (Etheridge et al., 2013) [§]. The Joule heating term was scaled by the duty cycle (pulse duration/period between pulses = 2×10^{-3}) to ensure that the total energy deposition matched the experimental protocol (2 ms pulse once every second). Electric potential boundary conditions of 486 V (output average) and 0 V were applied along the

outer surfaces of the energized and grounded electrode shells, respectively, and the initial voltage was set to 0 V in all domains. Additionally, all outer boundaries were treated as electrically insulating ($-n \cdot J = 0$). In terms of the thermal initial and boundary conditions, the initial temperature, T_0, was set to 25.9°C (baseline average) in all domains and in the exterior surroundings, T_{ext}, and the bottom and vertical boundaries of the tissue phantom domain were set as insulation ($-n\cdot(-k\nabla T) = 0$). The upper surface of the tissue phantom and electrode domains were set as external natural convection from the upside of a horizontal plate, and the vertical surfaces of the electrode domains were set as external natural convection from a vertical wall ($-n\cdot(-k\nabla T) = h(T_{ext} - T)$). For each case, the heat transfer coefficient (h) was determined from:

$$h = \frac{k\,Nu}{L} \qquad (1)$$

where Nu is the Nusselt number and L is a characteristic length scale. The length scale for the vertical case is the height of the exposed electrode surface, and the length scale for each horizontal case is the respective ratio of area/perimeter. The Nusslet number for each case can be found in (Incropera et al., 1996), and all material properties are evaluated at $((T + T_{ext})/2)$.

Table 10.1. PCM, electrode, and phantom properties

Property	Gallium (*s*/*l*)	Brass	Ultrasound gel
k (W m^{-1} K^{-1})	40.6/28.1[†]	109	0.52[§]
c_p (J kg^{-1} K^{-1})	376.8/343.3[*]	377	3800[§]
ρ (kg m^{-3})	5904/6093[*]	8520	1020[§]
σ (S m^{-1})	3.7×10^{6}[*]	1.7×10^{7}	0.13

A parametric study was performed on the transition range of the gallium to optimize the fit with the experimental results. T_R was varied (0.05, 0.1, 0.5, 1, and 1.5°C), and an overall regression coefficient was determined according to (Etheridge et al., 2013):

$$R^2 = 1 - \frac{\sum_{t=0}^{150}(T_{exp} - T_{num})^2}{\sum_{t=0}^{150}(T_{exp} - \bar{T}_{exp})^2} \quad (2)$$

where T_{exp} and T_{num} are the experimental and numerical temperatures, respectively, for a given time at the location of the fiber optic probe, and $\overline{T}_{\exp}$ is the average experimental temperature for all times at the location of the fiber optic probe.

10.2.3 – Expansion of the Numerical Model

The experimentally validated model was expanded to investigate a clinical IRE scenario with varying electrode properties. A parametric study was performed on electrode radius (0.5 mm, 0.75 mm, 1.0 mm, and 1.25 mm) and PCM melting point (T_M - T_0 = 1°C, 4°C, 7°C, and 10°C). The range of applicable electrode radii spans from commercially available IRE probes (NanoKnife Single Electrode, AngioDynamics, Queensbury, NY, USA) at the lower end to biopsy needles at the upper end (Amin et al., 2011). While the variation in PCM melting point may seem idealized, it is physically possible to raise/lower the melting point of gallium through alloying processes (Predel, 1960). To maximize the volume of PCM inside the electrode core, the shell thickness was reduced to 0.25 mm, which is similar to certain hollow dispensing needles (Howard Electronic Instruments Inc., El Dorado, KS, USA). An IRE protocol reported in (Appelbaum et al., 2012) was chosen here to investigate whether PCMs could mitigate temperature increase during these type of large liver ablations. Specifically, the applied voltage was increased to 3000 V across a constant electrode spacing of 1.5 cm (center-to-center). The pulse duration and the total time of pulsing were reduced to 90 µs and 70 s, respectively, and the electrical conductivity of the ultrasound gel was maintained at 0.13 S/m, which matches that of liver tissue at 25°C (Antunes et al., 2012).

The parametric study on electrode radius and melting point was repeated for thermal conductivities one and two orders of magnitude lower than gallium in both the solid and liquid phases. This simulation was designed to conceptualize alternate classes of PCMs, including salt hydrates ($k_{eq}/10$) and organics ($k_{eq}/100$). All other thermal properties were held constant. This ensured an equivalent heat of fusion per unit volume and heat capacity per unit volume between all trials. Interestingly, varying the density, heat of fusion, and heat capacity does not affect the results as long as the products of heat of fusion with density and heat capacity with density remain unchanged (data not shown). Salt hydrates and organics with similar products to gallium are commercially available (Zalba et al., 2003).

10.3 – Results

A comparison between the experimentally measured temperatures and the numerically predicted temperatures is shown in Figure 10.2. The experimental data is presented as the average of n = 3 trials by the dotted lines, and sample standard deviations are given at 5 s intervals. In the case of the solid electrodes, the temperature at the location of the fiber optic probe increased over 11°C above the baseline during treatment. The temperature increase was limited to approximately 4°C in the case of the PCM electrodes, which is over a two-fold reduction in peak temperature when compared to the solid electrodes. Despite this significant reduction in temperature, the gallium core remained fixed within the brass shell, which suggests that the phase transition process is in its early stages.

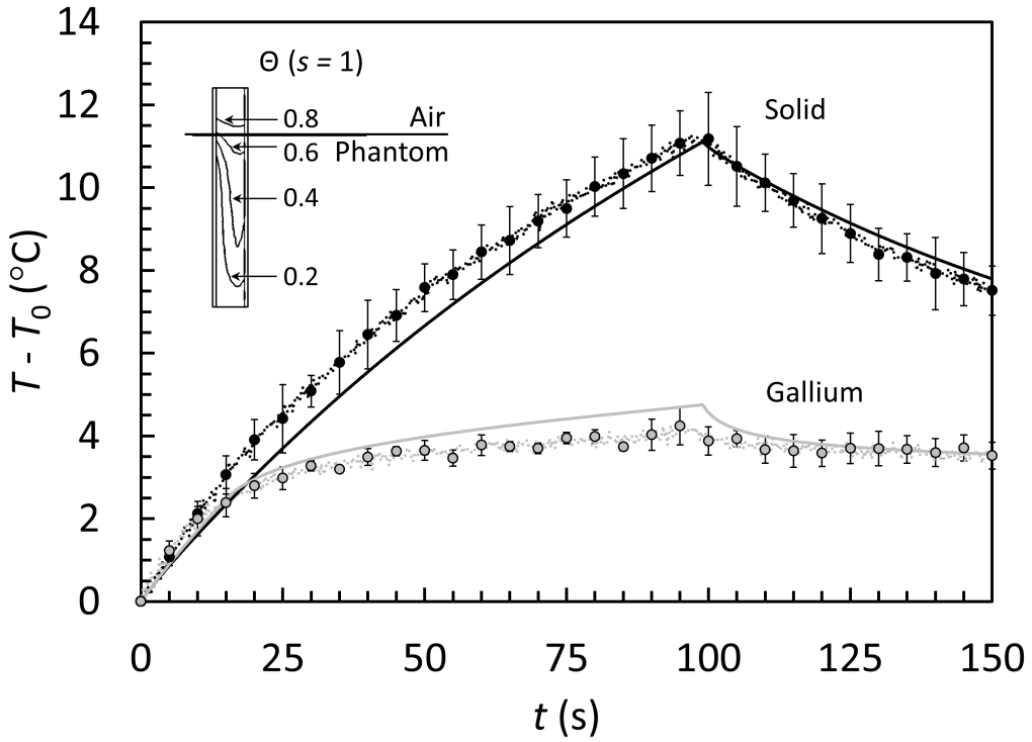

Figure 10.2. Numerical model validation. Comparison of the measured temperatures (dotted lines) with those predicted by the numerical model (solid lines) for solid electrodes (black) and phase change electrodes (gray). The insert shows the volume fraction of solid material predicted by the numerical model at the end of the 99 s pulse protocol.

In the case of the solid electrodes, the numerical model (solid lines) accurately predicts the experimentally measured temperatures within a single standard deviation at a majority of time points by using analytically derived boundary conditions and material properties taken from the literature (Figure 10.2). The only unknown variable for the PCM electrodes was the transition range of gallium. The results of the parametric study performed on this variable indicate that the highest correlation between measured and predicted temperatures occurs when T_R was set to 0.5°C (R^2 = 0.74). Lower values of T_R, or more abrupt transitions, overestimated the measured temperature at the onset of the phase transition, whereas higher values of T_R, or more gradual transitions, underestimated the measured temperature at the onset of the phase transition. The opposite was true during the return to baseline following treatment. As in the case of the solid electrodes, the predicted temperatures produced by the optimized gallium transition range were

in agreement with measured values from the PCM electrodes within a single standard deviation at a majority of time points. A plot of the volume fraction of solid gallium within one of the electrodes (Figure 10.2, insert) indicates that there was preferential heating/melting on the deep-medial portion of the electrodes. It also suggests that the phase transition in these regions is complete, while a majority of the superficial gallium remains solidified ensuring containment within the brass shell.

Solutions from the validated numerical model for the electric field and temperature distributions at the end of treatment are shown in Figure 10.3. There was no electrical conductivity dependence on temperature included in the model, and the electric field distributions for both scenarios are identical (Figure 10.3 a). As a general rule of thumb, any regions of tissue exposed to an electric field threshold of 500 V/cm or greater are subject to electroporation (Garcia et al., 2010). For the solid electrodes (Figure 10.3 b), a maximum temperature of 47.9°C occurred at the center of the tissue domain between the electrodes. This was a 22°C increase above the baseline temperature. By incorporating a PCM core, the maximum temperature reached between the electrodes was only 41.2°C. Therefore, the change in temperature was reduced by approximately 7°C. This reduction would likely become more pronounced during longer protocols, or shorter protocols at higher voltage, until the gallium completely enters the liquid state.

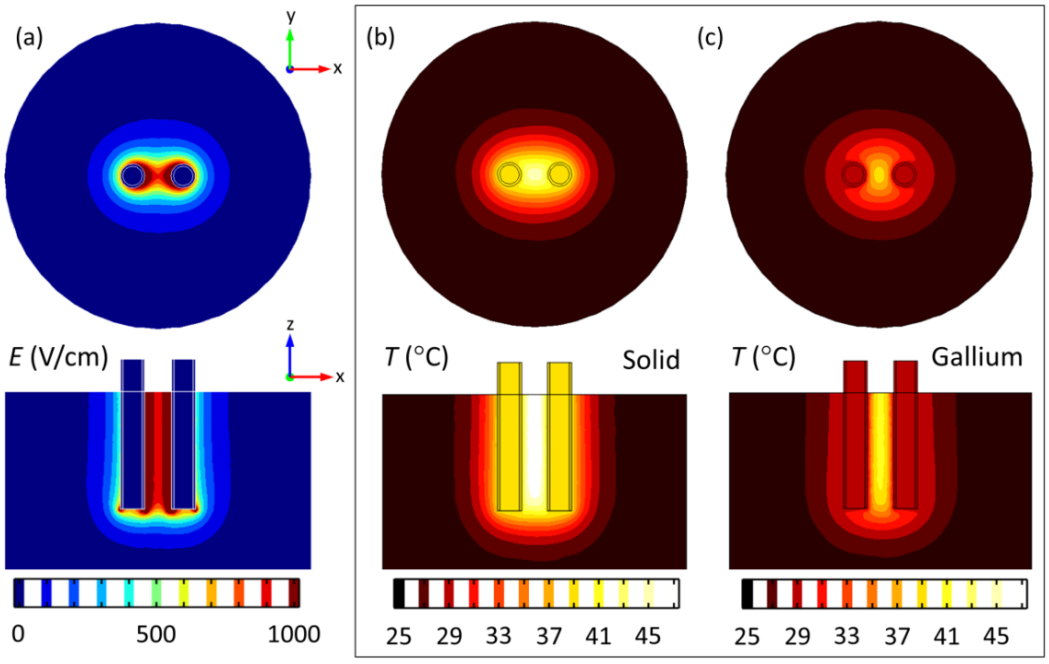

Figure 10.3. Surface contour plots from the numerical model. Electric field distribution (a) and temperature distribution for the solid electrodes (b) and phase change electrodes (c). All plots are shown at the end of the 99 s pulse protocol. In the *x*-*y* plane, the cross-section is taken at a depth of 1.80 cm from the surface of the ultrasound gel. In the *x*-*z* plane, the cross-section is taken through the center of the electrodes (y = 0).

Figure 10.4 shows temperature profiles resulting from the parametric study on electrode radius and metallic PCM melting temperature during the clinical IRE scenario. The temperature data was evaluated at the medial electrode-tissue-interface 1.80 cm below the surface of the ultrasound gel (same depth as experimental recordings). In all cases, including the solid electrodes (dotted lines), as electrode radius increased, the peak temperature at the end of treatment was reduced. This is due to the fact that larger electrodes have a diminished electric potential gradient along their boundaries. However, solid electrodes generally produced higher temperatures than PCM electrodes of equivalent radius. One exception occurred for large PCM electrodes with a T_M that exceeds the core temperature during treatment (Figure 10.4 d where T_M - T_0 = 10°C). In this case, there was no phase transition and the heat capacity per unit volume was greater for the solid electrode.

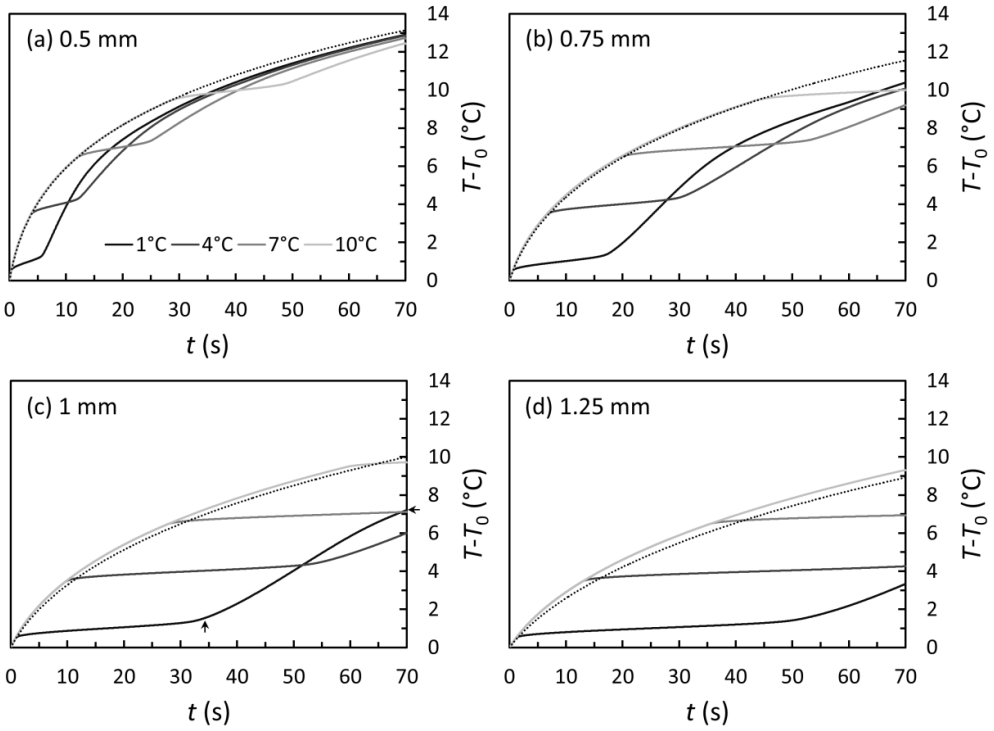

Figure 10.4. Gallium core temperature profiles. Parametric study on electrode radius (0.5, 0.75, 1.0, and 1.25 mm) and PCM melting point above the baseline temperature (1, 4, 7, and 10°C). Temperatures are plotted at the medial electrode-tissue-interface at a depth of 1.80 cm from the surface of the ultrasound gel. Dotted lines represent the solid electrode. In part (c), the vertical arrow indicates the end of melting and the horizontal arrow highlights the temperature at the end of treatment.

The temperature profiles also illustrate the tradeoff between choosing a T_M that is low enough to begin absorbing heat at the start of treatment and a T_M that is high enough to avoid complete melting before the end of treatment. For example, in Figure 10.4 c when T_M was 1°C above the ambient temperature, the center of the core at a depth of 1.80 cm was completely melted by 35 s (indicated by the vertical arrow), and the temperature increased at a faster rate for the remainder of the treatment due to a decreased heat capacity per unit volume. For larger electrodes capable of holding a greater volume of PCM, the transition time is extended, and a T_M of 1°C above the baseline is advantageous (Figure 10.4 d).

Figure 10.5 shows temperature profiles at identical points of interest from the parametric study when repeated for an organic PCM (k_{eq}/100). Similar trends were observed as in the

metallic case, with the main exceptions being the rate of temperature increase during the phase transition. Due to the increased thermal resistance, the temperature increased at a faster rate throughout the phase transition. However, this was balanced by the fact that it takes longer for the organic PCM to melt. For example, in Figure 10.5 c when T_M was 1°C above ambient conditions, it took 68 s for the center of the core to melt at a depth of 1.80 cm (indicated by the vertical arrow). This occurred nearly in unison with the end of treatment at 70 s. As a result, the organic PCM maintained a final peak temperature that was lower than that of the metallic PCM of equivalent radius and melting point. It is important to note that the salt hydrate PCM (k_{eq}/10) resulted in the highest temperatures during treatment for all parameter combinations (data not shown).

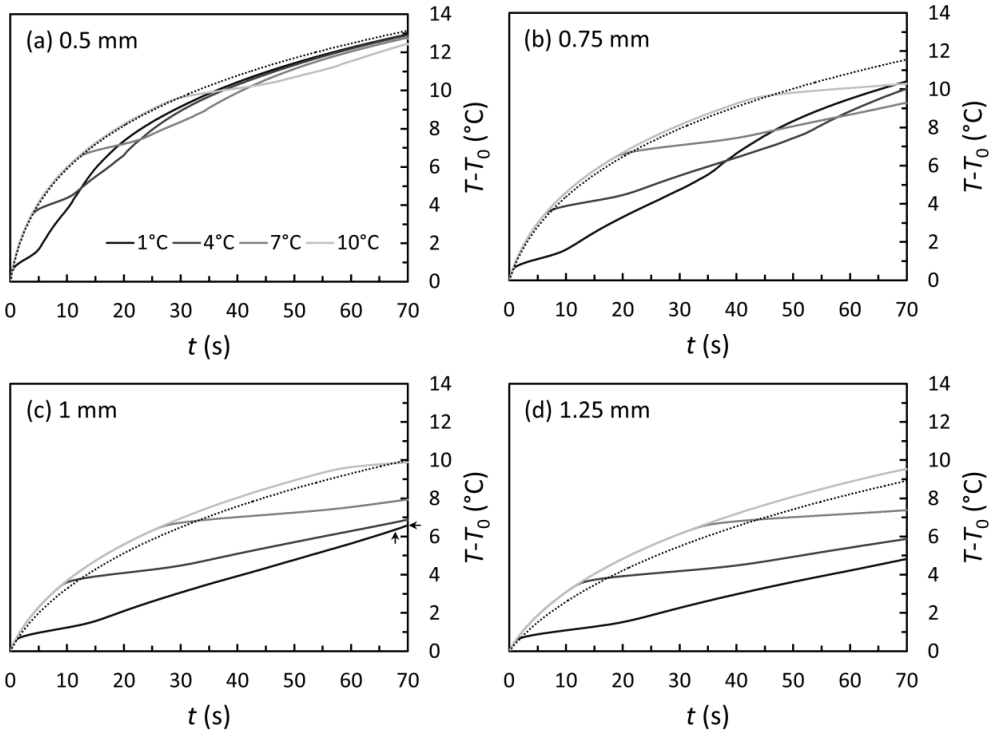

Figure 10.5. Organic PCM temperature profiles. Parametric study on electrode radius (0.5, 0.75, 1.0, and 1.25 mm) and PCM melting point above the baseline temperature (1, 4, 7, and 10°C) when k_{eq}/100. Temperatures are plotted at the medial electrode-tissue-interface at a depth of 1.80 cm from the surface of the ultrasound gel. Dotted lines represent the solid electrode for comparison. In part (c), the vertical arrow indicates the end of melting and the horizontal arrow highlights the temperature at the end of treatment.

Figure 10.6 summarizes the results of Figures 10.4 and 10.5 by compiling the data for temperature increase by the end of treatment. As a whole, the metallic PCM provides the most reduction in temperature at any given radius if the melting point is tuned correctly. However, as mentioned, if melting is completed relatively early-on, it becomes possible for the organic PCM to provide better results given the increased thermal resistance and extended transition zone. This special case is highlighted by the negative bar in Figure 10.6 c.

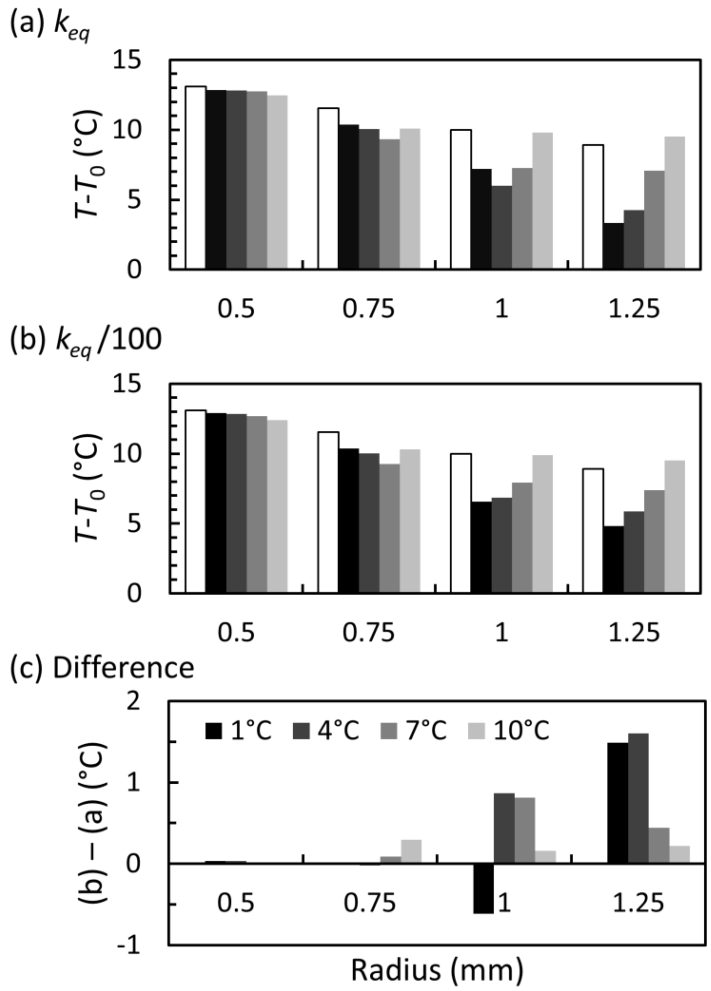

Figure 10.6 Change in temperature during treatment for varying electrode properties. (a) Gallium core electrode and (b) when k_{eq}/100 (b). Part (c) shows the difference between (b) and (a) to emphasize the most effective PCM for each parameter combination. White bars represent the solid electrode for comparison.

Differences in phase transition kinetics are shown in Figure 10.7. The metallic PCM was characterized by smooth transition at the center of the core at a depth of 1.80 cm (Figure 10.7 a). In contrast, the organic PCM remained solid at that position until 66.65 s and then melted abruptly over the next 1.8 s. The salt hydrate PCM presented certain features of both the metallic PCM and organic PCM, giving it the longest overall transition time of 38 s. Due to the high thermal resistance of the organic PCM, it took the longest for heat to conduct inwards from the treated tissue to the electrode core. As a result, a ridge of solid material remained in the core at the end of treatment (Figure 10.7 b). The melting front in the metallic or salt hydrate core surpassed or was approaching the air-tissue-interface, respectively.

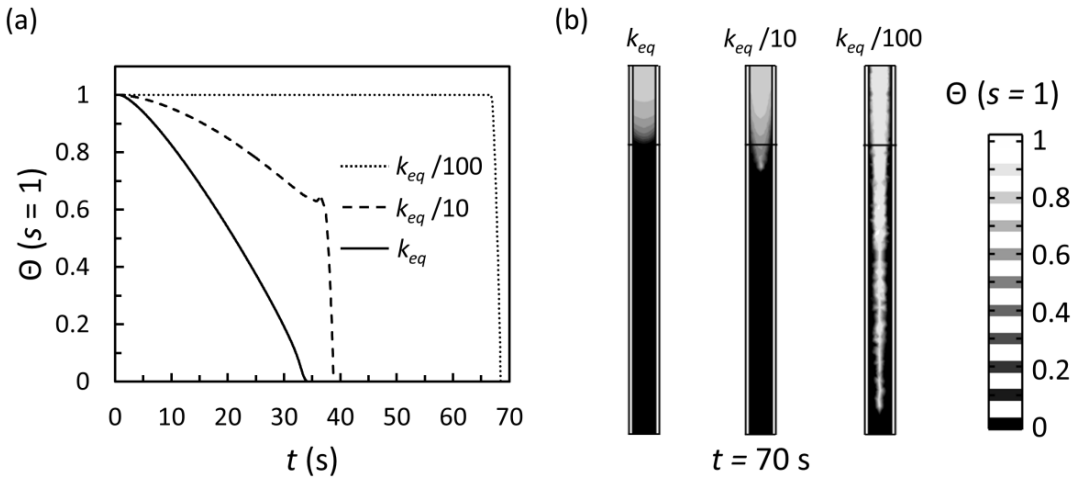

Figure 10.7. PCM melting kinetics. (a) Phase transition profile for different PCM cores (gallium, k_{eq}/10, and k_{eq}/100). The data is taken at the center of the core at a depth of 1.80 cm from the surface of the ultrasound gel. (b) Cross-section of the volume fraction solid material through the center of the electrodes at the end of treatment.

10.4 – Discussion

The results presented above demonstrate that electrodes containing a PCM core can be used to mitigate temperature development during therapeutic electroporation. The choice of gallium as the PCM was made for several reasons. First, its phase is easily manipulated slightly above room temperature, which makes it a logical selection for experimental validation. Second,

the thermal conductivity of metallic PCMs are considerably higher than other classes of PCMs, such as salt hydrates and organics. This enhances heat dissipation to the external environment and keeps temperatures closer to the melting point during the phase transition. Lastly, as alluded to earlier, gallium can be alloyed with bismuth to raise its melting point above physiologic temperature (Predel, 1960). This will be required for the treatment of deep-seated tumors. For tumors treated non-invasively with plate electrodes, pure gallium may be acceptable, since the equilibrium temperature between the target tissue and air is expected to be below 30°C.

Because metallic PCMs have a low thermal resistance and heat uniformly, they melt relatively quickly compared to other classes of PCMs. For shorter ECT and EGT protocols, or when using electrodes with a larger radius, metallic PCMs with a melting point close to ambient conditions are ideal. However, for longer IRE pulse protocols, such as those requiring 90 pulses to achieve contiguous ablations when the electrodes are spaced 2 cm apart (Ben-David et al., 2012), or when using electrodes with a smaller radius, the melting point should be raised to ensure that the phase transition process does not subside before the end of treatment. This relationship between the optimal melting point and electrode radius can be seen in Figure 10.6 a. As the electrode radius increases, the optimal melting point for mitigating peak temperature shifts to lower values. In industrial applications demanding multiple melting-freezing cycles, the re-solidification period also plays into the choice of PCM (Stupar et al., 2010). For electroporation-based therapies, this is less of a concern as electrodes are typically single-use.

According to the parametric study, the greatest reduction in peak temperature, when compared to solid electrodes, was 5.6°C. This occurred at the end of treatment with a 1.25 mm radius electrode containing a metallic PCM that melts 1°C above ambient conditions (Figure 10.6 a). When implemented clinically, this could permit the safe delivery of high-dose IRE or H-

FIRE protocols near thermally sensitive critical structures by eliminating the occurrence of thermal damage surrounding the electrodes. Faroja *et al.* have shown that temperatures of 50°C or greater produce classic findings of thermal coagulation (Faroja et al., 2013). Based on these results, lowering the temperature below 45°C using phase change electrodes would produce ablations that are predominantly associated with non-thermal IRE features, including dehydrated cells and hemorrhagic infiltrate.

Specific calculations for thermal damage based on the simulations presented *herein* were not made due to the fact that experiments were conducted below physiologic levels and the emphasis was placed on elucidating the effects of varying electrode properties. However, relationships between electrode properties and the increase in temperature above a baseline are still expected to translate clinically when trying to avoid reaching certain temperatures. Subsequent studies will include *in vivo* experimental validation of the ability of PCM core electrodes to reduce the probability for thermal damage along with the associated thermal damage calculations. This will also involve incorporating the dynamic features of tissue electroporation, including the electrical conductivity dependence on temperature (R. V. Davalos et al., 2003) and electric field (R.V. Davalos et al., 2004) and evaluating how they affect phase change kinetics. As these functions are known to vary between tissue types (N. Pavselj et al., 2005), it is possible that a different PCM will be required for separate tissues.

10.5 – Conclusion

The incorporation of PCMs into biomedical devices offers a largely unexplored opportunity to enhance therapeutic outcomes. Here, we show their potential to safely expand the parameter space when applying non-thermal electroporation to treat aberrant cell masses. This becomes particularly important in applications of H-FIRE, where greater electric field is required

to induce ablation. In future work, there is room to optimize electrode designs for improved heat transfer into the PCM domain, especially in the case of organics. This could involve added PCM compartmentalization with fins. Outside the field of electroporation, PCMs may also prove useful for thermal ablation modalities, either to prevent tissue vaporization at the site of treatment or reduce the risk of distant grounding pad burns. Further, PCMs present many unique solutions for improving diagnostic imaging and aiding in the storage and preservation of biological materials. Due to this wide variety of applications that can benefit from the inclusion PCMs, it is likely that their use will become commonplace over the next decade.

11 – Overall Conclusions

The research described in this dissertation is at the forefront of therapeutic IRE development. Significant progress has been made in addressing the challenges facing widespread clinical use of the technology presented in Chapter 1. To re-iterate, these challenges are:

1) The presence of multiple tissue types can distort the electric field distribution in the tissue and complicate treatment planning algorithms.
2) The PEFs used to perform IRE cause intense muscle contractions, which requires the administration of general anesthesia and neuroparalytic agents prior to treatment.
3) Cell death is highly dependent upon an electric field threshold, which can vary greatly between cell types.
4) There is an elevated probability for thermal damage in regions surrounding electrodes during high-dose cases of IRE.

To address points 1) and 2), we have developed a technique called H-FIRE that can produce uniform ablations in heterogeneous systems without causing muscle contractions. The underlying basis for these improvements stems from the fact that H-FIRE utilizes bipolar bursts of pulses with durations on the order of nanoseconds. These pulses allow for improved capacitive coupling across cell membranes that make heterogeneous tissues respond as if they were homogeneous. We are hopeful that this will simplify treatment planning algorithms to the extent that dynamic changes in tissue dielectric properties due to electroporation are more subtle during treatment and between tissue types. Additionally, it is possible that insulative microstructures within certain tissues, such as layers of dead cells comprising the surface of skin, will pose less of a barrier to treatment. H-FIRE waveforms also narrow the gap between

thresholds for non-thermal ablation versus electrical stimulation by suppressing the activation of voltage gated channels in excitable cells. By eliminating or drastically reducing muscle contractions, there is the potential to perform treatments without general anesthesia or a neuromuscular blockade. This would reduce procedural costs and open up the application space to diseases currently being treated outside the operating room.

To address point 3), we have constructed a 3D *in vitro* tumor system on which to economically and rapidly perform IRE treatments and determine how the electric field threshold for cell death is influenced by both the cell type and pulse protocol. This model has also proved useful in determining similar relationships for H-FIRE. The platform consists of a collagen hydrogel to which cancer cells readily attach and respond to therapy in a physiologically relevant manner. The data generated from these tests can be used in optimization of treatment planning algorithms for various tissue types. To address point 4), we have designed electrodes that incorporate PCMs at their core. The PCMs are chosen to melt during treatment and absorb heat from the tissue. This becomes particularly important during large IRE ablations with a single electrode insertion or H-FIRE applications, each of which requires an elevated electric field. By mitigating peak temperatures around the electrodes, the potential for thermal damage is reduced, and treatments can continue to be applied safely around critical structures, including major blood vessels and nerves.

Taken together, these promising results warrant future investigations into the use of H-FIRE, *in vitro* tumors, and phase change electrodes. For H-FIRE, experiments are required to validate the theoretical findings that indicate high-frequency, bipolar pulses produce more uniform ablations in heterogeneous tissue. This could be accomplished by treating implanted tumors in mice non-invasively with plate electrodes. Additionally, there is still much to be

learned about the ability of H-FIRE to induce non-thermal ablation without causing muscle contractions. Studies should be conducted in attempt to better understand how the proximity of muscle and nervous tissue affects this ability and influences the selection of pulse parameters. With respect to *in vitro* tumor constructs, further validation is needed showing that the electric field threshold is unchanged when cells are isolated from tissue and seeded in a collagen hydrogel. There is also room to expand this system for testing multiple cell types at one time and elucidating the effects of heterogeneities on the field distribution. Lastly, testing phase change electrodes for high-dose IRE of tissue would likely provide strong evidence of their ability to prevent thermal damage. This could be achieved by monitoring ablations in real-time using ultrasound. These additional experiments, when combined with the work presented here, will enable the use of H-FIRE, treatment planning algorithms guided by experiments on *in vitro* tumors, and phase change electrodes in commercial electroporation systems.

12 – References

Abhat, A. (1983). Low-temperature latent-heat thermal-energy storage - heat-storage materials. *Solar Energy, 30*(4), 313-332.

Abidor, I. G., Arakelyan, V. B., Chernomordik, L. V., Chizmadzhev, Y. A., Pastushenko, V. F., & Tarasevich, M. R. (1979). Electric breakdown of bilayer lipid-membranes. 1. Main experimental facts and their qualitative discussion. *Bioelectroch Bioener, 6*(1), 37-52.

Adrian, R. H., Chandler, W. K., & Hodgkin, A. L. (1968). Voltage clamp experiments in striated muscle fibers. *J Gen Physiol, 51*(5), Suppl:188S+.

Al-Sakere, B., Andre, F., Bernat, C., Connault, E., Opolon, P., Davalos, R. V., . . . Mir, L. M. (2007). Tumor ablation with irreversible electroporation. *PLoS ONE, 2*(11), e1135.

Al-Sakere, Bassim, Bernat, Claire, Andre, Franck, Connault, Elisabeth, Opolon, Paule, Davalos, Rafael V., & Mir, Lluis M. (2007). A study of the immunological response to tumor ablation with irreversible electroporation. *Technol Cancer ResTreat, 6*(4), 301-305.

Amin, D. V., Lozanne, K., Parry, P. V., Engh, J. A., Seelman, K., & Mintz, A. (2011). Image-guided frameless stereotactic needle biopsy in awake patients without the use of rigid head fixation. *J Neurosurg, 114*(5), 1414-1420.

Antonov, V. F., Petrov, V. V., Molnar, A. A., Predvoditelev, D. A., & Ivanov, A. S. (1980). Appearance of single-ion channels in unmodified lipid bilayer membranes at the phase transition temperature. *Nature, 283*(5747), 585-586.

Antunes, C. L., Almeida, T. R. O., Raposeiro, N., Goncalves, B., & Almeida, P. (2012). Using a tubular electrode for radiofrequency ablation numerical and experimental analysis. *Compel-the International Journal for Computation and Mathematics in Electrical and Electronic Engineering, 31*(4), 1077-1086.

Appelbaum, L., Ben-David, E., Sosna, J., Nissenbaum, Y., & Goldberg, S. N. (2012). Us findings after irreversible electroporation ablation: Radiologic-pathologic correlation. *Radiology, 262*(1), 117-125.

Arena, C. B., & Davalos, R. V. (2012). Advances in therapeutic electroporation to mitigate muscle contractions. *J Membra Sci Technol, 2*(1), 1000e1102.

Arena, C. B., Mahajan, R. L., Rylander, M. N., & Davalos, R. V. (2012). Towards the development of latent heat storage electrodes for electroporation-based therapies. *Appl Phys Lett, 101*(8), 083902.

Arena, C. B., Sano, M. B., Rossmeisl, J. H., Jr., Caldwell, J. L., Garcia, P. A., Rylander, M. N., & Davalos, R. V. (2011). High-frequency irreversible electroporation (h-fire) for non-thermal ablation without muscle contraction. *Biomed Eng Online, 10*(102).

Arena, C. B., Sano, M. B., Rylander, M. N., & Davalos, R. V. (2011). Theoretical considerations of tissue electroporation with high-frequency bipolar pulses. *IEEE Trans Biomed Eng, 58*(5), 1474-1482.

Arena, C. B., Szot, C. S., Garcia, P. A., Rylander, M. N., & Davalos, R. V. (2012). A three-dimensional in vitro tumor platform for modeling therapeutic irreversible electroporation. *Biophysical J, 103*(9), 2033-2042.

Bagla, S., & Papadouris, D. (2012). Percutaneous irreversible electroporation of surgically unresectable pancreatic cancer: A case report. *J Vasc Interv Radiol, 23*(1), 142-145.

Ball, C., Thomson, K. R., & Kavnoudias, H. (2010). Irreversible electroporation: A new challenge in "out of operating theater" anesthesia. *Anesthesia and Analgesia, 110*(5), 1305-1309.

Becker, S. M., & Kuznetsov, A. V. (2007). Thermal damage reduction associated with in vivo skin electroporation: A numerical investigation justifying aggressive pre-cooling. *International Journal of Heat and Mass Transfer, 50*(1-2), 105-116.

Beebe, S. J., White, J., Blackmore, P. F., Deng, Y. P., Somers, K., & Schoenbach, K. H. (2003). Diverse effects of nanosecond pulsed electric fields on cells and tissues. *DNA Cell Biol, 22*(12), 785-796.

Belehradek, J., Orlowski, S., Ramirez, L. H., Pron, G., Poddevin, B., & Mir, L. M. (1994). Electropermeabilization of cells in tissues assessed by the qualitative and quantitative electroloading of bleomycin. *Biochim Biophys Acta-Biomembranes, 1190*(1), 155-163.

Ben-David, E., Appelbaum, L., Sosna, J., Nissenbaum, I., & Goldberg, S. N. (2012). Characterization of irreversible electroporation ablation in in vivo porcine liver. *Am J Roentgenol, 198*(1), W62-W68.

Benard, C., Body, Y., & Zanoli, A. (1985). Experimental comparison of latent and sensible heat thermal walls. *Solar Energy, 34*(6), 475-487.

Beop-Min, Kim, Jacques, S. L., Rastegar, S., Thomsen, S., & Motamedi, M. (1996). Nonlinear finite-element analysis of the role of dynamic changes in blood perfusion and optical properties in laser coagulation of tissue. *IEEE J Sel Top Quantum Electron, 2*(4), 922-933.

Bilchik, A. J., Wood, T. F., & Allegra, D. P. (2001). Radiofrequency ablation of unresectable hepatic malignancies: Lessons learned. *Oncologist, 6*(1), 24-33.

Billard, V., Garbay, J. R., Morsli, N., Robert, C., Mir, L., & Marty, M. (2004). Sedation and anesthesia for electrochemotherapy. *Eurocancer: John Libbey Eurotext, Paris*, 229-230.

Boinagrov, D., Loudin, J., & Palanker, D. (2010). Strength-duration relationship for extracellular neural stimulation: Numerical and analytical models (vol 104, pg 2236, 2010). *J Neurophysiol, 104*(6), 3734-3734.

Bower, M., Sherwood, L., Li, Y., & Martin, R. (2011). Irreversible electroporation of the pancreas: Definitive local therapy without systemic effects. *J Surg Oncol, 104*(1), 22-28.

Bozec, L., & Odlyha, M. (2011). Thermal denaturation studies of collagen by microthermal analysis and atomic force microscopy. *Biophysical J, 101*(1), 228-236.

Chang, D. C. (1989). Cell poration and cell-fusion using an oscillating electric-field. *Biophysical J, 56*(4), 641-652.

Chang, I. A., & Nguyen, U. D. (2004). Thermal modeling of lesion growth with radiofrequency ablation devices. *Biomed Eng Online, 3*(1), 27.

Chapman, A.J. (1987). *Fundamentals of heat transfer*: Macmillan.

Charpentier, K. P., Wolf, F., Noble, L., Winn, B., Resnick, M., & Dupuy, D. E. (2010). Irreversible electroporation of the pancreas in swine: A pilot study. *HPB, 12*(5), 348-351.

Chen, M. T., Jiang, C., Vernier, P. T., Wu, Y. H., & Gundersen, M. A. (2009). Two-dimensional nanosecond electric field mapping based on cell electropermeabilization. *PMC Biophys, 2*(1), 9.

Chiu, J., & Fair, P. G. (1979). Determination of thermal conductivity by differential scanning calorimetry. *Thermochimica Acta, 34*(2), 267-273.

Corovic, S., Pavlin, M., & Miklavcic, D. (2007). Analytical and numerical quantification and comparison of the local electric field in the tissue for different electrode configurations. *Biomed Eng Online, 6*(37).

Dantzig, J. A. (1989). Modeling liquid-solid phase changes with melt convection. *Int J Numer Meth Eng, 28*(8), 1769-1785.

Daskalov, I., Mudrov, N., & Peycheva, E. (1999). Exploring new instrumentation parameters for electrochemotherapy - attacking tumors with bursts of biphasic pulses instead of single pulses. *IEEE Eng Med Biol Mag, 18*(1), 62-66.

Daud, A. I., DeConti, R. C., Andrews, S., Urbas, P., Riker, A. I., Sondak, V. K., . . . Heller, R. (2008). Phase i trial of interleukin-12 plasmid electroporation in patients with metastatic melanoma. *J Clin Oncol, 26*(36), 5896-5903.

Davalos, R. V., Mir, L. M., & Rubinsky, B. (2005). Tissue ablation with irreversible electroporation. *Ann Biomed Eng, 33*(2), 223-231.

Davalos, R. V., & Rubinsky, B. (2008). Temperature considerations during irreversible electroporation. *Int J Heat Mass Tran, in press*.

Davalos, R. V., Rubinsky, B., & Lir, L. M. (2003). Theoretical analysis of the thermal effects during in vivo tissue electroporation. *Bioelectrochemistry, 61*(1-2), 99-107.

Davalos, R.V., Otten, D.M., Mir, L.M., & Rubinsky, B. (2004). Electrical impedance tomography for imaging tissue electroporation. *IEEE Trans Biomed Eng, 51*(5), 761-767.

DeBruin, K. A., & Krassowska, W. (1999). Modeling electroporation in a single cell. I. Effects of field strength and rest potential. *Biophysical J, 77*(3), 1213-1224.

Demirbas, M. F. (2006). Thermal energy storage and phase change materials: An overview. *Energ Source Part B, 1*(1), 85-95.

Deri, B, Kotovsky, J, & Spadaccini, C. (2010). Assessment of latent heat reservoirs for thermal management of qcw laser diodes (U. S. D. o. Energy, Trans.) (pp. 1-13). Livermore, CA: Lawrence Livermore National Laboratory.

Duck, Francis A. (1990). *Physical properties of tissues: A comprehensive reference book*. San Diego: Academic Press.

Edd, J. F., Horowitz, L., Davalos, R. V., Mir, L. M., & Rubinsky, B. (2006). In vivo results of a new focal tissue ablation technique: Irreversible electroporation. *IEEE Trans Biomed Eng, 53*(7), 1409-1415.

Edd, J.F., & Davalos, R.V. (2007). Mathematical modeling of irreversible electroporation for treatment planning. *Technol Cancer Res Treat, 6*(4), 275-286.

Eikermann, M., Groeben, H., Husing, J., & Peters, J. (2003). Accelerometry of adductor pollicis muscle predicts recovery of respiratory function from neuromuscular blockade. *Anesthesiology, 98*(6), 1333-1337.

Ellis, T. L., Garcia, P. A., Rossmeisl, J. H., Henao-Guerrero, N., Robertson, J., & Davalos, R. V. (2011). Nonthermal irreversible electroporation for intracranial surgical applications laboratory investigation. *J Neurosurg, 114*(3), 681-688.

Esser, A. T., Smith, K. C., Gowrishankar, T. R., & Weaver, J. C. (2007). Towards solid tumor treatment by irreversible electroporation: Intrinsic redistribution of fields and currents in tissue. *Technol Cancer Res Treat, 6*(4), 261-274.

Esser, A. T., Smith, K. C., Gowrishankar, T. R., & Weaver, J. C. (2009). Towards solid tumor treatment by nanosecond pulsed electric fields. *Technol Cancer Res Treat, 8*(4), 289-306.

Etheridge, Michael L., Choi, Jeunghwan, Ramadhyani, Satish, & Bischof, John C. (2013). Methods for characterizing convective cryoprobe heat transfer in ultrasound gel phantoms. *J Biomech Eng, 135*(2), 021001-021010.

Faroja, Mohammad, Ahmed, Muneeb, Appelbaum, Liat, Ben-David, Eliel, Moussa, Marwan, Sosna, Jacob, . . . Goldberg, S. Nahum. (2013). Irreversible electroporation ablation: Is all the damage nonthermal? *Radiology, 266*(2), 462-470.

Ferraro, B., Morrow, M. P., Hutnick, N. A., Shin, T. H., Lucke, C. E., & Weiner, D. B. (2011). Clinical applications of DNA vaccines: Current progress. *Clin Infect Dis, 53*(3), 296-302.

Fiala, D., Lomas, K. J., & Stohrer, M. (1999). A computer model of human thermoregulation for a wide range of environmental conditions: The passive system. *J Appl Physiol, 87*(5), 1957-1972.

Fischbach, C., Chen, R., Matsumoto, T., Schmelzle, T., Brugge, J. S., Polverini, P. J., & Mooney, D. J. (2007). Engineering tumors with 3d scaffolds. *Nature Methods, 4*(10), 855-860.

Floridi, A., Gentile, F. P., Bruno, T., Delpino, A., Iacobini, C., Paggi, M. G., . . . Benassi, M. (1993). Thermal-behavior of a human glioma cell-line and its response to combinations of hyperthermia and lonidamine. *Oncol Res, 5*(1), 1-10.

Gabriel, C., & Gabriel, S. (1996). Compilation of the dielectric properties of body tissues at rf and microwave frequencies (R. R. D. Occupational and Environmental Health Directorate, Trans.). Texas (USA): Brooks Air Force Base.

Gabriel, S., Lau, R. W., & Gabriel, C. (1996). The dielectric properties of biological tissues .2. Measurements in the frequency range 10 hz to 20 ghz. *Phys Med Biol, 41*(11), 2251-2269.

Garcia, P. A., Pancotto, T., Rossmeisl, J. H., Henao-Guerrero, N., Gustafson, N. R., Daniel, G. B., . . . Davalos, R. V. (2011). Non-thermal irreversible electroporation (n-tire) and

adjuvant fractionated radiotherapeutic multimodal therapy for intracranial malignant glioma in a canine patient. *Technol Cancer Res Treat, 10*(1), 73-83.

Garcia, P. A., Rossmeisl, J. H., Neal, R. E., Ellis, T. L., & Davalos, R. V. (2011). A parametric study delineating irreversible electroporation from thermal damage based on a minimally invasive intracranial procedure. *Biomed Eng Online, 10*(1), 34.

Garcia, P. A., Rossmeisl, J. H., Neal, R. E., Ellis, T. L., Olson, J. D., Henao-Guerrero, N., . . . Davalos, R. V. (2010). Intracranial nonthermal irreversible electroporation: In vivo analysis. *J Membr Biol, 236*(1), 127-136.

Garon, E. B., Sawcer, D., Vernier, P. T., Tang, T., Sun, Y. H., Marcu, L., . . . Koeffler, H. P. (2007). In vitro and in vivo evaluation and a case report of intense nanosecond pulsed electric field as a local therapy for human malignancies. *Int J Cancer, 121*(3), 675-682.

Gascoyne, P. R. C., Pethig, R., Burt, J. P. H., & Becker, F. F. (1993). Membrane changes accompanying the induced differentiation of friend murine erythroleukemia cells studied by dielectrophoresis. *Biochim Biophys Acta, 1149*(1), 119-126.

Gascoyne, P. R. C., & Vykoukal, J. (2002). Particle separation by dielectrophoresis. *Electrophoresis, 23*(13), 1973-1983.

Gaynor, P. T., & Bodger, P. S. (1995). Electrofusion processes: Theoretical evaluation of high electric-field effects on cellular transmembrane potentials. *IEE Proc Sci Meas and Tech, 142*(2), 176-182.

Ge, Haoshan, & Liu, Jing. (2012). Phase change effect of low melting point metal for an automatic cooling of usb flash memory. *Frontiers in Energy, 6*(3), 207-209.

Gehl, J., Agerholm-Larsen, B., Iversen, H. K., Ibsen, P., Moller, J. M., Mahmood, F., & Jensen, K. S. (2011). Preclinical validation of electrochemotherapy as an effective treatment for brain tumors. *Cancer Res, 71*(11), 3753-3762.

Glaser, R. W., Leikin, S. L., Chernomordik, L. V., Pastushenko, V. F., & Sokirko, A. I. (1988). Reversible electrical breakdown of lipid bilayers - formation and evolution of pores. *Biochim Biophys Acta, 940*(2), 275-287.

Golberg, A., & Rubinsky, B. (2012). Towards electroporation based treatment planning considering electric field induced muscle contractions. *Technol Cancer Res Treat, 11*(2), 189-201.

Gowrishankar, T. R., Esser, A. T., Vasilkoski, Z., Smith, K. C., & Weaver, J. C. (2006). Microdosimetry for conventional and supra-electroporation in cells with organelles. *Biochem Biophys Res Commun, 341*(4), 1266-1276.

Gowrishankar, T. R., Stewart, C., & Weaver, J. C. (2004, Sep 1-5). *Electroporation of a multicellular system: Asymptotic model analysis.* Paper presented at the 26th Annual International IEEE Conference of the Engineering Medicine and Biology Society (EMBS).

Gowrishankar, T. R., & Weaver, J. C. (2003). An approach to electrical modeling of single and multiple cells. *P Natl Acad Sci USA, 100*(6), 3203-3208.

Griffith, L. G., & Swartz, M. A. (2006). Capturing complex 3d tissue physiology in vitro. *Nat Rev Mol Cell Biol, 7*(3), 211-224.

Guo, Y., Zhang, Y., Klein, R., Nijm, G. M., Sahakian, A. V., Omary, R. A., . . . Larson, A. C. (2010). Irreversible electroporation therapy in the liver: Longitudinal efficacy studies in a rat model of hepatocellular carcinoma. *Cancer Res, 70*(4), 1555-1563.

Haberl, S., & Pavlin, M. (2010). Use of collagen gel as a three-dimensional in vitro model to study electropermeabilization and gene electrotransfer. *J Membr Biol, 236*(1), 87-95.

Harris, C. M., & Kell, D. B. (1983). The radio-frequency dielectric-properties of yeast cells measured with a rapid, automated, frequency-domain dielectric spectrometer. *Bioelectroch Bioener, 11*(1), 15-28.

Haus, Hermann A., & Melcher, James R. (1989). *Electromagnetic fields and energy*. Englewood Cliffs, N.J. :: Prentice Hall.

Heizmann, C. W., Davey, G. E., & Murmann, P. (2001). Intracellular ca2+ and zn2+ levels regulate the alternative cell density-dependent secretion of s100b in human glioblastoma cells. *J Biol Chem, 276*(33), 30819-30826.

Henshaw, J. W., & Yuan, F. (2008). Field distribution and DNA transport in solid tumors during electric field-mediated gene delivery. *J Pharm Sci, 97*(2), 691-711.

Hibino, M., Shigemori, M., Itoh, H., Nagayama, K., & Kinosita, K., Jr. (1991). Membrane conductance of an electroporated cell analyzed by submicrosecond imaging of transmembrane potential. *Biophysical J, 59*(1), 209-220.

Hirano, S., Saitoh, T. S., Oya, M., & Yamazaki, M. (2000, Jul 24-28). *Long-term supercooled thermal energy storage (thermophysical properties of disodium hydrogenphosphate 12h2o).* Paper presented at the Proceedings of the 35th Intersociety Energy Conversion Engineering Conference (IECEC).

The history of cancer. (2012). *American Cancer Society*.

Hjouj, M., & Rubinsky, B. (2010). Magnetic resonance imaging characteristics of nonthermal irreversible electroporation in vegetable tissue. *J Membr Biol, 236*(1), 137-146.

Hodgkin, A. L., & Huxley, A. F. (1952). A quantitative description of membrane current and its application to conduction and excitation in nerve. *J Physiol, 117*(4), 500-544.

Hu, Q., Viswanadham, S., Joshi, R. P., Schoenbach, K. H., Beebe, S. J., & Blackmore, P. F. (2005). Simulations of transient membrane behavior in cells subjected to a high-intensity ultrashort electric pulse. *Physical Review E, 71*(3), -.

Incropera, F.P., & DeWitt, D.P. (1996). *Fundamentals of heat and mass transfer*: Wiley.

Ivorra, A. (Ed.). (2010). *Tissue electroporation as a bioelectric phenomenon: Basic concepts*: Springer Berlin Heidelberg.

Ivorra, A., Al-Sakere, B., Rubinsky, B., & Mir, L. M. (2009). In vivo electrical conductivity measurements during and after tumor electroporation: Conductivity changes reflect the treatment outcome. *Phys Med Biol, 54*(19), 5949-5963.

Ivorra, A., Mir, L. M., & Rubinsky, B. (2009, Sep 7-12). *Electric field redistribution due to conductivity changes during tissue electroporation: Experiments with a simple vegetal model.* Paper presented at the World Congress on Medical Physics and Biomedical Engineering, Munich, Germany.

Ivorra, A., & Rubinsky, B. (2007). In vivo electrical impedance measurements during and after electroporation of rat liver. *Bioelectrochemistry, 70*(2), 287-295.

Jarm, T., Cemazar, M., Miklavcic, D., & Sersa, G. (2010). Antivascular effects of electrochemotherapy: Implications in treatment of bleeding metastases. [Review]. *Expert Rev Anticancer Ther, 10*(5), 729-746.

Jensen, M. M., Jorgensen, J. T., Binderup, T., & Kjaer, A. (2008). Tumor volume in subcutaneous mouse xenografts measured by microct is more accurate and reproducible than determined by 18f-fdg-micropet or external caliper. *BMC Med Imaging, 8*, 16.

Jex-Blake, A. J. (1913). The goulstonian lectures on death by electric currents and by lightning: Delivered before the royal college of physicians of london. *Br Med J, 1*(2725), 601-603.

Jones, D. M., Smallwood, R. H., Hose, D. R., Brown, B. H., & Walker, D. C. (2003). Modelling of epithelial tissue impedance measured using three different designs of probe. *Physiol Meas, 24*(2), 605-623.

Jordan, D. W., Gilgenbach, R. M., Uhler, M. D., Gates, L. H., & Lau, Y. Y. (2004). Effect of pulsed, high-power radiofrequency radiation on electroporation of mammalian cells. *IEEE Trans Plasma Sci, 32*(4), 1573-1578.

Jose, A., Sobrevals, L., Ivorra, A., & Fillat, C. (2012). Irreversible electroporation shows efficacy against pancreatic carcinoma without systemic toxicity in mouse models. *Cancer Lett, 317*(1), 16-23.

Kanduser, M., Sentjurc, M., & Miklavcic, D. (2006). Cell membrane fluidity related to electroporation and resealing. *Eur Biophys J, 35*(3), 196-204.

Kanthou, C., Kranjc, S., Sersa, G., Tozer, G., Zupanic, A., & Cemazar, M. (2006). The endothelial cytoskeleton as a target of electroporation-based therapies. *Mol Cancer Ther, 5*(12), 3145-3152.

Katsuki, S., Nomura, N., Koga, H., Akiyama, H., Uchida, I., & Abe, S. I. (2007). Biological effects of narrow band pulsed electric fields. *IEEE Trans on Dielectr Electr Insul, 14*(3), 663-668.

Keangin, P., Rattanadecho, P., & Wessapan, T. (2011). An analysis of heat transfer in liver tissue during microwave ablation using single and double slot antenna. *Int Commun Heat Mass, 38*(6), 757-766.

Khudhair, A. M., & Farid, M. M. (2004). A review on energy conservation in building applications with thermal storage by latent heat using phase change materials. *Energ Convers Manage, 45*(2), 263-275.

Kim, J. B. (2005). Three-dimensional tissue culture models in cancer biology. *Semin Cancer Biol, 15*(5), 365-377.

Kolb, J. F., Kono, S., & Schoenbach, K. H. (2006). Nanosecond pulsed electric field generators for the study of subcellular effects. *Bioelectromagnetics, 27*(3), 172-187.

Kotnik, T., & Miklavcic, D. (2000). Theoretical evaluation of the distributed power dissipation in biological cells exposed to electric fields. *Bioelectromagnetics, 21*(5), 385-394.

Kotnik, T., & Miklavcic, D. (2006). Theoretical evaluation of voltage inducement on internal membranes of biological cells exposed to electric fields. *Biophysical J, 90*(2), 480-491.

Kotnik, T., Miklavcic, D., & Mir, L. M. (2001). Cell membrane electropermeabilization by symmetrical bipolar rectangular pulses. Part ii. Reduced electrolytic contamination. *Bioelectrochemistry, 54*(1), 91-95.

Kotnik, T., Mir, L. M., Flisar, K., Puc, M., & Miklavcic, D. (2001). Cell membrane electropermeabilization by symmetrical bipolar rectangular pulses. Part i. Increased efficiency of permeabilization. *Bioelectrochemistry, 54*(1), 83-90.

Kotnik, T., Pucihar, G., Rebersek, M., Miklavcic, D., & Mir, L. M. (2003). Role of pulse shape in cell membrane electropermeabilization. *Biochim Biophys Acta-Biomembranes, 1614*(2), 193-200.

Kotnik, Tadej, & Pucihar, Gorazd. (2010). Induced transmembrane voltage - theory, modeling, and experiments *Advanced electroporation techniques in biology and medicine* (pp. 51-70): CRC Press.

Krishnan, S., & Garimella, S. V. (2004). Analysis of a phase change energy storage system for pulsed power dissipation. *IEEE Trans Compon Pack Tech, 27*(1), 191-199.

Lackovic, I., Magjarevic, R., & Miklavcic, D. (2009). Three-dimensional finite-element analysis of joule heating in electrochemotherapy and in vivo gene electrotransfer. *IEEE Trans on Dielectr Electr Insul, 16*(5), 1338-1347.

Lamsa, T., Jin, H. T., Nordback, P. H., Sand, J., Luukkaala, T., & Nordback, I. (2009). Pancreatic injury response is different depending on the method of resecting the parenchyma. *J Surg Res, 154*(2), 203-211.

Landstrom, F. J., Nilsson, C. O. S., Crafoord, S., Reizenstein, J. A., Adamsson, G. B. M., & Lofgren, L. A. (2010). Electroporation therapy of skin cancer in the head and neck area. *Dermatologic Surgery, 36*(8), 1245-1250.

Lee, Edward W., Loh, Christopher T., & Kee, Stephen T. (2007). Imaging guided percutaneous irreversible electroporation: Ultrasound and immunohistological correlation. *Tech Cancer Res Treat, 6*(4), 287-293.

Lee, R. C., & Astumian, R. D. (1996). The physicochemical basis for thermal and non-thermal 'burn' injuries. *Burns, 22*(7), 509-519.

Lee, R. C., Zhang, D. J., & Hannig, J. (2000). Biophysical injury mechanisms in electrical shock trauma. *Annu Rev Biomed Eng, 2*, 477-+.

Leontiadou, H., Mark, A. E., & Marrink, S. J. (2004). Molecular dynamics simulations of hydrophilic pores in lipid bilayers. *Biophysical J, 86*(4), 2156-2164.

Littlewood, E. R., Gilmore, I. T., Murraylyon, I. M., Stephens, K. R., & Paradinas, F. J. (1982). Comparison of the trucut and surecut liver biopsy needles. *J Clin Pathol, 35*(7), 761-763.

Long, G., Shires, P. K., Plescia, D., Beebe, S. J., Kolb, J. F., & Schoenbach, K. H. (2011). Targeted tissue ablation with nanosecond pulses. *IEEE Trans Biomed Eng, 58*(8).

Lopez, A., Rols, M. P., & Teissie, J. (1988). P-31 nmr analysis of membrane phospholipid organization in viable, reversibly electropermeabilized chinese-hamster ovary cells. *Biochemistry, 27*(4), 1222-1228.

Maor, E., Ivorra, A., Leor, J., & Rubinsky, B. (2007). The effect of irreversible electroporation on blood vessels. *Technol Cancer Res Treat, 6*(4), 307-312.

Maor, E., Ivorra, A., Leor, J., & Rubinsky, B. (2008). Irreversible electroporation attenuates neointimal formation after angioplasty. *IEEE Trans Biomed Eng, 55*(9), 2268-2274.

Maor, E., Ivorra, A., & Rubinsky, B. (2009). Non thermal irreversible electroporation: Novel technology for vascular smooth muscle cells ablation. *PLoS ONE, 4*(3), -.

Marongiu, M. J., & Clarksean, R. (1997, Jul 27-Aug 1). *Thermal management of electronics enclosures under unsteady heating/cooling conditions using phase change materials (pcm).* Paper presented at the Proceedings of the 32nd Intersociety Energy Conversion Engineering Conference (IECEC).

Martin, R. C. G., McFarland, K., Ellis, S., & Velanovich, V. (2012). Irreversible electroporation therapy in the management of locally advanced pancreatic adenocarcinoma. *J Am Coll Surgeons, 215*(3), 361-369.

Marty, M., Sersa, G., Garbay, J. R., Gehl, J., Collins, C. G., Snoj, M., . . . Mir, L. M. (2006). Electrochemotherapy - an easy, highly effective and safe treatment of cutaneous and subcutaneous metastases: Results of esope (european standard operating procedures of electrochemotherapy) study. *EJC Supplements, 4*(11), 3-13.

McLaughlin, S., & Murray, D. (2005). Plasma membrane phosphoinositide organization by protein electrostatics. *Nature, 438*(7068), 605-611.

Merkle, E. M., Shonk, J. R., Zheng, L., Duerk, J. L., & Lewin, J. S. (2001). Mr imaging-guided radiofrequency thermal ablation in the porcine brain at 0.2 t. *Eur Radiol, 11*(5), 884-892.

Mezeme, M. E., Pucihar, G., Pavlin, M., Brosseau, C., & Miklavcic, D. (2012). A numerical analysis of multicellular environment for modeling tissue electroporation. *Appl Phys Lett, 100*(14).

Miklavcic, D., Sel, D., Cukjati, D., Batiuskaite, D., Slivnik, T., & Mir, L. (2004, Sep 1-5). *Sequential finite element model of tissue electropermeabilisation.* Paper presented at the 26th Annual International IEEE Conference of the Engineering Medicine and Biology Society (EMBS).

Miklavcic, D., Semrov, D., Mekid, H., & Mir, L. M. (2000). A validated model of in vivo electric field distribution in tissues for electrochemotherapy and for DNA electrotransfer for gene therapy. *Biochim Biophys Acta-General Subjects, 1523*(1), 73-83.

Miller, L., Leor, J., & Rubinsky, B. (2005). Cancer cells ablation with irreversible electroporation. *Technol Cancer Res Treat, 4*(6), 699-705.

Mir, L. M., Belehradek, M., Domenge, C., Orlowski, S., Poddevin, B., Belehradek, J., Jr., . . . Paoletti, C. (1991). Electrochemotherapy, a new antitumor treatment: First clinical trial. *C R Acad Sci III, 313*(13), 613-618.

Mir, L. M., Devauchelle, P., Quintin-Colonna, F., Delisle, F., Doliger, S., Fradelizi, D., . . . Orlowski, S. (1997). First clinical trial of cat soft-tissue sarcomas treatment by electrochemotherapy. *Brit J Cancer, 76*(12), 1617-1622.

Mir, L. M., Orlowski, S., Belehradek, J., & Paoletti, C. (1991). Electrochemotherapy potentiation of antitumor effect of bleomycin by local electric pulses. *Eur J Cancer, 27*(1), 68-72.

Mondieig, D., Rajabalee, F., Laprie, A., Oonk, H. A. J., Calvet, T., & Cuevas-Diarte, M. A. (2003). Protection of temperature sensitive biomedical products using molecular alloys as phase change material. *Transfus Apher Sci, 28*(2), 143-148.

Morris, D. L., Gananadha, S., & Wulf, S. (2004). Safety and efficacy of radiofrequency ablation of brain: A potentially minimally invasive treatment for brain tumours. *Minim Invas Neurosur, 47*(6), 325-328.

Neal, R. E., 2nd, & Davalos, R. V. (2009). The feasibility of irreversible electroporation for the treatment of breast cancer and other heterogeneous systems. *Ann Biomed Eng, 37*(12), 2615-2625.

Neal, R. E., 2nd, Garcia, P. A., Robertson, J. L., & Davalos, R. V. (2012). Experimental characterization and numerical modeling of tissue electrical conductivity during pulsed electric fields for irreversible electroporation treatment planning. *IEEE Trans Biomed Eng, 59*(4), 1076-1085.

Neal, R. E., 2nd, Rossmeisl, J. H., Jr., Garcia, P. A., Lanz, O. I., Henao-Guerrero, N., & Davalos, R. V. (2011). Successful treatment of a large soft tissue sarcoma with irreversible electroporation. *J Clin Oncol*.

Neal, R. E., 2nd, Singh, R., Hatcher, H. C., Kock, N. D., Torti, S. V., & Davalos, R. V. (2010). Treatment of breast cancer through the application of irreversible electroporation using a novel minimally invasive single needle electrode. *Breast Cancer Res Tr, 123*(1), 295-301.

Neal, R. E., & Davalos, R. V. (2009). The feasibility of irreversible electroporation for the treatment of breast cancer and other heterogeneous systems. *Annals of Biomedical Engineering, 37*(12), 2615-2625.

Neu, J. C., & Krassowska, W. (1999). Asymptotic model of electroporation. *Physical Review E, 59*(3), 3471-3482.

Neu, J. C., & Krassowska, W. (2003). Modeling postshock evolution of large electropores. *Physical Review E, 67*(2), -.

Neumann, E., Schaeferridder, M., Wang, Y., & Hofschneider, P. H. (1982). Gene transfer into mouse lyoma cells by electroporation in high electric fields. *Embo J, 1*(7), 841-845.

Nortemann, K., Hilland, J., & Kaatze, U. (1997). Dielectric properties of aqueous nacl solutions at microwave frequencies. *J Phys Chem A, 101*(37), 6864-6869.

Nuccitelli, R., Pliquett, U., Chen, X. H., Ford, W., Swanson, R. J., Beebe, S. J., . . . Schoenbach, K. H. (2006). Nanosecond pulsed electric fields cause melanomas to self-destruct. *Biochem Bioph Res Co, 343*(2), 351-360.

Okino, M., & Mohri, H. (1987). Effects of a high-voltage electrical impulse and an anticancer drug on invivo growing tumors. *Jpn J Cancer Res, 78*(12), 1319-1321.

Onik, G., Mikus, P., & Rubinsky, B. (2007). Irreversible electroporation: Implications for prostate ablation. *Technol Cancer Res Treat, 6*(4), 295-300.

Orlowski, S., Belehradek, J., Paoletti, C., & Mir, L. M. (1988). Transient electropermeabilization of cells in culture: Increase of the cytotoxicity of anticancer drugs. *Biochem Pharmacol, 37*(24), 4727-4733.

Pakhomov, A. G., Kolb, J. F., White, J. A., Joshi, R. P., Xiao, S., & Schoenbach, K. H. (2007). Long-lasting plasma membrane permeabilization in mammalian cells by nanosecond pulsed electric field (nspef). *Bioelectromagnetics, 28*(8), 655-663.

Pastushenko, V. F., Chizmadzhev, Y. A., & Arakelyan, V. B. (1979). Electric breakdown of bilayer lipid-membranes. 2. Calculation of the membrane lifetime in the steady-state diffusion approximation. *Bioelectroch Bioener, 6*(1), 53-62.

Paszek, M. J., Zahir, N., Johnson, K. R., Lakins, J. N., Rozenberg, G. I., Gefen, A., . . . Weaver, V. M. (2005). Tensional homeostasis and the malignant phenotype. *Cancer Cell, 8*(3), 241-254.

Pavlin, M., Pavselj, N., & Miklavcic, D. (2002). Dependence of induced transmembrane potential on cell density, arrangement, and cell position inside a cell system. *IEEE Trans Biomed Eng, 49*(6), 605-612.

Pavlin, M., Slivnik, T., & Miklavcic, D. (2002). Effective conductivity of cell suspensions. *IEEE Trans Biomed Eng, 49*(1), 77-80.

Pavselj, N., Bregar, Z., Cukjati, D., Batiuskaite, D., Mir, L. M., & Miklavcic, D. (2005). The course of tissue permeabilization studied on a mathematical model of a subcutaneous tumor in small animals. *IEEE Trans Biomed Eng, 52*(8), 1373-1381.

Pavselj, N., Preat, V., & Miklavcic, D. (2007, Jun 26-30). *A numerical model of skin electroporation as a method to enhance gene transfection in skin.* Paper presented at the 11th Mediterranean Conference on Medical and Biological Engineering and Computing.

Pavselj, Natasa, & Miklavcic, Damijan. (2011). Resistive heating and electropermeabilization of skin tissue during in vivo electroporation: A coupled nonlinear finite element model. *Int J Heat Mass Tr, 54*(11-12), 2294-2302.

Pennes, H. H. (1948). Analysis of tissue and arterial blood temperatures in the resting human forearm. *J Appl Physiol, 1*(2), 93-122.

Pilwat, G., Richter, H. P., & Zimmermann, U. (1981). Giant culture cells by electric field-induced fusion. *Febs Lett, 133*(1), 169-174.

Polk, Charles, & Elliot, Postow (Eds.). (1996). *Handbook of biological effects of electromagnetic fields* (Second ed.). New York: CRC Press, Inc.

Portney, L.G., & Watkins, M.P. (2009). *Foundations of clinical research: Applications to practice*: Pearson/Prentice Hall.

Prakash, J., Garg, H. P., & Datta, G. (1985). A solar water heater with a built-in latent-heat storage. *Energ Convers Manage, 25*(1), 51-56.

Prausnitz, M. R., Bose, V. G., Langer, R., & Weaver, J. C. (1993). Electroporation of mammalian skin: A mechanism to enhance transdermal drug delivery. *P Natl Acad Sci USA, 90*(22), 10504-10508.

Predel, Bruno. (1960). Die zustandsbilder gallium-wismut und gallium-quecksilber, vergleich der koexistenzkurven mit den theorien der entmischung. *Zeitschrift für Physikalische Chemie, 24*(3-4), 206-216.

Pucihar, G., Kotnik, T., & Miklavcic, D. (2009). Measuring the induced membrane voltage with di-8-anepps. *J Vis Exp*(33).

Pucihar, G., Miklavcic, D., & Kotnik, T. (2009). A time-dependent numerical model of transmembrane voltage inducement and electroporation of irregularly shaped cells. *IEEE Trans Biomed Eng, 56*(5), 1491-1501.

Puttaswamy, S. V., Sivashankar, S., Chen, R. J., Chin, C. K., Chang, H. Y., & Liu, C. H. (2010). Enhanced cell viability and cell adhesion using low conductivity medium for negative dielectrophoretic cell patterning. *Biotechnol J, 5*(10), 1005-1015.

Reilly, J. P., Freeman, V. T., & Larkin, W. D. (1985). Sensory effects of transient electrical stimulation - evaluation with a neuroelectric model. *IEEE Trans Biomed Eng, 32*(12), 1001-1011.

Rubinsky, Boris, Onik, Gary, & Mikus, Paul. (2007). Irreversible electroporation: A new ablation modality - clinical implications. *Technol Cancer Res Treat, 6*(1), 37-48.

Sano, M. B., Neal, R. E., Garcia, P. A., Gerber, D., Robertson, J., & Davalos, R. V. (2010). Towards the creation of decellularized organ constructs using irreversible electroporation and active mechanical perfusion. *Biomedical Engineering Online, 9*.

Saur, D., Seidler, B., Schneider, G., Algul, H., Beck, R., Senekowitsch-Schmidtke, R., . . . Schmid, R. M. (2005). Cxcr4 expression increases liver and lung metastasis in a mouse model of pancreatic cancer. *Gastroenterology, 129*(4), 1237-1250.

Schoenbach, K. H., Beebe, S. J., & Buescher, E. S. (2001). Intracellular effect of ultrashort electrical pulses. *Bioelectromagnetics, 22*(6), 440-448.

Schwan, H. P. (1957). Electrical properties of tissue and cell suspensions. *Adv Biol Med Phys, 5*, 147-209.

Schwan, H. P., & Foster, K. R. (1980). Rf-field interactions with biological-systems: Electrical properties and biophysical mechanisms. *P IEEE, 68*(1), 104-113.

Seidler, B., Schmidt, A., Mayr, U., Nakhai, H., Schmid, R. M., Schneider, G., & Saur, D. (2008). A cre-loxp-based mouse model for conditional somatic gene expression and knockdown in vivo by using avian retroviral vectors. *P Natl Acad Sci USA, 105*(29), 10137-10142.

Sel, D., Cukjati, D., Batiuskaite, D., Slivnik, T., Mir, L. M., & Miklavcic, D. (2005). Sequential finite element model of tissue electropermeabilization. *IEEE Trans Biomed Eng, 52*(5), 816-827.

Shafiee, H., Garcia, P. A., & Davalos, R. V. (2009). A preliminary study to delineate irreversible electroporation from thermal damage using the arrhenius equation. *J Biomech Eng, 131*(7), -.

Sharma, A., Tyagi, V. V., Chen, C. R., & Buddhi, D. (2009). Review on thermal energy storage with phase change materials and applications. *Renew Sust Energ Rev, 13*(2), 318-345.

Sheeran, P. S., & Dayton, P. A. (2012). Phase-change contrast agents for imaging and therapy. *Curr Pharm Design, 18*(15), 2152-2165.

Sherar, M. D., Moriarty, J. A., Kolios, M. C., Chen, J. C., Peters, R. D., Ang, L. C., . . . Kucharcyk, W. (2000). Comparison of thermal damage calculated using magnetic resonance thermometry, with magnetic resonance imaging post-treatment and histology, after interstitial microwave thermal therapy of rabbit brain. *Phys Med Biol, 45*(12), 3563-3576.

Shim, H., McCullough, E. A., & Jones, B. W. (2001). Using phase change materials in clothing. *Textile Res J, 71*(6), 495-502.

Smith, K. C., Neu, J. C., & Krassowska, W. (2004). Model of creation and evolution of stable electropores for DNA delivery. *Biophysical J, 86*(5), 2813-2826.

Sobotka, S., & Mu, L. C. (2011). Force characteristics of the rat sternomastoid muscle reinnervated with end-to-end nerve repair. *J Biomed Biotechnol*.

Stampfli, R., & Willi, M. (1957). Membrane potential of a ranvier node measured after electrical destruction of its membrane. *Experientia, 13*(7), 297-298.

Steinmetz, T., Wimmer, G., & Clemens, M. (2006). Numerical simulation of transient electro-quasistatic fields using advanced subspace projection techniques. *Adv Radio Sci, 4*, 49-53.

Stupar, A., Drofenik, U., & Kolar, J. W. (2010, Mar 16-18). *Application of phase change materials for low duty cycle high peak load power supplies.* Paper presented at the 6th International Conference on Integrated Power Electronics Systems (CIPS).

Sunderman, F. W. (1949). Rapid measurement of serum total base and estimation of serum sodium; an improved conductivity assembly. *Am J Clin Pathol, 19*(7), 659-664.

Surowiec, A. J., Stuchly, S. S., Barr, J. R., & Swarup, A. (1988). Dielectric properties of breast carcinoma and the surrounding tissues. *IEEE Trans Biomed Eng, 35*(4), 257-263.

Susil, R., Semrov, D., & Miklavcic, D. (1998). Electric field-induced transmembrane potential depends on cell density and organization. *Electro Magnetobiol, 17*(3), 391-399.

Szot, C. S., Buchanan, C. F., Freeman, J. W., & Rylander, M. N. (2011). 3d in vitro bioengineered tumors based on collagen i hydrogels. *Biomaterials, 32*(31), 7905-7912.

Talele, S., & Gaynor, P. (2008). Non-linear time domain model of electropermeabilization: Effect of extracellular conductivity and applied electric field parameters. *J Electrostat, 66*(5-6), 328-334.

Talele, S., & Gaynor, P. (2007). Non-linear time domain model of electropermeabilization: Response of a single cell to an arbitrary applied electric field. *J Electrostat, 65*(12), 775-784.

Talele, S., Gaynor, P., Cree, M. J., & van Ekeran, J. (2010). Modelling single cell electroporation with bipolar pulse parameters and dynamic pore radii. *J Electrostat, 68*(3), 261-274.

Tarek, M. (2005). Membrane electroporation: A molecular dynamics simulation. *Biophysical J, 88*(6), 4045-4053.

Teissie, J. (2002). Membrane destabilizations supporting electropermeabilization. *Cell Mol Biol Lett, 7*(1), 96-100.

Teissie, J., Golzio, M., & Rols, M. P. (2005). Mechanisms of cell membrane electropermeabilization: A minireview of our present (lack of ?) knowledge. *Biochim Biophys Acta-General Subjects, 1724*(3), 270-280.

Tekle, E., Astumian, R. D., & Chock, P. B. (1991). Electroporation by using bipolar oscillating electric field: An improved method for DNA transfection of nih 3t3 cells. *P Natl Acad Sci USA, 88*(10), 4230-4234.

Thomson, K. R., Cheung, W., Ellis, S. J., Park, D., Kavnoudias, H., Loader-Oliver, D., . . . Haydon, A. (2011). Investigation of the safety of irreversible electroporation in humans. *J Vasc Interv Radiol, 22*(5), 611-621.

Tieleman, D. P. (2004). The molecular basis of electroporation. *Biophysical J, 86*(1), 371a-372a.

Tieleman, D. P., Leontiadou, H., Mark, A. E., & Marrink, S. J. (2003). Simulation of pore formation in lipid bilayers by mechanical stress and electric fields. *J Am Chem Soc, 125*(21), 6382-6383.

Titomirov, A. V., Sukharev, S., & Kistanova, E. (1991). In vivo electroporation and stable transformation of skin cells of newborn mice by plasmid DNA. *Biochim Biophys Acta, 1088*(1), 131-134.

Tsong, T. Y. (1983). Voltage modulation of membrane permeability and energy utilization in cells. *Bioscience Reports, 3*(6), 487-505.

van den Honert, C., & Mortimer, J. T. (1979). Response of the myelinated nerve fiber to short duration biphasic stimulating currents. *Ann Biomed Eng, 7*(2), 117-125.

Verbridge, S. S., Choi, N. W., Zheng, Y., Brooks, D. J., Stroock, A. D., & Fischbach, C. (2010). Oxygen-controlled three-dimensional cultures to analyze tumor angiogenesis. *Tissue Eng Part A, 16*(7), 2133-2141.

Vernier, P. T., Levine, Z. A., Wu, Y. H., Joubert, V., Ziegler, M. J., Mir, L. M., & Tieleman, D. P. (2009). Electroporating fields target oxidatively damaged areas in the cell membrane. *PLoS ONE, 4*(11), -.

Vernier, P. T., Sun, Y., & Gundersen, M. A. (2006). Nanoelectropulse-driven membrane perturbation and small molecule permeabilization. *BMC Cell Biology, 7*, 37.

von Burstin, J., Eser, S., Paul, M. C., Seidler, B., Brandl, M., Messer, M., . . . Saur, D. (2009). E-cadherin regulates metastasis of pancreatic cancer in vivo and is suppressed by a snail/hdac1/hdac2 repressor complex. *Gastroenterology, 137*(1), 361-371.

Wagner, G. H., & Gitzen, W. H. (1952). Gallium. *J Chem Educ, 29*(4), 162.

Weaver, J. C. (1994). Molecular basis for cell membrane electroporation. *Ann N Y Acad Sci, 720*, 141-152.

Weaver, J. C., & Chizmadzhev, Y. A. (1996). Theory of electroporation: A review. *Bioelectroch Bioener, 41*(2), 135-160.

West, D. C., & Wolstencroft, J. H. (1983). Strength-duration characteristics of myelinated and non-myelinated bulbospinal axons in the cat spinal cord. *J Physiol, 337*, 37-50.

Wicker, P. (1990). Electrosurgery-part i. The history of diathermy. [Historical Article]. *NATNews, 27*(8), 6-7.

Wright, N. T. (2003). On a relationship between the arrhenius parameters from thermal damage studies. *J Biomech Eng, 125*(2), 300-304.

Yamada, K. M., & Cukierman, E. (2007). Modeling tissue morphogenesis and cancer in 3d. *Cell, 130*(4), 601-610.

Yao, C. G., Mo, D. B., Li, C. X., Sun, C. X., & Mi, Y. (2007). Study of transmembrane potentials of inner and outer membranes induced by pulsed-electric-field model and simulation. *IEEE Trans Plasma Sci, 35*(5), 1541-1549.

Yousif, N., Bayford, R., & Liu, X. (2008). The influence of reactivity of the electrode-brain interface on the crossing electric current in therapeutic deep brain stimulation. *Neuroscience, 156*(3), 597-606.

Yücel, F., Ünal, N., Erçakır, M., & Güven, G. (2003). Determination of age-related volume changes in rat brain by cavalieri method. *Erciyes Medical Journal, 25*(4), 170-185.

Zalba, B., Marin, J. M., Cabeza, L. F., & Mehling, H. (2003). Review on thermal energy storage with phase change: Materials, heat transfer analysis and applications. *Appl Therm Eng, 23*(3), 251-283.